Buyer, Andreas Anjan, M.Sc. B.Sc.

Contributions to Block Failure Analyses using Digital Joint Network Characterization

Doctoral Thesis

Department of Civil Engineering

Graz University of Technology

Reviewers:

Em.Univ.-Prof. Dipl.-Ing. Dr.mont. Wulf Schubert

Institute of Rock Mechanics and Tunnelling

Graz University of Technology

Prof. John Harrison, PhD.

Department of Civil & Mineral Engineering

University of Toronto

Graz, October 2019

Affidavit

I declare that I have authored this thesis independently, that I have not used other than the declared sources/resources, and that I have explicitly indicated all material which has been quoted either literally or by content from the sources used. The text document uploaded to TUGOnline is identical to the present doctoral thesis.

……………………… ……………………………………………

Date Signature

Acknowledgements

Above all, my gratitude belongs to my wife Hannah, my children Georg, Barbara and Quirin. Also, many thanks to my family. Together, they make life a wonderful experience and all grievances endurable. They were, are and will be the ones to rely on, if times are hard.

I especially want to thank Prof. Wulf Schubert for guiding me along the way and giving me precious lessons in self-organisation as well as answers when I needed them.

My gratitude belongs to Prof. John Harrison, too, who gave me valuable hints concerning presentation techniques, writing style and rock mass classification.

Also, my colleagues, especially Alexander Kluckner, Michael Henzinger and Prof. Qian Liu, contributed to the elaboration of this work by fruitful discussions and help, when I was stuck in the matter.

Furthermore, I express my gratitude to Andreas Gaich and Markus Pötsch for providing me with the latest software versions of ShapeMetriX^{3D} and helpful discussions about the methodology and results.

Graz, October 2019 Andreas Buyer

Kurzfassung

Untersuchung der Blockstabilität mit Hilfe der Digitalen Charakterisierung des Trennflächengefüges

Die Kenntnis des Trennflächengefüges ist in der Felsmechanik wichtig, um Gebirgsarten und Gebirgsverhalten festzulegen. Im laufenden Baubetrieb sind diese Informationen Planungsgrundlage und dienen der Dokumentation. Durch die Entwicklung der digitalen Trennflächenkartierung konnten standardmäßig Detailgrad und Arbeitssicherheit erhöht, sowie Zeit eingespart werden. Der Trend geht weiter in Richtung Automatisierung der Datenerfassung.

Diese Arbeit verknüpft bekannte Methoden zur 3D Punktwolkenanalyse mit neuartigen 2D Bildanalysen, um Trennflächen mit deren statistischen Kenngrößen hochpräzise und automatisiert zu erfassen. Daraus wird ein diskretes Trennflächennetzwerk für 3D DEM Simulationen erstellt. Dabei entspricht jede Trennfläche im numerischen Modell einer kartierten Trennfläche und ist mit ihrem Ursprung, sowie ihrer Orientierung und Größe definiert. Um bestehende Ansätze zu verbessern, basiert hier die Trennflächengröße nicht auf einer Wahrscheinlichkeitsverteilung, sondern wird in direkten Bezug zur empirischen Häufigkeitsverteilung aller messbaren Trennflächenspurlängen gesetzt. Das Modell dient der Bestimmung der Gebirgsgeometrie und ist Grundlage für weitere Stabilitätsuntersuchungen. Durch die explizite Modellierung des Trennflächengefüges kann die tatsächliche Ausbruchsgeometrie rekonstruiert und somit wichtige Gebirgseigenschaften rückgerechnet werden. Dazu wurden Sensitivitätsanalysen hinsichtlich des Trennflächenreibungswinkels, sowie des Seitendruckbeiwertes (*K*) durchgeführt. Zur Validierung der Ergebnisse dienen Ausbruchsgeometrie und Ortsbrustdokumentation. Die Methode wurde exemplarisch auf zwei Abschläge in Sprengvortrieben angewandt.

Durch die kombinierte Trennflächenanalyse konnten in Fallstudie I 1405 und in Fallstudie II 2465 Strukturen erfasst werden. Die resultierenden Scharen stimmen gut mit der jeweiligen geologischen Dokumentation überein. Die Blockformen sind in beiden Fällen v.a. plattig, untergeordnet würfelig. In Fallstudie I reichen die Blockgrößen von 0.0002 bis 11.2 m^3 (Mittelwert: 0.124 m^3) und es wurden fünf dominante Blockorientierungen identifiziert. Die Blockorientierung gibt die Orientierung der längsten Verbindungsstrecke zweier Ecken wieder. In Fallstudie II reichen die Blockgrößen von 0.0002 bis 2.5 m^3 (Mittelwert: 0.081 m^3) und die Haupt-Blockorientierung verläuft subparallel zur Schieferung. Die reale Ausbruchsgeometrie konnte in den jeweiligen Simulationen gut nachgebildet werden. In den Fällen, in denen sich Blöcke v.a. aus der Ortsbrust lösen konnten, ist der Reibungswinkel ausschlaggebend für die Blockstabilität. In Fällen, in denen es zum Herauslösen von Blöcken aus der Tunnellaibung kommt, zeigte sich der Einfluss von K auf die Blockstabilität. Im Fall von $K = 1$ kommt es aufgrund der plattigen Blockform und der ungünstigen Lastverteilung zu einem Herauspressen und damit einem höheren Überprofil.

Abstract

Contributions to Block Failure Analyses using Digital Joint Network Characterization

In rock mechanics, a sound knowledge about the joint network geometry is necessary to identify the ground behaviour. This information is part of the design and documentation for the ongoing construction. By the development of digital mapping techniques as a standard application, the level of detail and working safety could be improved and time saved. But the future trend goes towards the automation of data collection.

This thesis combines a well-known technique for 3D point cloud analyses with an innovative 2D image analysis to identify joints and determine their statistical characteristics at a very high precision. Based on this an explicit Discrete Fracture Network is created and each structure in the DFN represents an actual discontinuity from the previous mapping process. Each fracture is defined by its origin, orientation and size. In order to improve existing approaches, the joint size is not based on a probability function but is directly linked to the empirical probability distribution of the apparent joint trace lengths. The numerical model is used for both the determination of the rock mass geometry and a deterministic analysis of the block stability. The highly realistic reconstruction of the joint network around the tunnel allowed a back calculation of the joint friction angle and investigate the influence of the ratio between the principal normal stresses (*K*) by means of a sensitivity analysis. The results are validated with the actual excavation shape and tunnel documentation. The method is applied exemplarily on two D&B tunnel sections.

By combining the two information sources, 1405 (Case Study I) and 2465 (Case Study II) single structures were mapped. The resulting joint sets coincided well with the corresponding geologic documentation. In both cases, platy blocks were dominant, with cubic blocks subordinated to these. The cubic shape was subordinated. In Case Study I, the block volumes range from 0.0002 to 11.2 m^2 at a mean of 0.124 m^3 and five main block orientations were distinguished. The block orientation refers to the trend and plunge value of the longest inter vertex chord length of a block. In Case Study II, the block volumes range from 0.0002 to 2.5 m^3 at a mean of 0.081 m^3 and the block orientation is obviously controlled by the foliation. In the numerical simulations of each case study, the actual excavation shape was approximated very well. In cases, where blocks could slide from the tunnel face, the tunnel stability was most sensitive to the joint friction angle. In cases, where blocks predominantly detached from the tunnel periphery, the influence of *K* on the tunnel stability could be shown. At a $K = 1$, blocks were squeezed out of the rock mass, resulting in a higher volume of moving blocks. This was explained by the unfavourable stress redistribution due to the platy block shape.

Table of Contents

List of Figures

List of Tables

Symbols and Abbreviations

Scalars, Vectors and Matrices

X_t	total spacing
X	joint spacing
X_s	set spacing
X_n	set normal spacing
L	trace length
J_v	volumetric joint count
V_B	block volume
P_{ij}	fracture intensity, with i and j representing the dimensions of the observation space
$\mathbf{e}$	matrix of the binary image with the detected edges
E	eccentricity of an ellipses encompassing a line segment
LS_1	line segments after first selection
l_{PK}	local orientation peak
l_{MIN}	local orientation valley
$\mathbf{f_{corr}}$	correlation filter mask
I	placeholder for the number/index of the orientation peak from the primary peak detection
n_{PK}	number of detected peaks after the second orientation filtering
N	value at peak *i*
$\mathbf{g}$	sum over all orientation dependant correlation images from matrix **e**
d_{ss}	maximum Euclidean distance
n_{corr}	minimum correspondence value
K	number of nearest neighbours in the k-nearest neighbour search
L_a	apparent joint trace length
L_t	theoretical joint trace length
$P(L_t)$	random cumulative probability between 0 and 1
R^2	coefficient of determination

RMSE	root mean square error
K	ratio between the principal normal stresses σ_1 and σ_3
a_{tol}	general tolerance value for the 3DEC model
$V_{B,ref}$	minimum reference block volume
$V_{B,min}$, $V_{B,max}$	minimum and maximum block volume
$V_{B,25/50/75}$	25, 50 and 75% quantile of the block size distribution
$\vec{\mathbf{u}}$	plane normal vector of plane i
$\vec{\mathbf{v}}$	plane normal vector of plane j
a, b, c, d	parameters describing the analytical approximation of the empirical joint size distribution
$P(L)$	probability distribution function for describing the joint size distribution
r_0	original radius of the disc shaped joint
r_1	disc radius according to eq. 2.9 with quantile value of n_{xt} [m]
$\overrightarrow{\boldsymbol{V_1}}$	vector between the two most distant boundary points
$\overrightarrow{\boldsymbol{V_2}}$	normal vector of plane i
$\overrightarrow{\boldsymbol{V_3}}$	perpendicular vector to $\overrightarrow{\mathbf{V_2}}$ and $\overrightarrow{\mathbf{V_3}}$
$\boldsymbol{O_0}$	original joint origin (base)
$\overrightarrow{\boldsymbol{O_{r,v}}}$	vector with a length of $\sqrt{r_1^2 - r_0^2}$ to move from $\mathbf{O_0}$
$\vec{\boldsymbol{a}}, \vec{\boldsymbol{b}}$	vectors of corresponding block vertices
A_s	block surface area [m^2]
$\bar{l}$	mean vertex length [m]
R	maximum Ratio of unbalanced forces
z_{dil}	maximum shear displacement
G	unit weight of a block
F_t	tangential force acting on a joint plane parallel to the tunnel direction as a result of circumferential stresses around the excavation, the force is split into a component acting parallel to the joint plane and into a component perpendicular to the joint plane

Greek letters

α	block flatness Index
β	block elongation Index
ψ	line segment orientation
$\alpha_{l,P}$	lower angular boundary of primary orientation clustering
$\alpha_{u,P}$	upper angular boundary of primary orientation clustering
θ	angle between normal vector $\vec{\mathbf{u}}$ and $\vec{\mathbf{v}}$
β_{sl1}	maximum angular deviation for the first segment linking stage
β_{sl2}	maximum angular deviation for the second segment linking stage
ι	dilation angle
φ	joint friction angle
φ_{res}	residual joint friction angle
σ_1, σ_3	principal normal stresses
ς	standard deviation
γ	intersection angle between two joints (2D) forming a block
ψ	line segment orientation

Abbreviations

P	Persistence
ISBD	In-situ Block Size Distribution
GT	Ground type
GBT	Ground Behaviour Type
JS	Joint Set
DCF	Discontinuity-controlled block failure
GB	Ground Behaviour
D&B	Drill and Blast Excavation
DD/D	Angle of Dip Direction/Dip Angle
TRS	Terrestrial Remote Sensing
TLS	Terrestrial Laser Scanning

TDP	Terrestrial Digital Photogrammetry
RQD	Rock Quality Designation
JRC	Joint Roughness Coefficient
ISRM	International Society for Rock Mechanics and Rock Engineering
UDEC	Universal Distinct Element Code
DDA	Discontinuous Deformation Analysis
3DEC	3D Distinct Element Code
DFN	Discrete Fracture Network
KBT	Key Block Theory
JPD	Joint Plane Detection
JTD	Joint Trace Detection
SMX	ShapeMetriX3D
PDF	Probability Density Function
MTO	Median trace orientation within one orientation cluster
DSE	Discontinuity Set Extractor
CDF	Cumulative Density Function
DoO	Degree of Orientation
CoC	Cone of Confidence
SA	Spherical Aperture
PSS	Primary Stress State
SSS	Secondary Stress State
SOI	Station of Interest, i.e. the station where the joint network geometry in the tunnel face is mapped
NoM	Number of Measurements
FOS	Factor of Safety

1 Introduction

In tunnelling, all construction activities are tightly scheduled and delay is often intolerable. Those schedules are planned according to a preliminary study, including information about the distribution of ground behaviour types. However, during the excavation not everything can be performed as planned as the rock mass often does not appear as expected. Such unexpected changes can lead to higher deformations or lower advance rates due to a weaker material, like fault zones, or a changing joint network geometry. To document these changes and help updating the geological-geotechnical model of the project and therefore increase its accuracy, geologists are mapping the tunnel face as soon as possible. Those maps are usually hand-drawn and include information about the joint network geometry, lithology and other geotechnical features. But the time for the geologists to draw a detailed joint trace map of a tunnel face on-site is limited, since the miners want to proceed with tunnel advance. As a result, a manually drawn discontinuity map is rather qualitative and subjective than quantitative and objective (Slob & Hack, 2004, Gaich et al., 2004b, Gaich et al., 2004c, Gaich et al., 2006, Gaich & Pötsch, 2011). Only dominant and obvious structures are recognized and captured, but they might not be the sole geotechnically relevant structures in the tunnel face. Consequently, conclusions, like the stability of blocks against failure, drawn from this information are lacking in reliability. However, in order to predict and document discontinuity-controlled block failure, accurate knowledge about the joint network is crucial, since a proper prediction can reduce the effort for blasting and remedial action. A comprehensive knowledge about the joint network reduces the risk for the construction staff and equipment, since it allows for more accurate design of support measures.

In this thesis, existing tools for rock mass characterization and joint mapping are combined with novel techniques to overcome these deficiencies. This contributes to an improved level of detail in data acquisition as well as a more realistic implementation of the real joint network geometry in numerical simulations.

In order to find a common ground and avoid misunderstandings, the following section is defining the most important phrases. Afterwards, several reasons for the necessity of quantifying geometrical joint and rock mass properties in rock engineering are given in section 1.2. A summary about the currently applied methods is presented in section 1.3 along with their shortcomings in section 1.4.

1.1 Definitions

Rock Mass

A rock mass is part of the earth’s crust, composed of rock, frequently with anisotropic properties, including discontinuities and voids, filled with loose material, liquids or gases (Austrian Society for Geomechanics, 2010).

Discontinuity, Joint, or Fracture

A discontinuity is a general term for any mechanical discontinuity in a rock mass having zero or low tensile strength. It is a collective term for most types of joints, like bedding planes, foliation, cracks and faults (Austrian Society for Geomechanics, 2010).

A joint is a crack or fracture in a rock mass, caused by the exceedance of the rock mass strength (shear/tension) with little or no movement (Priest, 1993).

It is helpful to distinguish between natural, geologic/ geomorphologic discontinuities and artificial discontinuities, which are caused by blasting, drilling and excavation. (Priest, 1993, Fasching, 2000)

In this thesis, the terms discontinuity, joint and fracture are used interchangeable.

Foliation

Foliation is the summary of numerous closely-spaced discontinuities, separated by thin layers of intact rock. The genesis is due to lithology and stress conditions producing shearing, extension or compression (Priest, 1993).

Discontinuity Network

The discontinuity network is the representation of the complex three-dimensional structure of all discontinuities in a pre-defined rock mass volume (Priest, 1993).

Joint Set

A joint set is a collection of several joints with similar properties, like orientation, spacing, spatial extent, mechanical behaviour and genesis.

Joint Spacing

The joint spacing (X) is defined as the distance of two adjacent discontinuities, measured along a line. Usually, the term spacing refers to the distance between two adjacent discontinuities of one joint set. Three different types are distinguished:

Total spacing (X_t) is the spacing between two immediately adjacent discontinuities along a line of general orientation and location.

Set spacing (X_s) is related to the distance of two immediately adjacent discontinuities along a line of general orientation and location belonging to the same joint set.

Set normal spacing (X_n) is the distance measured normal to the mean orientation of the representative discontinuity set. (Fasching, 2000)

Joint Trace Length

The joint trace length (L) is the length of a line generated by the intersection of a discrete joint with a reference plane, e.g. planar rock face (Priest & Hudson, 1981, Priest, 1993).

A distinction is made between the set trace length (L_S) and the total trace length (L_T), similar to the definition above.

Furthermore, the visible, or apparent joint trace length (L_a) is treated differently than the theoretical joint trace length (L_t) in this thesis.

Persistence and Joint Size

Persistence is an expression for the three-dimensional extent or continuation of a single discontinuity (P) or a set of discontinuities (P_S) in a plane (ISRM, 1978, Slob, 2010). It can for example be described with the size of a discontinuity, resp. its surface area. Measuring this parameter directly is seldom possible. Usually, the size is back calculated by the joint (semi-) trace length (Priest, 1993, Zhang & Einstein, 2000, Fasching, 2000).

Shang et al. (2018) differentiate between the areal extent of a joint plane, referred to as the true persistence and the linear extent definition, e.g. joint trace length, as an approximation of the persistence.

Fracture Intensity

The fracture intensity is the amount of fractures, present in a rock mass. Following the terminology of Dershowitz & Herda (1992), fracture intensity (P_{ij}) can be expressed as a linear fracture intensity (P_{10}), which is the number of fractures along a line, as the volumetric fracture density (P_{32}), which is the sum of the joint surface areas divided by the total unit area, and as the fracture porosity (P_{33}), which is expressed as the sum of the joint surface areas, multiplied by the respective apertures, divided by the total unit area and the total number of fractures.

Spherical Aperture	The Spherical Aperture (SA) is the spread of orientation measurements in one joint set around the mean set orientation. It is comparable with the standard deviation for linear statistics (Wallbrecher, 1986, 3GSM GmbH, 2018).
Concentration	The concentration compares the orientation sample size with the length of the mean orientation vector. The longer the vector for the same sample size, the higher is its concentration. It describes the concentration around a mean orientation value and is equal to the Fisher constant (Wallbrecher, 1986, 3GSM GmbH, 2018).
Degree of Orientation	The Degree of Orientation (DoO) is a normalized measure for the alignment of orientations. 0 % refers to a uniform distribution, whereas 100 % refer to a parallel alignment (Wallbrecher, 1986, 3GSM GmbH, 2018).
Cone of Confidence	The Cone of Confidence (CoC) defines a region (small circle in the stereographic projection) around the calculated mean set orientation, which delimits the deviation of the true mean orientation for a certain level of confidence. If the confidence level is high, the cone of confidence is also very large (Wallbrecher, 1986, 3GSM GmbH, 2018).
Confidence	The Confidence defines a level of certainty/probability for the interpretation of results from statistical analyses. Higher levels include a wider spread of results compared to lower levels (3GSM GmbH, 2018).
Blocky Rock Mass	A blocky rock mass is defined as a rock mass, which has three or more clearly developed and persistent joint sets. Voluminous blocks can be formed in any direction of excavation. The term also includes rock masses, which are cut by extensive joint sets in highly determined orientations as well as rock masses which are randomly cut by non-extensive joint sets with statistically distributed geometrical characteristics (Goodman, 1995).
Ground Behaviour	The ground behaviour (GB) is the reaction of the ground to a full face excavation, without consideration of sequential excavation and support (Austrian Society for Geomechanics, 2010).
Ground Behaviour Type	The ground behaviour type (GBT) is a general category, describing similar GB with respect to failure and displacement characteristics (Austrian Society for Geomechanics, 2010).

Discontinuity Controlled Block Failure	Discontinuity-controlled block failure (DCF) stands for a voluminous, discontinuity-controlled and gravity induced falling or sliding of blocks, combined with an occasional local shear failure on discontinuities (Austrian Society for Geomechanics, 2010).

1.2 Discontinuity-Controlled Block Failure in Tunnelling

In blocky rock masses, joints are forming blocks of any size. Excavation of underground openings creates the necessary kinematical freedom to allow sliding, rotating or falling of blocks into the opening, especially, if the circumferential stresses around the excavation are low (Hoek & Brown, 1994). This can lead to injuries and heavy damage to the construction equipment. Furthermore, the detachment of blocks in the tunnel periphery changes the tunnel shape (Figure 1.1) and causes additional costs due to material transport, necessary backfilling and additional construction time (Mandal & Singh, 2009). Therefore, the existence of potentially instable blocks should be known prior to excavation, sufficient support should be at hand and the blasting pattern in drill and blast (D&B) tunnels should be adaptable to the on-site rock mass geometry.

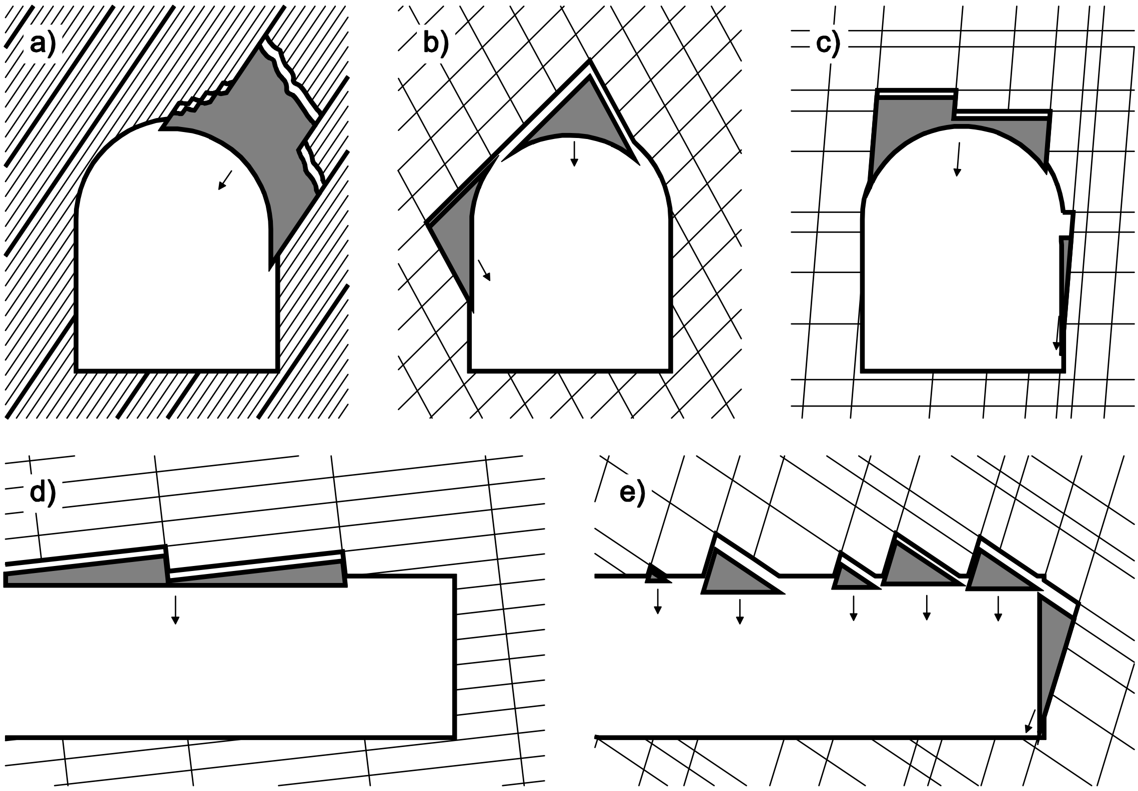

Figure 1.1: Exemplary influence of the joint network geometry on underground excavations and the resulting excavation profile after discontinuity-controlled block failure; a) discontinuity controlled block failure along shear zones in foliated rock masses with tensile failure, b) and c) wedge (block) detachment in the roof and side walls, d) "Sargdeckelbildung" in the roof section with a saw-tooth profile (cross section), e) wedge detachments in the roof and tunnel face (cross section).

1.2.1 Description

A definition of discontinuity-controlled block failure (DCF) is given in section 1.1. The minimum number of non-parallel joint planes to form a block is four. This criterion can be achieved by the intersection of three joint sets and the tunnel periphery as the fourth (free) plane.

Considering block size, there exists a maximum block volume due to the size of the underground opening and the joint network geometry: no larger blocks than the actual underground structure can detach into the opening (Goodman & Shi, 1985, Hoek & Brown, 1994). Blocks below this block size can be kinematically free and may need to be supported, depending on their size, position and the joint properties. On the other hand, there is also a minimum block size, which is not regarded hazardous and blocks below this size do not require support measures. These minor block detachments can also be caused by artificial cracks due to blasting and do not lead to a general change of the tunnel shape. Here, the lower threshold is set to $5 \cdot 10^{-4}$ m^3. This threshold considers a sphere passing a wire mesh with a mesh width of 10 cm, which is commonly used in tunnelling. The effort for preventing smaller blocks from detaching is quite high and is in no relation to the hazard they pose to the equipment and staff.

In addition, the block size influences the shear strength of joint planes. For example, joint planes in densely jointed rock masses generally exhibit a higher shear strength due to the smaller block size. This is related to the joint roughness and the reduced rock mass stiffness due to the scale effect allowing block rotation (Bandis, 1990). Consequently, the resultant overbreak in such ground types is smaller than in blockier rock masses with a lower shear resistance and larger overbreak.

Block detachments can occur at the tunnel face and in the tunnel periphery (crown and side walls). Block failure at the tunnel face is posing a hazard only to the workers and equipment on-site, but does not influence the tunnel shape in general. Detachments in the periphery pose both a hazard to the workers and cause additional costs e.g. due to backfilling, scaling of appropriate support and decreasing advance rates (Costamagna et al., 2018). Block failure can occur immediately after blasting or after a period of time due to stress redistribution and additional vibrations due to blasting (Mandal & Singh, 2009).

1.2.2 Influence on the Excavation

Besides the hazard during excavation, the actual excavation process, e.g. blasting, as well as the tunnel shape after block detachment, is controlled by the block size and shape respectively (Goodman & Shi, 1985, Costamagna et al., 2018). Thuro (2002) summarizes for D&B excavations that the larger the blocks, respectively the wider the joint normal spacing in a rock mass, the more blasting holes (or explosives) have to be drilled to account for smooth blasting. On the contrary, the denser the joint spacing, the better is the excavatability and less effort is necessary for reshaping the tunnel. The failure of blocks in the tunnel periphery leads to a volumetric and areal increase of the excavation (overbreak). This additional volume has to be backfilled in order to:

- satisfy the designed tunnel geometry,
- to ensure contact of the support (e.g. lining) with the rock mass, and
- to prevent other blocks from sliding.

Depending on the volume and additional support for preventing further overbreak, backfilling can be quite costly (Hoek & Brown, 1994, Costamagna et al., 2018). In order to calculate the necessary time and material for reshaping, the expected overbreak has to be predicted as accurate as possible as described in the following.

1.2.3 Quantification of Overbreak

When constructing a tunnel project in Austria, the expected amount of discontinuity-controlled overbreak has to be specified by the Owner (ÖNORM B 2203-1). This information is used in the planning stage to define the ground behaviour type (GBT) and plan sufficient support strategies. Furthermore, the information is necessary to plan the material transport and mucking during excavation. The conclusions have to be regulated in respective contracts. Likewise, underbreak also needs contractual regulations. The (ÖNORM B 2203-1) dictates both, the assessment of potential overbreak during tendering and the determination of actual overbreak during excavation and prior to backfilling.

Overbreak can be estimated manually by an on-site inspection of the damage and physical measurements on the extent of the overbreak, compared with the designed shape. This however is time-consuming, inaccurate and due to the usually low number of possible measurements imprecise. With the application of laser scanning techniques and photogrammetry in tunnelling, scaled 3D point clouds can be used for a direct comparison between designed tunnel shape and the actual tunnel periphery. This comparison can be done in 2D cross sections by computing the volume losses (overbreak) or rock left inside the minimum excavation perimeter (underbreak) (Maerz et al., 1996, Fekete et al., 2010, Gaich et al., 2017, Costamagna et al., 2018).

For quantification, different factors are used (Costamagna et al., 2018), like:

- Overbreak area, which is the area that exceeds the designed tunnel section

- Overbreak distance, which is the distance between the overbreak and the designed profile
- Tunnel Contour Quality Index, which relates the overbreak distances contour ratios and longitudinal variations in each round or for the entire tunnel
- Verbal description and classification

A good estimation of the overbreak is also dependent on a sound knowledge of the controlling factors of DCF in a particular ground type and the reasons why some ground types are less affected by DCF than others.

1.2.4 Controlling Factors

Discontinuity-controlled block failure depends on several parameters and can be classified roughly into six groups (Pötsch, 2002, Goricki, 2003, Mandal & Singh, 2009):

- Rock mass properties (like density, tensile strength, uniaxial compressive strength, shear strength, bulk and shear modulus)
- Joint network geometry (e.g. number of discontinuities and sets/degree of fracturing, orientation of discontinuities, spacing and aperture, size, position of discontinuities)
- Joint properties (e.g. shear strength, planarity, roughness)
- Stress conditions (e.g. primary/secondary stress states, Poisson's ratio of the global rock mass)
- Excavation geometry (e.g. tunnel diameter, tunnel shape, round length)
- Excavation technique (e.g. blasting pattern, drilling accuracy, charge parameters and initiation sequence).

The excavation geometry and rock mass properties are considered constant and known, likewise the stress conditions, if major tectonic influences and changes in overburden can be excluded. Stresses can have stabilizing effects, if the tangential stresses are high – causing e.g. interlocking – or lead to a destabilisation in case of low tangential stresses – increasing the mechanical freedom by reducing the normal stresses on the wedge planes (Pötsch, 2002). The excavation technique and blasting pattern is pre-defined or adapted to the on-site evaluation or the tunnel design. Information about the joint network and joint properties is collected prior to the excavation during exploration programmes and laboratory tests. This information is continuously updated by the ongoing documentation of the joint network in the open tunnel faces (Austrian Society for Geomechanics, 2010).

Usually, in order to predict and analyse block instability (section 1.3) the density of the rock fabric [kg/m³], the mean joint set parameters, the joint properties – if known so far – and the stress conditions are considered. However, the collection of sufficient data about the joint network and rock mass geometry is time consuming and therefore often a mere estimation. Usually, the sample number is too low to allow a statistically valid decision and in addition, only the most dominant and obvious structures a usually documented. The subsequent block stability analyses are aggravated by the fact that only the mean set characteristics of the single joint sets are used with minor statistical deviations. However, local deviations, e.g. in joint orientation or spacing and especially location are usually not distributed uniformly, especially at an insufficient number of measurements, and the usage of a mean value ignores such local deviations. Furthermore, the analyses usually consider infinite and perfectly planar joint planes. This can lead to a misjudgement of the potential block sizes and consequently an inadequate support design.

Summarizing, DCF poses a hazard to equipment and staff and causes additional costs. Therefore, it is necessary to predict or estimate the probability and quantity of DCF in advance.

1.3 Predicting Discontinuity-Controlled Block Failure in Tunnelling

As stated in the previous section a sound knowledge about the rock mass geometry is necessary for analysing the block stability. With this information discontinuity-controlled block failure can be predicted and the expected overbreak quantified properly. Hence, capturing of the joint network (sub-section 1.3.1) and the description of the rock mass geometry (sub-section 1.3.2) should be as detailed and objective as possible. The results can then be used for either analytical or numeric stability analyses (sub-section 1.3.3).

1.3.1 Joint Network

For a detailed description of the joint network, ISRM (1978) and (ÖNORM EN ISO 14689) suggest ten different properties that should be collected by field work:

- Joint **orientation**, **spacing** and **persistence;**
- Joint **roughness** and **wall strength;**

- **Aperture** of the joints and a description of the **filling material;**
- Quantification of **seepage;**
- Assessment of the **number of distinct joint sets** and the resultant **block size.**

To measure or estimate these parameters, several options are available and can roughly be differentiated in conventional and digital measuring techniques. Both approaches offer various advantages and disadvantages and one must choose the best method to apply.

Conventional Mapping

To characterize rock masses, conventional geotechnical data acquisition by geological surveys combines engineering geological judgement and manual methods. Usually, the investigated rock mass is photographed for the documentation and a geological-geotechnical sketch is drawn, which includes information about the joint orientations, block detachments and other features like water seepage. The sketch helps in localizing and abstracting the geological and structural features. But sometimes, the abstraction is too big and the sketch can hardly be referred to the photograph or tunnel face.

Joint orientations are measured with a geological clino-compass (Priest, 1993, Fasching, 2000). Joint set spacings are either estimated or measured with a scanline. This method can be extended by multiple scanlines and mapping windows, which increase the statistical reliability and reduce the inherent bias of a single measurement (Priest & Hudson, 1981, Kulatilake & Wu, 1984, Priest, 1993, Song & Lee, 2001, Mauldon et al., 2001). However, several authors mention shortcomings of the traditional geotechnical data acquisition in the following points (Priest, 1993, Gaich et al., 2004a, Gaich et al., 2006, Haneberg, 2008, Assali et al., 2014, Gaich & Pischinger, 2016):

- OBJECTIVITY: the results are subjective and not reproducible;
- TIME: manual data acquisition is time consuming (up to half a day for one outcrop investigation), and has often a focus only on dominant, apparent structures;
- HAZARD: sometimes the acquisition of data requires access in unsupported regions;
- ACCESSIBILITY: conventional mapping covers relatively small areas, since the measurements are limited by the arm’s reach;

- STATISTICS: the number of manual measurements is low due to the necessary time and possible restrictions in accessibility, and the derived conclusions may not be statistically relevant.

Still, under perfect conditions (free accessibility, no time restrictions and hazard), manual mapping also allows the assessment of parameters, which cannot be measured remotely, like the wall strength, a quantification of the seepage and a characterization of fillings.

Digital Mapping

To overcome the previously mentioned shortcomings in mapping discontinuities on-site, several digital approaches have been developed during the last decades. The main advantage of digital mapping is the reduced time needed on-site for capturing the joint network and the increased time, available to map structures in the office. This leads to a larger set of measurements and a higher objectivity. Consequently, the reliability is increased and block failure analyses can be improved (e.g. Fekete & Diederichs, 2013, Assali et al., 2014, Menegoni et al., 2019).

In general, there exist two different approaches for digital joint mapping:

- a vector-based discontinuity analyses, operating with digital surface models and point clouds (e.g. Sturzenegger & Stead, 2009b), and
- pixel based discontinuity analyses, working with 2D image processing (e.g. Lemy & Hadjigeorgiou, 2003, Azarafza et al., 2019).

Today, digital data acquisition and digital mapping of discontinuities has become state of the art (van Knapen & Slob, 2006, Sturzenegger & Stead, 2009b, Sturzenegger et al., 2011, Liu, 2013, Assali et al., 2014, Tuckey & Stead, 2016, Gaich & Pischinger, 2016, Francioni et al., 2018, Menegoni et al., 2019). Two main approaches have gained acceptance (Poropat, 2006):

- Terrestrial Laser Scanning (TLS) and
- Terrestrial Digital Photogrammetry (TDP).

Both approaches produce comparable 3D point clouds, which can be used for the evaluation of geological information. But, both techniques also have advantages, like geo-referencing and accuracy, and disadvantages, like equipment costs and portability (Haneberg, 2008, Sturzenegger & Stead, 2009a, Francioni et al., 2018). However, TDP has the advantage of the image information being coupled directly with the produced point cloud. Hence, discontinuities, which appear only as linear traces, rather than planar features due to occlusion, are included in the model as well – at least as optical features, which can be mapped manually.

In vector-based applications, a point normal vector is assigned to each point in the point cloud, providing information about its orientation. This information, along with the location and the number of surrounding similarly oriented points, defines distinct planes and hence joint structures for rock mass characterization. Furthermore, Haneberg (2007) developed a procedure to extract directional roughness profiles from point clouds and estimate the Joint Roughness Coefficient (JRC) or asperity angles.

The second source of information is digital image processing (Franklin et al., 1988, Kemeny & Post, 2003, Buyer et al., 2018, Azarafza et al., 2019). A first attempt on an image-based discontinuity mapping, used for rock mass characterization, is proposed by Lemy & Hadjigeorgiou (2003). Lemy & Hadjigeorgiou used a segmentation algorithm combined with the application of certain thresholds, to automatically analyse grey-level images. They detected morphological edges and lines, which represent joint traces and changes in the morphology of the photographed rock face, due to changes in the light exposure and colour. Hence, they were able to collect information about discontinuity trace length, mean and total spacing, frequency and Rock Quality Designation (RQD). Lemy & Hadjigeorgiou (2003) used two different segmentation algorithms, the Canny edge detection algorithm (Canny, 1986) and Steger's algorithm (Steger, 1998), for specific light conditions (oblique and normal illumination) and image specific threshold-values.

The evaluation of geological information in digital outcrop models can be performed either by

- a manual definition of joint planes and traces (Gaich & Pischinger, 2016, Dewez et al., 2016),
- manually defining thresholds to distinguish semi-automatically between a joint plane and edges (Reid & Harrison, 2000, Slob, 2010, Assali et al., 2014, Vasuki et al., 2014, Riquelme et al., 2014, Thiele et al., 2017), or
- a completely automatic analysis (Bolkas et al., 2018, Buyer & Schubert, 2018, Riquelme et al., 2018).

However, for a fully automatized analysis of the rock mass structure with image or 3D point cloud processing, the bias in data accuracy and precision is still too high (Sturzenegger & Stead, 2009a, Gaich & Pötsch, 2011, Sturzenegger et al., 2011, Fekete & Diederichs, 2013). For this reason, different authors (Fasching, 2000, Slob et al., 2007, Haneberg, 2008, Sturzenegger et al., 2011, Fekete & Diederichs, 2013, Assali et al., 2014) discuss the necessity of combining the information from photometric pictures with 3D surface models, in order to improve the analysis and to reduce the influence of confounding factors like vegetation, shadows or cutback traces, which impede a fully automatized image processing (Gaich et al., 2006). But a break-through in the development of a robust and accurate combination of both information sources is still missing, despite some promising approaches (Li et al., 2016, Zhang et al., 2019), where pixel information about the joint network is used to trace structures in the 3D point cloud and compute the spatial orientation of those structures.

Therefore, the main goal of this thesis is to present a methodology in digital rock mass characterization for improving design strategies and increasing the cost efficiency in rock engineering. The proposed methodology shall compensate the lack of robust techniques in semi-automatically mapping the joint network by combining image processing with point cloud analyses. This combination gives more detailed information about:

- the total number of discontinuities in an exposed tunnel face
- the true spacing of a discontinuity set in a tunnel face
- critical intersections of discontinuities in the tunnel face
- quantitative values for the discontinuity size of the investigated rock mass
- the representative block shape and volume, defined by the discontinuity network

With this information at hand, a very detailed and site-specific block stability analysis, based on the generation of a descriptive DFN of the local joint network, and a highly detailed description of the rock mass geometry is possible (Havaej et al., 2016, Huang et al., 2019). Due to the very high number of measurements, a statistical representation of the rock mass is no more necessary and actual specifications, like orientation, spatial position and apparent joint sizes can be measured directly. Moreover, the proposed method also allows the generation of statistical models for a regional discrete fracture network, in order to predict potential overbreak ahead.

Nonetheless, the approach shall not compensate geological-geotechnical expertise, since it cannot differentiate between geotechnical relevant structures and “noise”, but can act as a detailed data basis for further investigations, like numerical simulations and documentation (Buyer et al., 2018). Furthermore, only geometrical features of the rock mass can be captured, but mechanical properties, like seepage, or infilling material cannot be described. This task must still be performed by a skilled expert.

1.3.2 Rock Mass Geometry

Joint Network Geometry

Once joint structures are mapped, the single measurements are classified into joint sets (see definition in section 1). The classification can be done either manually, e.g. by inspecting density plots in the stereographic projection, or automatically, using for example the k-means algorithm (Hammah & Curran, 1998). From here on, parameters like the joint set spacing can be calculated, using scanline mapping, window mapping, or numerical approaches (Gaich et al., 2004a, Riquelme et al., 2015, Vazaios et al., 2018). An actual determination of the true joint spacing on-site is seldom possible (Thuro, 2002) and usually the spacing is described textually (ISRM, 1978, ÖNORM EN ISO 14689). The (ÖNORM EN ISO 14689) also suggests the use of the volumetric joint count (J_V), to describe the degree of fracturing in a reference block volume of 1 m^3.

The persistence or discontinuity size (see definition in section 1.1) controls the intersection of joints and therefore the complete rock mass geometry as well as its mechanical behaviour (Shang et al., 2018). Thus, it is one of the most important parameters in joint network characterization, but it is also one of the most difficult to measure (e.g. Kulatilake et al., 1993, Shang et al., 2018). To describe the discontinuity size, several statistical approaches exist. But to do this adequately, a large number of measurements is necessary (Priest, 1993, Kulatilake et al., 1993, Tuckey & Stead, 2016). Priest (1993) states that the best and most frequently used method, to estimate the discontinuity size, is by calculating it from the joint trace length. Strouth & Eberhardt (2006) estimate the (exposed) joint size by examining the longest distance between two points in a point cloud that belong to the same joint plane. They accept the bias by defining this exposed joint size as a lower boundary of the mean joint persistence. Other approaches (Riquelme et al., 2018) process 3D point clouds and search for co-planar joint planes in one plane and determine the sum of exposed joint plane area relative to the total area, which encompasses all co-planar joint planes. Still, both techniques are dependent on the accuracy of the captured joint network geometry.

Block Geometry

The term ‘geometry’ describes in this case the size, shape and orientation of a block. The block size and shape are roughly defined by the orientation and spacing of the joints or joint sets, forming the block. The orientation is defined as the trend and plunge value of the longest block axis.

The block size is one of the suggested parameters for describing rock masses and is a valuable input parameter in a number of classification systems (Bieniawski, 1973, Barton et al., 1974, Stille & Palmstrøm, 2003, Cai et al., 2004, Kim et al., 2007, Elmo et al., 2014). Especially in blocky rock masses (e.g. plutonic and massive/bedded sedimentary, or metamorphic rocks), the block size is an important factor for rock mass classification (Goricki, 2003). It controls the design and construction of surface and underground works, the quality of blasting, as well as the transportability and excavatability of the material in mining (Stavropoulou, 2014). The combination of block size and rock properties controls the global properties of the rock mass, in which rock masses with larger blocks are generally less deformable than those with smaller blocks (ISRM, 1978, Gottsbacher, 2017). Additionally, Mahtab et al. (1997) state that, according to the joint network geometry, a lower degree of overbreak will be encountered when the joint spacing is low and the number of joint planes is high. The combination of both parameters defines the shape and size of blocks. However, the larger a kinematically and mechanically free block, the higher is the effort to secure this block via anchoring, bolts and/or shotcrete and wire mesh (Figure 1.2).

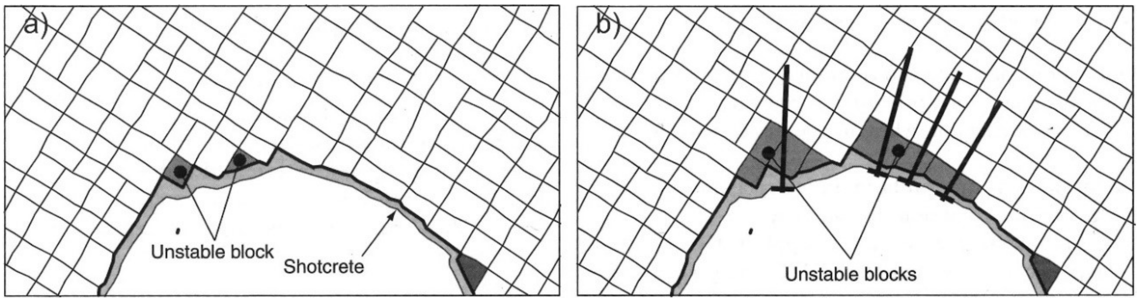

Figure 1.2: Influence of the block size resp. detaching rock mass on the necessary support (Palmström & Stille, 2015).

Since a jointed rock mass consists of numerous blocks, the range of sizes can be represented by the in-situ block size distribution (Elmouttie & Poropat, 2012, Stavropoulou, 2014). Usually, the median, the 25 %- and the 75 %-quantile of the block sizes are provided. Since the determination of the actual in-situ block size distribution (IBSD) is only possible by exposing each single block within the rock mass – a task that is almost impossible and definitely not economical – many authors developed methods to approximate the IBSD. ISRM (1978) and (ÖNORM EN ISO 14689) suggest the determination of the Block Size Index, which represents an average block length or the volumetric joint count (J_v), which represent the block size. Others, like Palmstrøm (2005), Cai et al. (2004) and Kluckner et al. (2015) use empirical formulas to determine the block volume (V_B) by the spacing, the orientation and the joint size for a maximum of three different joint sets. The formulations usually base on the determination of the volume of parallelepipeds, rather than tetrahedrons or higher order polyhedrons. Again, others use Monte-Carlo simulations (Wang et al., 1991, Lu & Latham, 1999) or numerical models (Wang et al., 2003, Kalenchuk et al., 2006, Kim et al., 2007, Elmouttie & Poropat, 2012). A comparison of the single results is given for example in Aichinger (2018) and Söllner (2014). Elmo et al. (2014) and Kim et al. (2015) use geo-statistical Discrete Fracture Network (DFN), to find a correlation between the fracture intensity (P_{ij}) and the fracture length with the resulting block size distribution. Miyoshi et al. (2018) use Discrete Fracture Networks to determine an ISBD and quantify the GSI-system. Here, the fracture intensity and size were also given as crucial parameters in describing the DFN. But in contrast to a purely stochastic DFN, a conditioned DFN, containing major deterministic fractures, e.g. by a comprehensive joint mapping, would improve the application of DFN-models in rock mass classification and stability analyses (Miyoshi et al., 2018).

The importance of the block shape is known in literature (ISRM, 1978, Palmstrøm, 2005, Kalenchuk et al., 2008, ÖNORM EN ISO 14689). Gottsbacher (2017) and Goodman & Shi (1985) state that for analysing the deformability of a jointed rock mass, the block shape in relation to the direction of loading – whether elongated or flat/platy – plays an important role in the global deformability. Hence, an objective classification system is necessary. In most cases, the shape is classified subjectively (ISRM, 1978, Palmstrøm, 2005, ÖNORM EN ISO 14689). These block shapes (Figure 1.3) are hardly describable in mathematical terms, since they include the geological genesis of the investigated rock mass, as well as the natural heterogeneity of joint characteristics.

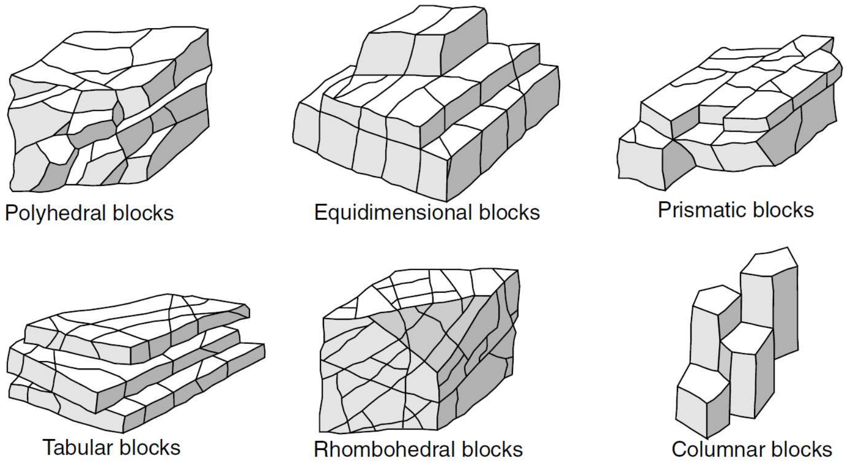

Figure 1.3: Descriptive Block Shape Classes (ISRM, 1978, Palmstrøm, 2005, ÖNORM EN ISO 14689); the classes include information about the joint network geometry as well as their genesis and heterogeneity of the joints.

Nonetheless, they seem to have two basic characteristics in common: elongation and flatness. Kalenchuk et al. (2006) introduced a mathematical solution, to classify the shape of polyhedral blocks. Within this classification, six different block classes, with three major features are distinguished (Figure 1.4). The classification is based on the elongation (β, equation 2.14, sub-section 2.2.2) and flatness (α, equation 2.15, sub-section 2.2.2) of a given block, calculated with the inter vertex chord lengths and their collinearity along with a ratio between the block volume and its surface area. The method is very robust and delivers objective results.

In case of the intersection of three or more joint sets with different joint spacings, the shape of the formed block deviates from a cube and is either platy or elongated (Figure 1.4). According to Gottsbacher (2017), the orientation of blocks in reference to the main direction of loading is controlling the global rock mass deformability. This is especially true for elongated and flat blocks, when the joint normal spacing in direction of loading has the highest deviation. However, the in-situ distribution of the block orientations is almost never investigated.

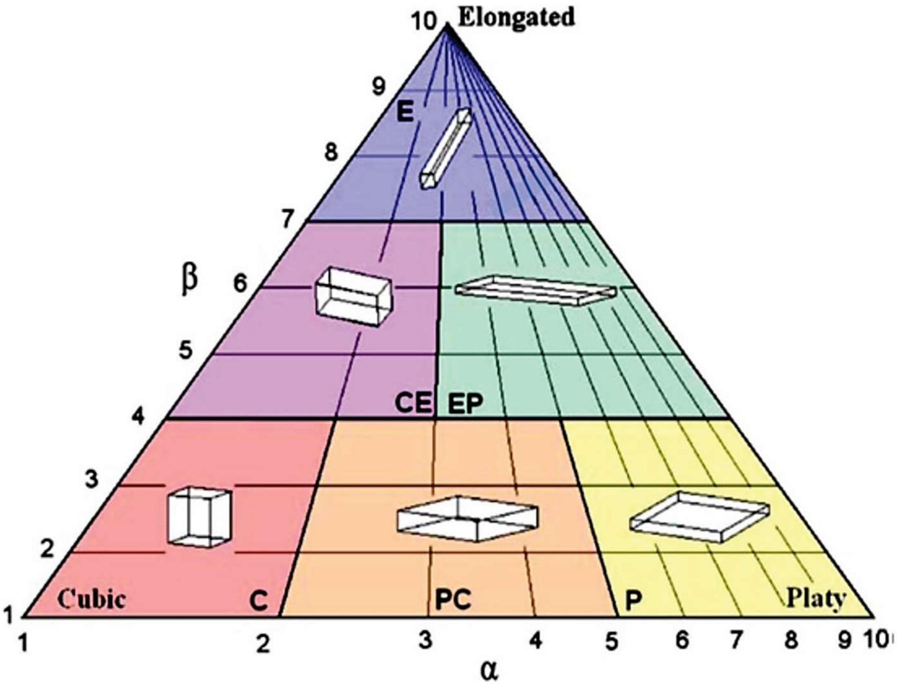

Figure 1.4: Block Shape Classification diagram according to Kalenchuk et al. (2006), the diagram distinguishes three main and three intermediate classes, depending on their elongation (β) and flatness (α).

1.3.3 Quantification of the Block Failure Risk

The amount of discontinuity-controlled overbreak has to be estimated by the Owner (ÖNORM B 2203-1). For block failure, a block needs both kinematical and mechanical freedom. If a block is kinematically free, the mechanical properties acting on the sliding plane(s) might still stabilize the block. The kinematical freedom can be assessed via stereographic projections, tolerating several deficiencies. Subsequently, analytical solutions must be applied to assess the mechanical freedom of a kinematically free block. These analyses are restricted to rather simple cases, usually considering only three different joint sets and no interlocking. For the assessment of complex interactions of the rock mass with the underground excavation, numerical solutions are applied, allowing the investigation of polyhedral blocks with the actual joint network geometry.

Stereographic and Analytical Solutions

To quantify the risk and volume of removable blocks, usually stereographic or vector-based operations are applied (Priest, 1980, Goodman & Shi, 1985, Hoek & Brown, 1994, Hudson & Harrison, 2009). These approaches assume generally infinite and perfectly planar joint planes and use the joint set specifications. For example, Priest (1980) and Hudson & Harrison (2009) propose an inclination of the projection plane in the hemispherical projection resp. the use of the upper and lower hemisphere, in order to analyse block failure modes also in the side walls and roof section. One of the most common techniques is the Key Block Theory (KBT). The KBT identifies key blocks, which are finite, kinematically removable and potentially unstable (depending on the mechanical properties and loading), based on the intersection of joint planes with open spaces (e.g. the tunnel periphery or slopes). The methodology can be performed either vector-based or with a stereographic projection of the joint network and the free surfaces. This makes the KBT a very fast, practical and reliable tool to predict block failure in both surface and underground excavations. The KBT also allows the determination of the volume of convex polyhedral blocks (Pötsch, 2011).

With a known block volume and type of failure (e.g. sliding on one plane, two planes or even more complex modes), it is possible to, calculate the mechanical block stability, considering the joint friction angles and circumferential stress conditions using analytical solutions or, again, stereographic analyses (e.g. Goodman & Shi, 1985, Sofianos et al., 1999, Brady & Brown, 2006).

Nonetheless, since analytical solutions use only the joint set specifications, local variations in the set spacing or orientation are smeared, although they may still form (potential) key blocks (Auzinger, 2015). Additionally, stereographic solutions are usually restricted to three different joint sets, the only possible block shape is a tetrahedron. This however eases the determination of the volume of the instable rock blocks. But a realistic representation of the block stability, including all the variations of a natural joint network, is hardly possible. Consequently, the solutions for a mechanical freedom are inaccurate as well.

Numeric Calculation of Block Instability

To overcome the deficiencies of analytical solutions, numeric approaches were developed and the use of 2D distinct element codes for block stability analysis in tunnelling is quite common (Fasching, 2000, Goricki, 2003, He et al., 2018). Distinct element codes allow explicitly (e.g. UDEC, Itasca Consulting, Inc.) or implicitly (DDA, e.g. Jing (2003)) the analysis of in-situ stress conditions and their influence on the block stability with respect to the intersection of joint planes, joint properties and tunnel shape. A review is given in Jing (2003). However, 2D approaches do only consider the apparent dip of 3D planes and hence other factors, controlling the 3D block stability, are missing. Furthermore, no information is provided about the block sizes.

A common 3D implementation of stereographic operations for analysing structural controlled block failure in underground works is the program UnWedge (Rocscience Inc.). The program allows the analysis of three intersecting joint planes with the underground opening, forming tetrahedral blocks. Again, the joint set specifications are used in the analyses. In case of more than three joint sets, probabilistic simulations can be performed to determine the most unfavourable combination of joint sets. In the simulations it is possible to include mechanical properties along with field stresses and support measures, to stabilize the blocks (Hoek & Brown, 1994, Hoek et al., 1997). However, the approach does not incorporate deviations in the spatial position of joints or the formation of non-pyramidal blocks. The method proposed by Menéndez-Díaz et al. (2009) is similar to UnWedge, but considers also non-pyramidal blocks. It is mainly based on a numerical implementation of the KBT.

In 2013, Fekete & Diederichs (2013) used for the first time the information about the joint network geometry drawn from laser scans for enhanced block stability analyses in a tunnel project. They manually extracted data for the joint orientations, joint set spacings and position of joints from the point cloud. This information is then used to build a 3D distinct element model. For modelling, the authors distinguished between a deterministic and a statistical rock mass reconstruction. With the deterministic reconstruction, the joint network geometry is implemented as mapped in the point cloud – it represents the joint network geometry as seen – whereas the statistical reconstruction uses the statistical interpretation of the joint set specifications, to generate a site specific, but random joint network geometry (Jing, 2003). A deterministic reconstruction can for example be used to directly compare the actual tunnel shape with a numerical model and allows the back calculation of joint properties or the prediction of block failure modes in consecutive rounds. The statistical representation should be used to characterize the joint network geometry and rock mass geometry, rather than for a stability analysis of a particular tunnel section. However, a crucial input parameter for the rock mass behaviour is the actual persistence. Nonetheless, by deterministically modelling a rock mass, Fekete & Diederichs (2013) were able to generate a realistic 3DEC model, which could be compared to the actual tunnel shape. A quasi-deterministic approach for using remote sensing results in numerical stability analyses was performed by Huang et al. (2019). The authors used the information from the digital joint mapping, joint orientation and location, directly in a 3D DEM simulation to perform a stability analysis in the close vicinity of the excavation. However, the measurements were obtained manually and again, the persistence was the crucial parameter in the stability assessments, which was approximated by a parameter study and back calculation. Similarly, Havaej et al. (2016) used remote sensing techniques, to assess the stability of an open pit mine in Cornwall (UK), by generating a DFN in a 3DEC model. Still their mapping of discontinuities in the point cloud of the quarry was based on manual measurements and the DFN was based on statistical parameters, rather than actual measurements. But the application of a combined 3DEC-DFN model showed a better comparability with the actual block failures in the out

Another way to model naturally fractured rock masses is the implementation of a discrete fracture network. The theory of DFN modelling was introduced to rock mechanics by Dershowitz & Einstein (1988), Priest (1993) and Zhang et al. (2002). It is a stochastic approach to model the joint location, orientation, aperture and joint size within a rock mass. Joints are considered for example as circular shaped discs with a limited size, defined by the radius, at statistically distributed locations and varying orientations. Since this is a realistic approximation of a jointed rock mass and avoids the problem of defining a persistence, it was soon implemented in numerical modelling (Dershowitz et al., 2004). It is primarily used for determination of hydraulic properties of jointed rock masses (Jing, 2003). However, it is also applied for stability analyses of cliff walls (Bonilla-Sierra et al., 2015) and pillars in mining (Elmo & Stead, 2010), or for the characterization of intact rock bridges (Scholtès & Donzé, 2012, Elmo et al., 2018) and synthetic rock samples (Mas Ivars et al., 2011). Grenon et al. (2017) and Miyoshi et al. (2018) used a DFN, based on field mapping results or a photogrammetric evaluation of the joint network, to assess the wedge stability in an underground mine. Since DFN heavily relies on mapping results of geological structures (Grenon et al., 2017, Miyoshi et al., 2018), the input has to be as good as possible, despite limited mapping areas or borehole data. Otherwise it has to be represented by stochastic approaches introducing bias from scanline and window mappings (Jing, 2003). Elmo et al. (2015) suggest explicitly to primarily use data collected by objective and indirect sampling methods (like photogrammetry or laser scanning), for the stochastic representation of DFN.

Besides the geometry, the rock mass and joint properties, especially the shear strength, determine whether a block is stable or will move (e.g. Goodman & Shi, 1985, Goricki & Goodman, 2003, Pötsch, 2011, Lambert & Coll, 2014, Gaich et al., 2014). This is controlled by the stress conditions and the constitutive models for the rock material and the joints. However, most of the parameters are either only estimated or described texturally, or not collected at all, since it would require an extensive laboratory program. Nonetheless, using particular and deterministic rock mass models and comparing the numerical results with the actual tunnel behaviour, a back analysis of the shear parameters is possible (Fekete & Diederichs, 2013).

Concluding, a good prediction of DCF is based on a good mapping of the local joint network, since the joint network is controlling the regional rock mass geometry. Both information is necessary for a proper stability analysis regarding the probability and amount of DCF. Those stability analyses can be done either analytically or by using numerical simulations. However, neither method considers the actual orientation and position of discontinuities as they occur in the field and hence the results are based on statistical analyses rather than a site-specific fracture pattern. Hence the actual tunnel shape cannot be reconstructed and a short-term prediction of the conditions in the next excavation rounds is not possible.

1.4 Academic Void and Research Questions

Summarizing the previous statements, discontinuity-controlled block failure poses a hazard to both tunnelling staff and equipment. In addition, it causes costs due to overbreak. In order to describe, predict and document discontinuity-controlled block failure in tunnelling, a sound knowledge about the joint network is necessary. With the current methods there is an apparent lack of information in capturing the discontinuity network appropriately and many assumptions are necessary. This leads to non-reproducible rock mass classifications and uncertainties in rock engineering. In addition, numerical modelling for predicting and documenting discontinuity-controlled block failure is usually based on statistical rather than deterministic joint network properties and may not be able to describe the on-site situation properly, since the statistical representation of the joint network is based on too few measurements, which can also be outliers. This lack of information and reliability can lead to poor designs and increased construction costs as well as an increased risk during excavation. To overcome these deficiencies, it is necessary to improve the data acquisition as well as to find a better implementation of the joint network geometry into numerical simulations. But how can this situation be improved and how can one increase both the quality and quantity of the collected data? Furthermore, how can statistical representations be avoided and the geological documentation be used directly for a site-specific tunnel reconstruction?

These questions are answered in this thesis. This thesis contributes to an improved and objective capturing of the on-site joint network geometry and investigate the applicability of a discrete fracture network for block stability analyses in the selected case studies. The joint network is captured by a novel approach for detecting joint traces in digital images (JTD) coupled with a well-known, vector-based point cloud analysis for detecting joint planes clouds (JPD). The conjoined information is then used to generate highly detailed and deterministic discrete fracture networks, in order to describe discontinuity-controlled block failure numerically and characterize the rock mass geometry. In addition, statistical properties of the joint network and rock mass geometry are determined. For the elaboration, the following questions are addressed:

1. Can the degree of detail of rock mass characterization be improved by using automated and computer aided characterization tools like JPD and JTD?
2. Can a value for the joint size be derived from the spatial information of the mapped joint sets?
3. Does the application of a DFN in block stability analyses result in a good reconstruction of the real excavation shape?
4. Which mechanical factors influence over-excavation in the investigated rock masses?
5. What limitations and uncertainties remain, where the operator must have the possibility to interfere with the results?

The answers to the questions are given in section 5.1. The answers are given as a conclusion of the results, obtained by the proposed method. This work presents a new way to improve geotechnical design and help in mapping the joint network more accurately. This enables a detailed reconstruction of the rock mass in a numerical model and allows the determination of the rock mass geometry as well as block stability. The way to derive this state is explained in the following chapter and is applied on application examples in chapter 3. Here, the power and benefit of the novel approaches is demonstrated and highlights the possibilities of digital rock mass characterization for block stability analyses.

2 Methodology

The essence of the previous chapter is the necessity of determining a joint structure map, which is as detailed and as independent from statistics as possible. This goal shall be reached by a very large number of objective and automatically obtained measurements. The resulting structure map should be implementable directly in numerical block stability analyses, in order to evaluate overbreak and back calculate rock mass as well as joint properties. In the following sections, the rock mass geometry is characterized and a block failure analysis is performed at two case studies of D&B tunnels. The analyses are split into three parts:

1. Gathering information about the joint network using digital image processing (sub-section 2.1.1) and 3D point cloud processing (sub-section 2.1.2),

2. Determination of the statistical joint set specifications using SMX Analyst (sub-section 2.2.1) and characterization of the block geometry in the investigated rock mass (sub-section 2.2.2),

3. Generation of a 3D DFN to simulate a blocky rock mass with 3DEC (section 2.3).

For the analyses, an Intel i7 (4th generation) Quad-Core with 32 GB RAM and a NVIDIA GeForce GTX 960 (4 GB) was used.

The proposed method of this thesis is only applied to tunnelling. Nonetheless, it can also be applied to surface works, like slope stability analyses, and mining.

2.1 Joint Network

As written in sub-section 1.3.1, digital mapping of the joint network can base either on pixel or vector information, leading to the detection of joint traces and planes. In this thesis, both approaches are combined for the first time, to make use of the advantages from both information sources and to obtain a highly detailed structure map of the investigated outcrops.

2.1.1 Joint Trace Detection

The proposed method for detecting joint traces in digital images is based on the approached according to Reid & Harrison (2000) and Lemy & Hadjigeorgiou (2003), in terms of line and edge detection as well as segment linking, but presents also a new way for filtering false positives, linking remote segments and obtaining the most dominant structures in the digital image. Furthermore, the obtained results are transferred into 3D space to calculate the spatial orientation of the detected features.

The analyses are split into four phases: the first phase covers the extraction of the tunnel face and exclusion of the tunnel lining, in order to reduce noise and computation time. The second phase represents the pre-processing steps, to obtain sharper edges and hence more robust results. The third phase comprises the detection of edges and an innovative way of filtering of the results to omit false positives. The applied method is mainly based on the detection of edges in the region of interest with the Canny edge detector and a low-level post-processing of the signals, consisting of correlation and orientation filtering. In the fourth phase loose segments are linked in the first step according to different linking criteria. In a second and new step, the grey-weighted distance transform of the intensity image is used to find the best linkage between remote joint traces within one cluster. Finally, the detected joint traces are transposed into 3D space with the program SMX Analyst, where the spatial orientations are calculated and further processes are performed. SMX Analyst is a commercial program, provided by the company 3GSM GmbH.

For the analyses Matlab version R2018a (The Math Works Inc., 2016) was used. The used Matlab-functions are given specifically in brackets and are in `Courier` style. The functionality of the respective functions are given in the documentation (The Math Works Inc., 2016).

A monochrome image can be represented as a matrix of a size $m \times n$. If the image is polychrome, another dimension is added: $m \times n \times z$, with z representing the dimension, m the number of rows in the matrix and n the number of columns. Hence a coloured image with a red, a green and a blue colour channel with a size of 1028×512 pixel can be represented as a matrix of $1028 \times 512 \times 3$. The position of a pixel within the matrix, given as x and y-coordinates can then be used to compute the real coordinates in a metric system in ShapeMetriX3D.

Exclusion of the Tunnel Lining

In order to reduce computation time and false signals, the tunnel lining is excluded from the analyses. This exclusion is done manually by defining a region of interest (ROI) in the digital image of the tunnel face (using the Matlab-function `roipoly`). The distinction between lining and tunnel face, respectively the rock mass is based on the general excavation shape and differentiation between sprayed concrete and exposed rock. In order to avoid boundary effects, the ROI is shrunken by 15 Pixel (`bwmorph`). The value of 15 Pixel is seen as sufficiently low enough to ensure that the segment linking algorithms and orientation cluster do not select values from the boundary region. A higher value would lead to a loss in valuable information about the joint network in the image. All subsequent image processing analyses are running on the selected ROI, exclusively.

Pre-Processing

In a pre-processing step, the image intensity of the RGB image is adjusted using the built-in function `imadjust` and a gamma value of 0.3, where gamma specifies the shape of the curve describing the relationship between the input and output image. This value gave the best results for all investigated rock mass outcrops, even under daylight conditions. Subsequently, the matrix of the input image is subtracted from the one of the output image, in order to sharpen contrasts and edges.

Further on, the adjusted image is sharpened by high-boost filtering (Gonzalez & Woods, 2018). The unsharping mask (`imsharpen`) has a standard deviation of the Gaussian lowpass filter (radius) of 5 and a strength of the sharpening effect of 4.5 (amount). This high value leads to a larger contrast increase of the sharpened pixels. The minimum contrast (threshold), required for a pixel to be considered an edge pixel, was set to 0.2. In subsequence, the RGB image is transformed into greyscale (`mat2gray`). A greyscale image is a topographic representation of the exposed rock face according to its exposure to the light source (intensity). In a last step, outliers are filtered by using first a median (`medfilt2`) and a Wiener filter (`wiener2`). Both filters operate with a neighbourhood size of 6 × 6. A larger filter size lead to an excessive filtering and flattening of the input images.

The pre-processing steps are standard applications to improve the results from the subsequent analyses.

Edge Detection and Orientation Clustering

Changes in the morphology of a rock face lead to changing light and colour conditions and consequently also changes in the intensity, colour or texture values. These changes can be detected as so-called edges and lines (Reid & Harrison, 2000, Lemy & Hadjigeorgiou, 2003, Gonzalez & Woods, 2018). According to Lemy & Hadjigeorgiou (2003), the Canny edge detector (`edge`) provides good and robust results and is therefore applied here.

The edge detection is performed on the pre-processed intensity image. The processed image is denoted as the matrix **e**. As a novelty, only edge segments with an eccentricity larger than 0.99 and longer than the 75 %-quantile (`regionprops`, `quantile`) of all detected line segments (LS_l) are used, to calculate the line segment orientation (ψ). The eccentricity (E) [0; 1] is calculated by an ellipse that has the same second-moments as the surrounding region and is the ratio of the distance between the foci of the ellipse and its major axis length. The higher the eccentricity, the higher is the elongation or linearity of a segment. The length, or ‘Area’, is represented by the number of connected white pixels. The orientation of the line segment is defined as the inclination of the ellipse against the horizontal line (Figure 2.1). Tests showed that it is sufficient, to allow for a lower edge length (75 %-quantile) at a still high linearity (0.99). However, too short line segments would increase the noise and hence blur the results.

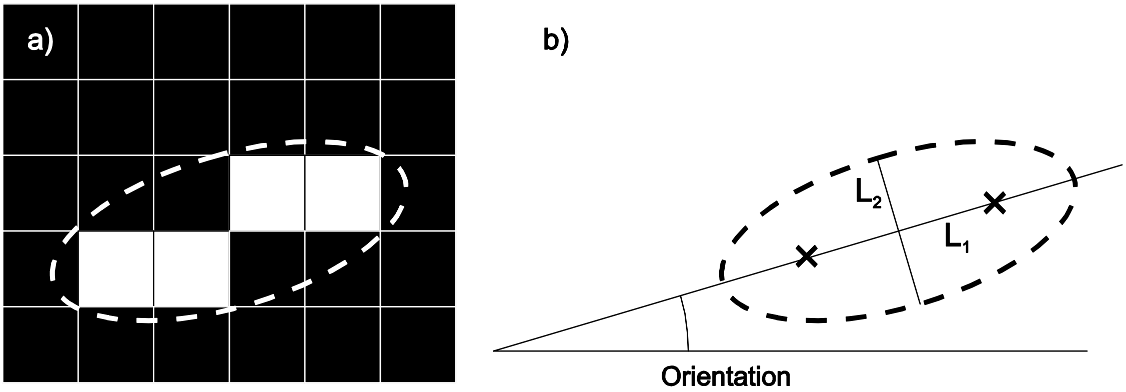

Figure 2.1: a) Fitted ellipse (dashed white line) onto a trace of four white pixels (= area, or length), surrounded by black pixels; b) the resulting ellipse (dashed black line) can be described by its eccentricity according to its two main axes (L_1/L_2) and its foci points (black crosses), as well as its orientation (ψ.

From the orientation values, a kernel smoothening function is calculated (`ksdensity`). The function calculates the probability density function (PDF) of the orientation values for each line segment. The number of investigated points was set to 180, since the orientation data is given in a range of [-90°; 90°] in steps of 1°. 0° indicates the horizontal line. The local peaks (l_{PK}) and minima (l_{MIN}) are localized (`findpeaks`) for a primary identification of dominant segment orientations. The peak orientations of the primary orientation filtering are used to apply a rotating correlation filter ($\mathbf{f}_{\mathbf{corr}}$, `imrotate`). The matrix of the correlation filter mask ($\mathbf{f}_{corr}(i,n)$) is displayed in equation 2.1. This step is necessary for the innovative application of an orientation dependant correlation filter to detect principal orientation cluster in the detected edges.

$$f_{corr} = \begin{bmatrix} -5 & -5 & -5 & -5 & -5 & -5 & -5 & -5 & -5 \\ -5 & -5 & -5 & -5 & -5 & -5 & -5 & -5 & -5 \\ -5 & -5 & -5 & -5 & -5 & -5 & -5 & -5 & -5 \\ 1 & 1 & 1 & 1 & 1 & 1 & 1 & 1 & 1 \\ 5 & 5 & 5 & 5 & 5 & 5 & 5 & 5 & 5 \\ 1 & 1 & 1 & 1 & 1 & 1 & 1 & 1 & 1 \\ -5 & -5 & -5 & -5 & -5 & -5 & -5 & -5 & -5 \\ -5 & -5 & -5 & -5 & -5 & -5 & -5 & -5 & -5 \\ -5 & -5 & -5 & -5 & -5 & -5 & -5 & -5 & -5 \end{bmatrix} \qquad (2.1)$$

Alternative mask sizes, e.g. 5 × 5, 7 × 7 or 12 × 12 have been tested as well and it was found that the larger the correlation mask, the more joint orientations are blurred. In contrast, the smaller the mask, the more noise appears in the measurements. However, the best results were obtained with a 9 × 9 pixel dimension. The correlation filtering is applied on the binary image matrix (**e**) from the edge detection and is morphologically post processed by infinite thinning (`bwmorph`, eq. 2.2). i is a placeholder for the number of the orientation peak from the primary peak detection and n is the detected peak value at i.

$$\boldsymbol{g} = \sum_{i=1}^{n} bwmorph(\boldsymbol{e} \otimes \boldsymbol{f}_{\boldsymbol{corr}}(i,n),'\,thin','\,inf') \tag{2.2}$$

The resulting matrix **g** is a sum of all orientation dependant correlation images and from this matrix, again only line segments longer than the 75 %-quantile are selected. Like previously, the 75%-quantile threshold was chosen in order to allow for shorter line segments but simultaneously avoid too much noise. Additionally, remaining branch points, where two line segments intersect, as well as line segments consisting of less than three pixels are excluded from the following determination of the secondary orientation filtering. This second determination defines the boundaries ($\alpha_{l,P}$ and $\alpha_{u,P}$) for the single orientation clusters according to the eq. 2.3 and 2.4. If the orientation values of the first peak, max(l_{PK}), and last peak, min(l_{PK}), express an absolute difference greater or equal to 162°, both peaks are regarded as one cluster (eq. 2.5).

$$a_{l,P} = \begin{cases} min\,(\psi),\ i = 1 \\ l_{MIN}(i-1), i \in [2, n] \end{cases} \tag{2.3}$$

$$a_{u,P} = \begin{cases} l_{MIN}(i1), i \in [1, n-1] \\ max\,(\psi), i = n \end{cases} \tag{2.4}$$

$$|max\,(l_{PK}) - min\,(l_{PK})| \geq 162° \tag{2.5}$$

for $i = [1, n_{PK}]$
n_{PK} *= number of detected peaks after the second orientation filtering*

From this primary orientation filter (= selection of all orientation values between $\alpha_{l,P}$ and $\alpha_{u,P}$), the median trace orientation (MTO) and the corresponding standard deviations (ς) are calculated. All values between the second orientation boundaries (eq. 2.6) are then assigned to one orientation cluster, assuming Gaussian deviation of the orientation values:

$$\alpha_{l,\sigma}/\alpha_{u,\sigma} = MTO \pm n \cdot \varsigma \tag{2.6}$$

n is set to 2, to include at least 95.4 % of all orientations within one cluster (assuming a Gaussian deviation). For the final extraction of line segments, a threshold for a minimum element length was chosen of at least the 85 %-quantile of all line segments in the specific cluster and a minimum segment eccentricity of 0.99 is applied. The workflow of the two orientation filter processes is displayed in Figure 2.2.

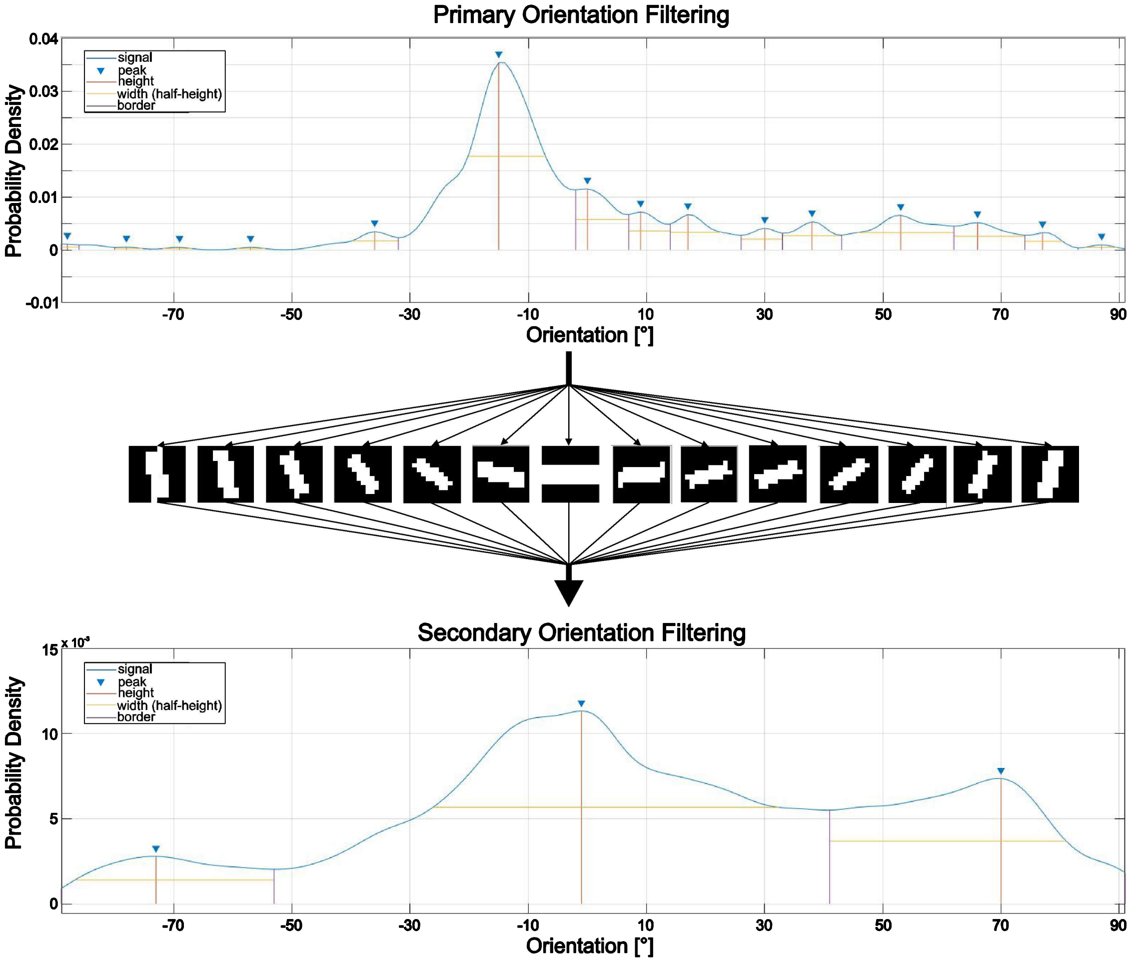

Figure 2.2: Exemplary workflow between the primary and the secondary orientation filtering as well as the application of the rotating correlation mask, based on the peak values (blue triangle) in the upper PDF distribution (primary orientation filtering); the resulting distribution of orientation values is displayed in the lower PDF plot (secondary orientation filtering).

Segment Linking

After identifying the single clusters, adjacent endpoints are linked in order to reduce the total number of single line segments and increase the segment length. The process is split into local linking (operating over distances from 1 to 50 Pixel), which shall link closely neighbouring segments, and regional linking, which links remoter line segments (operating from distances between 51 and 150 Pixel). The distance for the first local linking has been chosen due to the face that over short distances a straight line will more likely follow a straight line than over longer distances. A longer distance will probably not represent the course of a natural joint trace. The distance threshold of the secondary linking has been chosen accordingly. However, since the grey weighted distance transformation is following curvilinear intensities, it can represent the natural joint trace properly. But, once the distance is too large, it was found in test series, that false links are made despite the chosen heuristics. However, both values are heavily dependent on the image resolution and influence also the computation time.

The locally operating linking process is controlled by:

- a maximum Euclidean distance (d_{ss}),
- a maximum angular deviation (β_{sl1}) from the global set orientation,
- a minimum correspondence value (n_{corr}), determined by the number of identical points of the canny edges with the connecting line.

The maximum Euclidean distance was set to 50 Pixel. The maximum angular deviation for the first linking process (β_{sl1}) was fixed to 7.5°. The level of correspondence was set to 0.5. The chosen parameters produced robust results in each investigated case, including quarry faces and natural rock slopes.

To find and connect neighbouring points (training data) to the query data, an innovative implementation of a classic range searching algorithm was applied (`rangesearch`): From all line segments in one orientation cluster the coordinates of the associated end points (`bwmorph`), as well as the single line orientations are determined stepwise and used as query data. In case no neighbouring point is found, the next two neighbouring points – regardless of d_{ss} – are searched (`knnsearch`). If the distance criterion is fulfilled, a straight line, using the Bresenham's line algorithm, is drawn between the corresponding endpoints (Wetzler, 2010). The segments are connected by the bresenham-line, if the angular deviation of the linking segment, compared with the query orientation, does not exceed β_{sl1} and if at least 50 % (n_{corr}) of the coordinates of the dilated bresenham-line (disc shaped dilation mask, with a radius of 2 Pixel) are also existing in the canny edge image. In case the neighbouring points are closer than 10 Pixel, β_{sl1} is increased by the factor 2. Finally, the obtained line segments are morphologically thinned.

As a second and novel linking stage, the grey-weighted distance transformation (Soille, 1994) is used to link remote line segments by searching the shortest distance between two points, following an optimum and curvilinear path. In general, the distance transform of a binary image gives the distance from each foreground pixel in a background of zeros to the next neighbouring non-zero pixel and refers to this distance as a cost function (Szeliski, 2011, Gonzalez & Woods, 2018). In a grey-weighted distance transform, the cost is defined as the sum of the grey-level values along a path between two seed points in an intensity image, which is necessary to cover the distance. The minimum cost path between the two points is defined as the smallest amount of added intensity values, allowing to link these points (Soille, 1994). Consequently, a line is drawn between the two seed points, which is following the least cost path as a curvilinear connection. The approach is similar to the proposed method from Thiele et al. (Thiele et al., 2017), but instead of Dijkstra's algorithm, the Matlab-function `graydist` is applied to find the shortest path with the least cost between two seed points. The seed points are the starting and endpoints of two disconnected line segments within one orientation cluster. However, in order to avoid false positives, the following criteria must be fulfilled:

- Only the five closest line segment to the query point (`knnsearch`, within a Euclidean distance between 51 and 150) are used to compute the grey distance transform in order to find a connecting path between the points. Again, the number of pixel (‘Area’), along with its eccentricity and orientation are stored in a matrix.

- Only linking paths with an orientation, deviating less than a certain threshold (β_{sl2}), are selected. In this case, β_{sl2} was set to 12.5°. Furthermore, if the eccentricity was lower than 0.995 the path was deselected for the linking process.

β_{sl2} has been chosen due to the fact, that the grey-weighted distance transformation is working on a larger distance than the first linking algorithm. Therefore, a wider searching angle seems reasonable. But still, the main objective is to link interrupted line segments and a too large deviation is rather unrealistic under the assumption that a joint trace is rather a straight line than a zigzag line. Furthermore, the linkage can be curvilinear, but should not be too arched and the threshold for the eccentricity was set to 0.995. In case there are more than two possible linking partners, fulfilling the criteria above, the link with the longer distance is chosen. This generates generally longer line segments, which result in a better determination of the plane orientation. Likewise, if both linking partners are equal in distance from the starting point, the one with the higher eccentricity is chosen.

Due to the possible overlap of a linking path with an already existing line segment, the generation of new branchpoints cannot be avoided. Such features need further post-processing: each connected component (`bwconncomp`, connectivity of 8) with an eccentricity lower than 0.999 and an area higher than 50 Pixel is seen as a false positive and hence needs to be morphologically post-processed (disc-shaped dilation, r = 50 Pixel, followed by thinning). Again, the high value for E is chosen to process only the most linear signals. The radius for the dilation mask ensures the elimination of minor branches due to segment overlapping from the previous segment linking stages. However, a larger disc would also affect the natural course of the joint trace and changes it into a straight line.

Finally, line segments consisting of less than 50 Pixel are deleted from the 2D trace map and a 2D structure map is generated for the geotechnical application in ShapeMetriX^{3D}. This threshold length has been chosen to eliminate noise in the orientation measurements, since it is more difficult to fit a unique plane into a short string of spatially separated points, than into a longer one. The single line segments per cluster are considered as joint traces and, for maximum accuracy, the position of every white pixel along one single line segment in the resulting matrix are written into a SMX readable file-format (*.jmm). All further analyses, e.g. calculation of the spacing, or the determination of the discontinuity orientation, are performed in ShapeMetriX^{3D} Analyst. The implementation of a 2D structure map in ShapeMetriX^{3D} has basically been programmed for a fast on-sight application but has never been used in the context of automatic 2D image analyses to derive information about the joint network geometry.

2.1.2 Joint Plane Detection

As a second source of information the point clouds of each investigated rock face are analysed with the Discontinuity Set Extractor and ShapeMetriX^{3D} according to Riquelme et al. (2014) and Buyer & Schubert (2017). The Discontinuity Set Extractor (DSE) is a well-known tool for a semi-automatic and vector-based 3D point cloud analyses, in order to identify joint sets and joint planes. A clear description of the application is given in Riquelme et al. (2014). In a short summary, the method consists of three steps, which are (I) the calculation of the local curvature and the identification of planes, (II) the user-supervised and statistical analysis of the detected planes and (III) the actual cluster analysis. The methodology can be applied on 3D point clouds of any size. In the first step, a specific number of nearest neighbouring points (k) is searched to define the curvature and identify distinct planes in the point cloud. The analyses include a co-planarity test, to determine plane borders and the computation of the plane normal vectors. In a second step the user will decide, whether the automatic joint set identification, according to the distribution of the normal vector orientations in the stereographic projection, is acceptable, or if some results have to be omitted. This step is performed manually by the inspection of the density distribution of the normal vectors, belonging to the detected planes, in a stereo graphic projection. This leads to the definition of the orientations of the principal poles. The automatic joint set identification is controlled by the peak values of the density distribution of the orientation values. In the last step, the DBSCAN-algorithm (Ester et al., 1996) is used to cluster points, belonging to one joint set, into distinct groups, representing joint set planes.

For the analyses, the DSE version 2.08 (2018) is used. The configuration parameters for the DSE analyses are given in Table 2.1. Sensitivity analyses, regarding the input parameters on the data of Case Study I and II, were performed by Buyer et al. (2017) and Preiner (2018). The number of joint sets was kept at the default value (10), since the measurements are re-clustered in a post processing step, and by this, a higher number of measurements can be collected. The same counts for the cone of clustering (40°). Nonetheless, orientation clusters with very low densities were deleted manually according to their density distribution of the normal vectors in the density contour plot. The minimum number of points, which define a plane, was set to 50, in order to reduce noise.

Table 2.1: Calibration parameters for the vector-based discontinuity analysis with DSE, based on the sensitivity analyses of Buyer et al. (2017) and Preiner (2018).

Calibration parameter		Calibration value
number of neighbouring points	[-]	30
orientation tolerance	[-]	0.2
resolution of the KDE	[-]	512
minimum angle between joint sets	[°]	30
maximum number of joint sets	[-]	10
cone of the clustering	[°]	40
$k(\varsigma_s)$	[-]	1.5
min number of points to form a plane	[-]	50

The results of the discontinuity identification with DSE are transferred into SMX, according to Buyer & Schubert (2017). In summary, the single joint planes of each set are searched in the DSE output file, along with their normal vector orientation and set ID. From these points, the boundary points are searched using the Matlab-function `boundary`. Doublets are deleted by applying the function `unique`. Afterwards, the unique boundary points are sorted clockwise by projecting the points on the x-z-plane and select the coordinates accordingly. From the joint set planes also the midpoints are computed.

2.1.3 Conjunction of the Structure Maps

After the generation of the joint trace map (2D, sub-section 2.1.1) and the joint plane map (3D, sub-section 2.1.2) both structure maps are merged with SMX Analyst v.4.3. This innovative step enables to use the advantages of both sources of information and reduces the underlying bias, like the inability of JPD to detect joint traces as well as the inability of JTD to identify joint planes and determine the spatial orientation of the structures. Since both structure maps consist of pre-clustered structures, a re-clustering regarding the orientation measurements is necessary. This step is performed by the k-means algorithm, implemented in SMX Analyst. The partitioning and determination of the optimum number of clusters is determined by the examination of the angular distances between each orientation measurement. If the angle exceeds the vectorial sum of the spherical aperture plus the cone of confidence of each set, the partitioning is counted as statistically significant. The re-clustering specifications are given in Table 2.2. The clustering results consider a weighting of the structure sizes. The weighting factor is related to the size of the maximum diameter of the corresponding structure. The optimum results are chosen either by the optimum clustering result of the k-means analysis or other suggested clustering possibilities like the Fuzzy Hypervolume, the Partition Density (3GSM GmbH, 2018).

Table 2.2: Calibration parameters for conjoining the structure maps via re-clustering with the k-means algorithm, implemented in SMX Analyst.

Calibration parameter		Calibration value
Cluster Count	[-]	Between 1 and 10
Membership angle	[°]	60
Confidence level	[%]	95

Since it is possible that a structure is detected both as a planar feature and a trace feature, doublets can exist in the structure map. These doublets can lead to an underestimation of the actual set spacing (X_S) or the generation of too many fractures in the DFN. To avoid this the merged structure map is searched for doublets. For each base point of a structure within one set the next nearest neighbour base point is searched (`knnsearch`). If the neighbouring structure is co-planar, e.g. the angle (θ) between the plane normal vectors and the distance of the corresponding basepoints are below a user-defined threshold, the larger structure element is selected and the smaller deleted. The angular deviation is computed according to equation 2.7. For the distance threshold a distance of 20 cm was used at a maximum angular deviation of 7.5°.

$$\theta = arctan2d^{-1}\left(\frac{|\vec{\boldsymbol{u}}\times\vec{\boldsymbol{v}}|}{\vec{\boldsymbol{u}}\cdot\vec{\boldsymbol{v}}}\right) \tag{2.7}$$

$\vec{\boldsymbol{u}}$ = *plane normal vector of plane i [°]*
$\vec{\boldsymbol{v}}$ = *plane normal vector of plane j [°]*
θ = *angle between normal vector* $\vec{\boldsymbol{u}}$ *and* $\vec{\boldsymbol{v}}$

When generating the DFN (sub-section 2.3.2), fractures which are neighbouring less than 15 cm and deviate less than 10°, are aligned into one common plane.

2.1.4 Representation of Joint Size and Origin

An important parameter to describe a discrete fracture is its size. As described in sub-section 1.3.2, it is extremely difficult to assign numbers to this parameter. Strouth & Eberhardt (2006) approximate the joint size by the maximum apparent trace length of joints (L_a) in an exposed rock face and accept this value as a minimum joint size. In contrast, Priest (1993) suggest the use of statistical approaches to derive the joint size distribution from the joint trace length distribution. Both approaches have the use of the joint trace length in common.

This thesis proposed an innovative combination of both techniques: Since the number of identified joint structures is extremely high an empirical cumulative probability of the joint size distribution per set can be computed. For this, the maximum distance between all boundary points of a structure element is searched (`max`, `pdist`). This distance is seen as the apparent joint trace length (L_a). For statistical reliability the calculations are performed for all structure elements within one joint set and the cumulative density distribution (CDF) for each set can be computed using the kernel smoothening function (`ksdensity`). In order to describe the joint network in terms of variables the empirical CDF (eCDF) is used to find an analytical function, approximating the eCDF. The function (aCDF) is approximated by an exponential fitting function (eq. 2.8, Figure 2.3) using the `fit`-function in Matlab. `fit` finds the optimum values for the constants *a*, *b*, *c* and *d*.

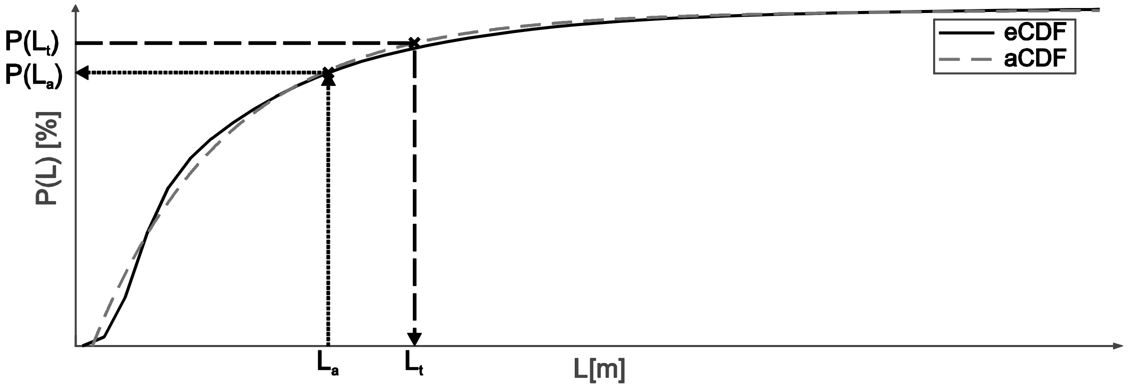

Figure 2.3: Exemplary CDF for on joint set, the empirical probability distribution (eCDF) is displayed as a solid black line, the corresponding fitted exponential function (aCDF) is displayed as a dashed black line, the apparent joint size (L_a) and the corresponding quantile value $P(L_a)$ is marked with a narrow dashed line, the theoretical cumulative probability, $P(L_t)$, and the corresponding theoretical joint size, L_t, is displayed in wide dashed blue line.

The success of the fitting is evaluated with the value for the root mean square error (RMSE) and coefficient of determination (R^2).

$$P(L) = a \cdot e^{b \cdot L} + c \cdot e^{d \cdot L} \tag{2.8}$$

A test series showed, that a better curve fitting is achieved with the double-exponential function than with a sigmoid or Weibull-function. Furthermore, using this equation a parametric description of the joint size distribution in a joint set is possible. To decide, whether the apparent joint size L_a is increased or not, a theoretical cumulative probability, $P(L_t)$, is generated. $P(L_t)$, which is based on a uniform distribution and ranges between 0 and 1, is then compared with the probability of $P(L_a)$ according to equation 2.8.

In case $P(L_t)$ is smaller than $P(L_a)$, the joint size and origin (base) of the structure element remain unchanged. In case $P(L_t)$ is bigger than $P(L_a)$, $P(L_t)$ is used to compute a theoretical joint size L_t according to equation 2.8 ($P(L) = P(L_t)$, solved against x_t, Figure 2.3). The base of the DFN fracture is also changed according to the new disc radius (r_1, eq. 2.10). The new origin can move only along the perpendicular and normalized vector ($\overrightarrow{\mathbf{V_3}}$) to the normal vector of the joint plane ($\mathbf{V_2}$) and the vector between the most distant boundary points ($\overrightarrow{\mathbf{V_1}}$), but in two directions (eq. 2.11 and 2.12). The length of the vector is the square-root of the difference between the squared new disc radius (r_1) and r_0 (eq. 2.9). The concept is displayed in Figure 2.4. The probability for $\mathbf{O_1}$ or $\mathbf{O_2}$ is 50 %.

$$r_0 = \frac{|\overrightarrow{V_1}|}{2} \tag{2.9}$$

$$r_1 = \frac{P(x_t) = n_{xt}}{2} \tag{2.10}$$

$$\overrightarrow{\boldsymbol{V_3}} = \frac{\overrightarrow{\boldsymbol{V_1}} \times \overrightarrow{\boldsymbol{V_2}}}{|\overrightarrow{\boldsymbol{V_1}} \times \overrightarrow{\boldsymbol{V_2}}|} \tag{2.11}$$

$$\overrightarrow{\boldsymbol{O_{r,v}}} = |\overrightarrow{\boldsymbol{V_3}}| \cdot \sqrt{r_1^2 - r_0^2} \tag{2.12}$$

$$\boldsymbol{O_1} = \boldsymbol{O_0} + \overrightarrow{\boldsymbol{O_{r,v}}} \text{ and } \boldsymbol{O_2} = \boldsymbol{O_0} - \overrightarrow{\boldsymbol{O_{r,v}}} \tag{2.13}$$

r_0 = original disc radius [m]
r_1 = disc radius according to eq. 2.9 with quantile value of n_{xt} [m]
$\overrightarrow{\boldsymbol{V_1}}$ = Vector between the two most distant boundary points
$\overrightarrow{\boldsymbol{V_2}}$= normal vector of plane i
$\overrightarrow{\boldsymbol{V_3}}$= perpendicular vector to $\overrightarrow{\boldsymbol{V_2}}$ and $\overrightarrow{\boldsymbol{V_3}}$
$\overrightarrow{\boldsymbol{O_{r,v}}}$ = vector with a length of $\sqrt{r_1^2 - r_0^2}$ to move from O_0
$\boldsymbol{O_0}$ = original joint origin (base)
O_1 and O_2 = new joint origin after increasing its size

This concept for describing a joint size distribution is new in rock engineering and further application might show its applicability.

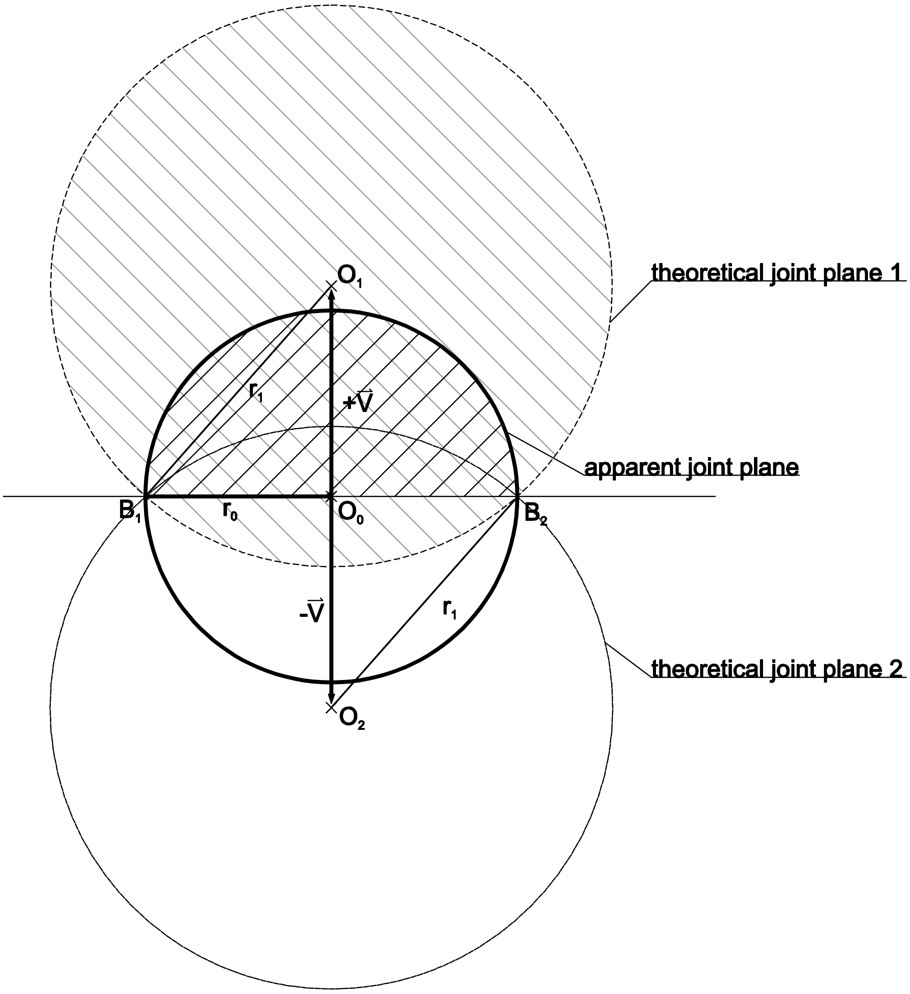

Figure 2.4: Considerations on the joint size (2D, disc shaped) regarding the apparent joint plane (bold circle in the centre) with the radius r_0 and origin $\mathbf{O_0}$; once the joint size is increased (considering an increased radius r_1), the origins of the new joint planes ($\mathbf{O_1}$ and $\mathbf{O_2}$) deviate from $\mathbf{O_0}$ and can lie on both sides of the reference line, drawn between the boundary points $\mathbf{B_1}$ and $\mathbf{B_2}$; the new origins ($\mathbf{O_{1/2}}$) are computed by moving $\mathbf{O_1}$ or $\mathbf{O_2}$ along the normal vector ($\pm \vec{\mathbf{V}}$), which is perpendicular to the plane normal vector and $\overrightarrow{\mathbf{B_1B_2}}$.

2.2 Rock Mass Geometry

The better a joint network is mapped, the better is the resulting description of the rock mass geometry. Herein, a higher quantity of the measurements reduces the influence of outliers and increases the accuracy of the results. The description of the joint network geometry with standard parameters like joint set orientation, spacing and trace length is described in sub-section 2.2.1. The methodology for obtaining and characterizing the resulting rock mass and block geometry is described in sub-section 2.2.2.

2.2.1 Joint Network Geometry

For describing the joint network geometry, ShapeMetriX3D – SMX Analyst (v4.3) is used. The joint network geometry is described by the statistical representation of the following parameters, using the Multiple-Scanline Analysis in SMX Analyst (3GSM GmbH, 2018):

- joint set orientation: the orientation values are given with the mean set orientation values, the cone of confidence (CoC), the degree of orientation (DoD) and the spherical aperture (SA) (Wallbrecher, 1986, 3GSM GmbH, 2018).
- joint set normal spacing (X_S): the values are given with the mean, the median and the corresponding standard deviation.
- apparent joint trace lengths (L_a): the values are given with the mean and the median joint trace length as well as the corresponding standard deviations.
- joint set frequency (linear fracture intensity, P_{10}).

The statistical joint size distribution is determined according to sub-section 2.1.4.

2.2.2 Block Geometry in the Rock Mass

The IBSD is derived directly from the DFN, generated in 3DEC (Söllner, 2014, Preiner, 2018, Aichinger, 2018). However, only the volumes of blocks inside the DFN region are exported and used to compute a cumulative size distribution. Since the generation of the DFN is a rather deterministic representation of the joint network, a repetition of the calculations, like suggested in Söllner (2014), was not deemed relevant for a representative deviation of the IBSD. The results are displayed as the CDF in a semi-logarithmic plot. The block shape distribution is computed according to the approach after Kalenchuk et al. (2006) and Aichinger (2018), using the block edge coordinates along with the volume and surface information from 3DEC. The elongation (β) and flatness (α) are computed according to equation 2.14 and 2.15. The algorithm searches for corresponding block vertices, which have a distance larger than the median chord length of all inter-vertex distances and computes pairwise the squared scalar product between vector $\vec{a}$ and $\vec{b}$, as well as the squared vector norm of $\vec{\mathbf{a}}$ and $\vec{\mathbf{b}}$.

$$\beta = 10\left[\frac{\sum(\vec{a}\cdot\vec{b})^2}{\sum\|\vec{a}\|^2\cdot\|\vec{b}\|^2}\right]^2, \beta \in [1, 10] \tag{2.14}$$

$$\alpha = \frac{A_S \cdot \bar{l}}{7.7 \cdot V_B}, \alpha \in [1, 10] \quad (2.15)$$

$\vec{a}$ and $\vec{b}$ being vectors of corresponding block vertices
A_s = Block surface area [m^2]
$\bar{l}$ = mean vertex length [m]
V_B = Block volume [m^3]

To get a better idea about the dominant block shape in the rock mass a kernel density estimation (`kde2d`) according to Botev et al. (2010) is computed for all measurements.

As a further development in characterizing the block geometry, the 2D distribution of the block orientation (given in trend and plunge) is computed by the kernel density distribution. This value represents the 3D vector orientation of the longest inter-vertex chord of each single block in the numerical model. In case there are two or more inter-vertex chords with an equal length (like in a case of a cuboid), the vector orientation is computed by the mean of all orientation values. Again, the resulting density distribution is displayed in a stereographic projection (lower hemisphere, equal angle).

2.3 Numerical Rock Mass Modelling

With a sound knowledge about the joint network geometry and rock mass type it is possible to identify the rock mass behaviour e.g. with numerical analyses. This helps during the project design stage, anticipating the risk and providing adequate support (Goricki, 2003). Still, a numerical analysis is only as good as its underlying input-parameters. In the case of DCF, the ground behaviour is predominantly controlled by the joint network geometry, the joint properties and stress conditions. Therefore, the previously identified discontinuities are used to generate a deterministic rock mass model for analysing the actual block failure in relation to the actual excavation shape. The scope of this numerical analyses is not to find the real values for the joint and rock mass properties but rather to demonstrate the usefulness and applicability of the proposed method in block stability analysis. Hence, the sensitivity analyses are kept very simple and only a few parameters are varied.

2.3.1 General Model Layout

The numerical simulation for the block stability and the back calculation of the rock mass parameters in the selected tunnel sections is performed with the 3D distinct element code 3DEC (Itasca Consulting Inc.). The general model geometry considers a rectangular block with the coordinate ranges given in Table 2.3.

Table 2.3: Coordinates of the model boundaries and DFN-regions for the two case studies.

Model	Used for	X_{min} [m]	X_{max} [m]	Y_{min} [m]	Y_{max} [m]	Z_{min} [m]	Z_{max} [m]
Case Study I	Global	-25	30	-35	20	-10	30
	DFN	-15	15	-15	25	-10	10
Case Study II	Global	-27.5	27.5	-15	40	-10	30
	DFN	-10	10	-10	18	-10	10

The size of the global model boundaries, given in Table 2.3, is large enough to exclude boundary effects, like unbalanced stresses between fixed blocks at the boundary and moving blocks around in the tunnel periphery. The size of the DFN region is large enough to contain all mapped discontinuities.

The tunnel shape is modelled in both case studies according to the design cross-section, however, considering a full-face top heading excavation in compliance with the described excavation class. In order to limit the fractures, generated by the DFN, the general model is densified into smaller, but jointed, blocks.

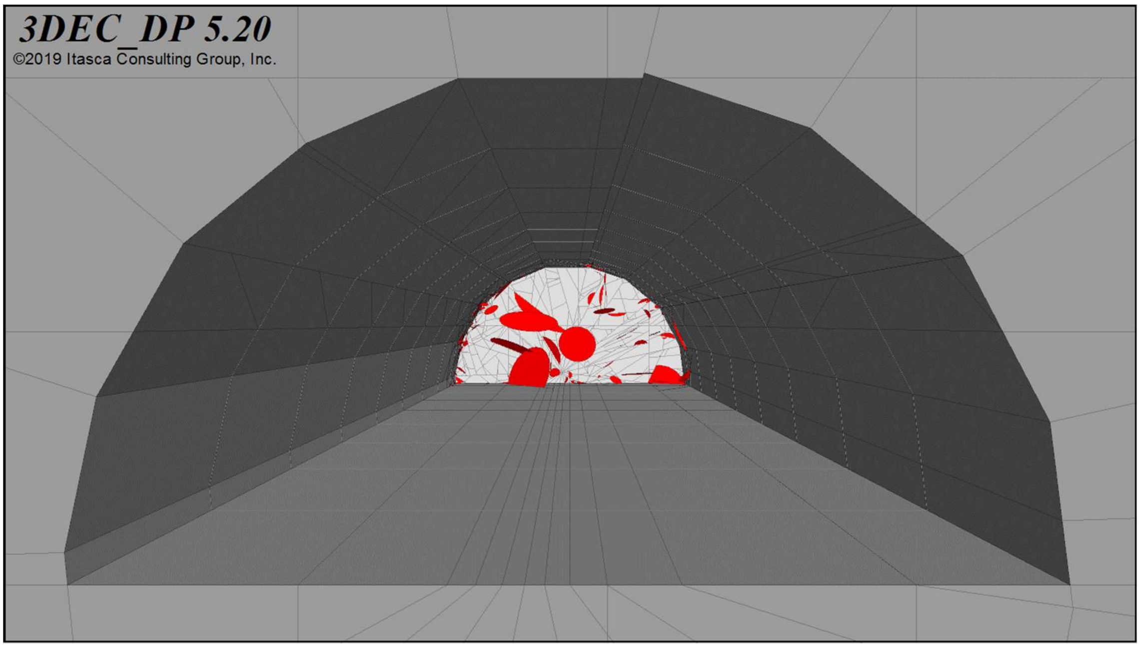

Figure 2.5: Model geometry (without joints) of the 3DEC model of Case Study I; the rock mass is coloured in grey consisting of several distinct blocks, the red discs indicate the position of the discrete fractures, used to generate the joint network.

The tunnel axis in Case Study I points towards north (Figure 2.5). In Case Study II, the tunnel axis has a trend of 150° and a plunge of 0°. These values are chosen according to the project information of each case study. In order to reconstruct the documented tunnel face, the tunnel is excavated in both case studies according to the project documents in round lengths of 2.2 m with a top heading sequence. The invert is not excavated.

The primary stress conditions in both case studies are modelled according to the overburden at the chosen cross-sections (Table 3.1 and Table 3.11). For the ratio between the principal stresses (K) a parameter study was performed: K was fixed to 0.33 in Case Study I, due to the low overburden and the open joints, as denoted in the project documents. In Case Study II, K was changed from 0.33 to 0.66 and 1 in order to investigate the influence of the stress conditions on the excavation profile, respectively the total volume of blocks moving more than 1 cm. In both cases gravitational load is applied ($g = -9.81$ m/s²). The orientation of the primary stresses σ_1 and $\sigma_{2/3}$ correspond to the vertical and horizontal axis. The joint network is modelled as a discrete fracture network (DFN), linked directly to the joint network characterization in section 2.1. Each numerical analysis is split into five computation sequences (Table 2.4, Figure 2.6)

Table 2.4: Simulation sequences in the numerical analyses according to the different stress states (PSS, primary stress state; SSS, secondary stress state) and the used calculation steps and the maximum ratio (R) of unbalanced forces; the station of interest (SOI) is the station, where the joint network geometry is mapped.

Sequence	Description	Solving Steps
PSS	Computation of the primary stress state	$R \leq 1 \cdot 10^{-6}$
SSS-1	Excavation of the rock mass until 4.4 m before the station of interest (SOI)	100,000
SSS-2	Excavation of the rock mass until 2.2 m before the station of interest (SOI)	100,000
SSS-3	Excavation of the rock mass until the SOI	150,000
SSS-4	Excavation of the rock mass 2.2 after the SOI	150,000

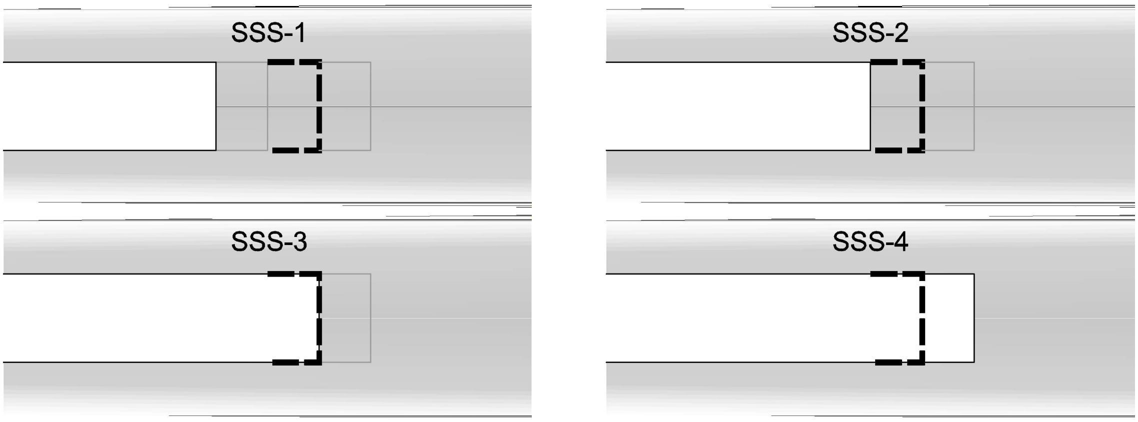

Figure 2.6: Depiction of the excavation sequences (SSS-1 to SSS-4) in the secondary stress state and the position of SOI (dashed bold line).

An equilibrium state was only desired in the first excavation sequence (PSS). Afterwards, only a limited number of calculation steps is necessary, to achieve the desired excavation profile and approximate the real excavation procedure. A lower maximum ratio of unbalanced forces would only increase the computation time significantly, since it requires a state, where all blocks have detached and none is still in the process of falling.

A geometry sensitive parameter is the general tolerance value (a_{tol}). It controls:

- the minimum distance between grid points,
- the tolerance to link grid points of jointed blocks,
- the tolerance to select vertices close to the command plane.

a_{tol} can be seen as a reference value for the minimum block size in the model. As written in sub-section 1.2.1, only blocks with a reference size of $5 \cdot 10^{-4}$ m³ ($V_{B,ref}$) are considered relevant. Hence, a theoretical model was built where a_{tol} was stepwise increased from 0.005 to 0.1, in order to determine an optimum value for a_{tol}, which results in a minimum block size according to the lower reference block size. The theoretical model had an edge length of 5 m. The joint set geometries are given in Table 2.5.

Table 2.5: Joint network specifications for the theoretical determination of an optimum general tolerance value a_{tol}.

Set ID	DD [°]	ς_{DD} [°]	D [°]	ς_{D} [°]	X_s [m]	ς_{xs} [m]
1	150	15	25	15	0.3	0.1
2	020	15	75	15	0.2	0.1
3	075	15	65	15	0.4	0.1
4	110	15	10	15	0.1	0.1

The persistence was set to 100 % to allow for the smallest block size. The optimum value for a_{tol} was selected when the 5 %-quantile value of V_B coincided with $V_{B,ref}$. This still allows the generation of smaller blocks ($V_{B,min}$), but the majority is larger than $V_{B,ref}$. Each computation was repeated three times, to include a slight variation of the results due to the standard deviations of the joint geometry properties. Although a statistical representation of variations in the joint set orientations are usually given with a Fisher distribution (Priest, 1993), 3DEC allows in its standard implementation of joint sets only the definition of mean orientations along with the corresponding standard deviation. The results are displayed in Figure 2.7 and listed in Table 2.6. The optimum value for a_{tol} was set to 0.06, since the resulting block sizes, especially $\overline{V_{b,5}}$ coincided with the reference block size.

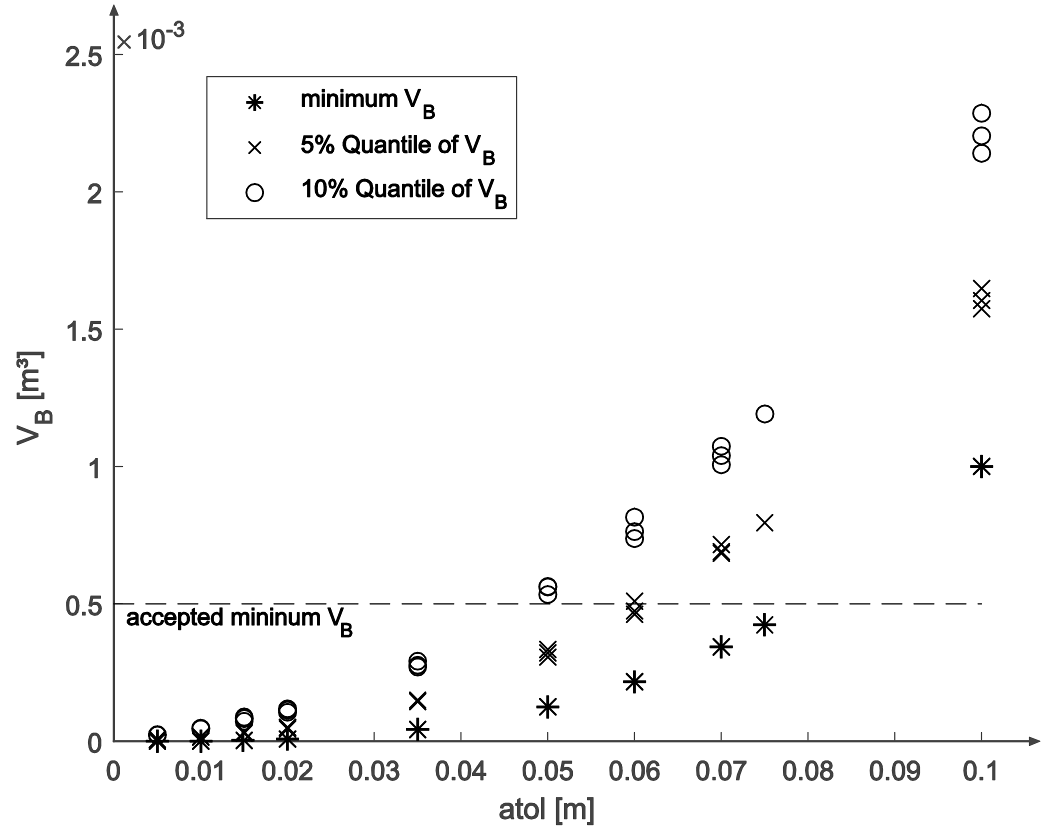

Figure 2.7: Varying block sizes resulting from different global tolerance values (a_{tol}); the dashed line represents $V_{B,ref}$, stars mark the global minimum V_B, crosses mark represent the 5 %-quantile of V_B, circles mark the 10 %-quantile of V_B.

Table 2.6: Resulting mean block sizes for varying general tolerance values (a_{tol}) of each replication, depending on the joint specifications according to Table 2.5; the optimum results are highlighted in bold letters; $\overline{V_{B,min}}$ represents the global minimum of V_B, $\overline{V_{B,5}}$ represents the 5%-quantile of the global V_B and $\overline{V_{B,10}}$ represents the 10 %-quantile of V_B.

a_{tol} [m]	$\overline{V_{B,min}}$ [m³]	$\overline{V_{B,5}}$ [m³]	$\overline{V_{B,10}}$ [m³]
0.005	$1.27 \cdot 10^{-7}$	$6.13 \cdot 10^{-6}$	$2.42 \cdot 10^{-5}$
0.01	$1.01 \cdot 10^{-6}$	$1.58 \cdot 10^{-5}$	$4.62 \cdot 10^{-5}$
0.01	$3.39 \cdot 10^{-6}$	$3.20 \cdot 10^{-5}$	$8.12 \cdot 10^{-5}$
0.02	$8.02 \cdot 10^{-6}$	$4.85 \cdot 10^{-5}$	$1.12 \cdot 10^{-4}$
0.035	$4.30 \cdot 10^{-5}$	$1.46 \cdot 10^{-4}$	$2.80 \cdot 10^{-4}$
0.05	$1.25 \cdot 10^{-4}$	$3.21 \cdot 10^{-4}$	$5.53 \cdot 10^{-4}$
0.06	$\mathbf{2.17 \cdot 10^{-4}}$	$\mathbf{4.82 \cdot 10^{-4}}$	$\mathbf{7.72 \cdot 10^{-4}}$
0.07	$3.44 \cdot 10^{-4}$	$6.97 \cdot 10^{-4}$	$1.04 \cdot 10^{-3}$
0.075	$4.24 \cdot 10^{-4}$	$7.96 \cdot 10^{-4}$	$1.19 \cdot 10^{-3}$
0.10	$1.00 \cdot 10^{-3}$	$1.6 \cdot 10^{-3}$	$2.21 \cdot 10^{-3}$

2.3.2 Generation of the Discrete Fracture Network

Numerical modelling of DCF is standard in rock engineering, if a discrete block failure is expected to be the dominant failure mechanism. However, the application of discrete fracture networks in stability analyses is seldom performed, since this requires either a good statistical model to describe the DFN in terms of joint orientation, size and position, or a very high number of measurements. In this thesis, an innovative approach is applied, directly using the information gained from the joint network characterization (sub-sections 2.1.3 and 2.1.4). This allows to explicitly consider the mapped discontinuities in the analyses and a statistical representation of the joint network geometry is redundant. Parameters, like the persistence are described by the disk size and deviations in the actual joint position or orientation are exactly like in the investigated rock face. This makes a direct comparison of the modelled excavation profile with the DSM of the tunnel face possible.

Each fracture is embedded as a disc shaped and planar joint with finite size. In detail, each captured structure element is written into a DFN file, along with its normal vector, origin (base) and size. Since the fractures are located at the investigated tunnel face, the DFN region is a cubic area around the position of the tunnel face with the boundary regions given in Table 2.3. With a_{tol} set to a relative high value (0.06 m, sub-section 2.3.1), cuts, leading to blocks below $V_{B,ref}$, are rejected. Furthermore, adjacent discontinuities were simplified. This means that single fractures, whose bases are closer than 0.15 m and have an angular deviation of less than 10° were aligned into one plane, with the bigger of the two compared disks as a reference.

2.3.3 Joint and Material Properties

The joint and material properties are selected according to the project documents (Table 3.2 and Table 3.12). The joint constitutive model for Coulomb slip failure and weakening (plastic deformation), implemented in 3DEC, is used. In the constitutive model a threshold for the maximum shear displacement (z_{dil}) must be given to define a transition-point between the intact and the residual joint properties. Bevor z_{dil} is reached, a joint can reach its maximum shear capacity with the given intact properties. However, once a shear displacement of more than z_{dil} has taken place, the residual values apply and the maximum shear capacity is lower (Figure 2.8).

Since block failure is expected rather than plastic block deformation, the blocks are considered rigid and the Mohr Coulomb constitutive model is applied. This also leads to the assumption of a negligible influence of variations in the joint normal stiffness (j_{kn}). It is therefore kept constant at $1 \cdot 10^{11}$ Pa/m. The joint shear stiffness (j_{ks}) was chosen with $1 \cdot 10^{10}$ Pa/m. Variations of j_{ks} were investigated, but did not show significant differences in the model behaviour.

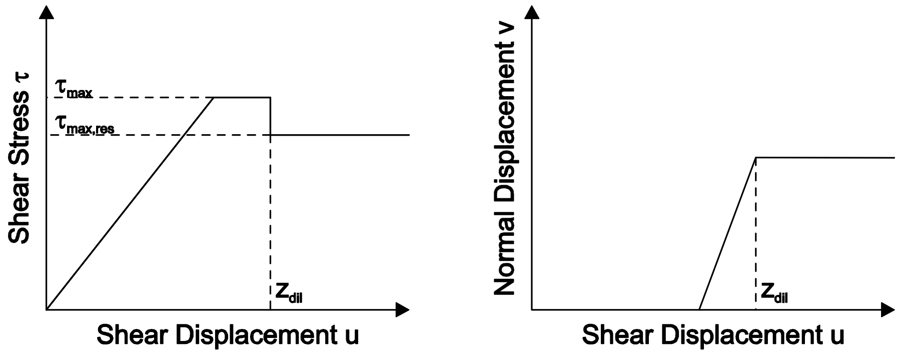

Figure 2.8: Influence of the threshold for the maximum dilation distance z_{dil} on the transition from the intact joint properties to the residual properties and the resulting maximum shear capacity ($\tau_{max,res}$).

Since the discrete fractures base on existing and exposed joint planes it is assumed that no rock bridges existed on those fractures at the point of detachment and hence zero cohesion and no tensile strength is assigned to the joint planes. The digital surface models (Figure 3.2 and Figure 3.13) in both case studies indicate that the identified fault structures are not connected to a decreased material stiffness in their vicinity, since the faults are not accompanied by caving structures. Hence, only one set of material properties is used.

Following Sofianos et al. (1999), the block geometry and the joint friction angle (φ) are seen as the most sensitive parameters for the tunnel stability. With the block geometry specified by the DFN, the influence of φ is investigated in three case studies. Starting from the values in Table 3.2 and Table 3.12, a higher (φ + 5°) and a lower friction angle (φ - 5°) is tested for its influence on the total block volume of blocks moving more than 1 cm ($\Sigma V_{B,0.01}$) as well as its visual effect on the excavation profile. The residual friction (φ_{res}) angle is adapted as well. Since the numerical model shall a priori demonstrate the applicability of the proposed methods a detailed sensitivity analysis, including a wider range of friction angles has been relinquished, with respect to the extensive computation times. Likewise, the influence of the dilation angle (ι) is also not investigated in a sensitivity analysis and is therefore kept constant. The sensitivity analysis is performed for each considered value of K.

2.3.4 Assessment of Discontinuity-Controlled Block Failure

The validation of the numerical results is based on the visual comparison of the modelled overbreak with the actual tunnel shape, as it was digitized with ShapeMetriX^{3D}. The actual tunnel shape is loaded into 3DEC as a *.dxf geometry and used as a reference excavation geometry. As a numeric indicator for the model sensitivity regarding K and φ, the total volume of blocks moving more than 1 cm ($\Sigma V_{B,0.01}$) is determined and compared for each simulation stage. The threshold of 1 cm has been chosen according to the maximum dilation distance, which marks the transition between the original (raised) and residual values for the joint shear resistances. A parameter is identified as model sensitive, if $V_{B,0.01}$ is increasing considerably, or if the point cloud of the real excavation profile visually overlays the modelled excavation profile.

This sensitivity analysis and back calculation of realistic rock mass and joint properties is only possible due to the extremely high detail of the joint network mapping. But a detailed joint mapping is not enough, if it cannot be used explicitly in a numerical model. Therefore, a site specific DFN is generated, which directly implements the joint specifications orientation and location for each single discrete fracture according to the structure map. The size of the fracture is specified according to a novel approach for statistically increasing the apparent joint trace length according to an analytical approximation of the empirical probability function of the measured joint traces per set. The application of a DFN, rather than a statistical deterministic rock mass model, allows the explicit reconstruction of the rock mass geometry as well as a site-specific block stability analysis.

But how is the performance of this theoretical approach under real conditions? Deliver the used algorithms enough data for a better understanding of the rock mass and do they allow for a deterministic block stability analysis? In the next chapter, two case studies under different rock mass conditions are used as application examples. The results are discussed in chapter 4.

3 Application Examples

In the following sections, two exemplary tunnel faces are investigated with the proposed method. The rock mass in both case studies is different. Case Study I (section 3.1) shows a very blocky rock mass with many exposed joint planes, but also lots of changes in colouring and shading. Therefore, a good performance of the JPD and a weaker performance of the JTD is expected. Case Study II (section 3.2) shows a foliated gneiss with minor exposed joint planes and block detachments in the roof section. Due to the lack of joint planes, a weaker performance of the JPD algorithm is expected, whereas the obvious foliation shall lead to a very good performance of the JTD. Nonetheless, by combining both approaches, a highly detailed joint network description and DFN is generated, since the strength of both information sources can be used and reduce the weaknesses of the single methods.

The results are subdivided first into the general description of the case study according to the digital mapping results (sub-sections 3.2.1 and 3.1.1), second the rock mass geometry (sub-sections 3.2.2 and 3.1.2) and third the numerical stability analyses (sub-sections 3.2.3 and 3.1.3).

3.1 Case Study I – Blocky Rock Mass

In a first case study the proposed methodology is applied on a tunnel face in a very blocky rock mass and a low overburden. The tunnel project and information sources are kept anonymous due to unresolved claims. The data consists of the geological documentation along with information from the exploratory program as well as a scaled SMX model (3D point cloud) of the selected station. The point cloud is not referenced to north and covers most of the outbreaks in the actual tunnel face, the side walls as well as in the roof section. The tunnel specifications are given in Table 3.1.

The chosen case study can be seen as a standard application for JPD due to the very distinct joint planes in the DSM (Figure 3.2) and the general ground type 1 (GT1) was assigned by the mapping geologist. However, in the lower right side of the tunnel face, classified as GT2 according to the project documents, a denser joint pattern can be seen in the form of joint traces (Figure 3.1). Still the chosen case study shall confirm the applicability and benefit of the proposed methodology.

As can be seen in Figure 3.1-a, the rock mass appears as very blocky and shows alternating degrees of weathering. The different states can be distinguished by their colour (grey in fresh and unweathered rock to brownish colours). The blockiness can be anticipated by the different shades. According to the project documents, two highly persistent discontinuities cross the tunnel face in the mid-section and in the right side. Figure 3.1-b is a geological sketch of the exposed tunnel face, taken from the project documents, and includes information about joint orientations, highlights areas of block detachments (hatching) as well as dominant joint traces. A minor overbreak is indicated in the right crown region. A direct comparison of Figure 3.1-a (photograph) with b (geological sketch) clearly shows the necessity of a scaled and referenced tunnel face model. Most of the structures in the sketch cannot be seen directly in the photograph due to the lack in spatial information. On the contrary, the actual tunnel profile and most of the joint structures, which are apparent in Figure 3.1-a are not drawn in the Figure 3.1-b. Hence a direct comparison is difficult.

Table 3.1: Specifications of the tunnel station in Case Study I according to the geological documentation and project documents.

Parameter		Unit	Value/Description
Overburden		[m]	20
Round length		[m]	2.20
Orientation of the tunnel face		[°]	000/90
Lithology		[-]	Granite
Density		[kg/m³]	2600
Rock Mass Type		[-]	
	GT1	[%]	85
	GT2	[%]	15
Documented joint sets		[-]	st, k1, k2, k3, k4*
Comments			Block detachments from the right-side wall, defined by highly persistent joint resp. fault, minor detachments from the left side wall, design profile can hardly be maintained

* st = Fault, k1…4 = joint set 1…4

According to the geological documentation, the rock mass mainly consists of a fine to coarse grained granite. The rock mass condition is according to the project documents generally good with a low degree of fracturing (GT1). GT2 is assigned to regions with a higher degree of fracturing than GT1. The joint properties are listed in Table 3.2. Since no detailed information is given about the shear resistance properties of the joints, reasonable values are selected in correspondence with the verbal description of the joints (e.g. Hoek et al., 1997). The particular values are marked with a star (*). Since the numerical model considers rigid blocks, no rock material properties, apart from the density, and no constitutive model for describing the stress strain relations are necessary.

Table 3.2: Joint geometry and properties according to the geological documentation and engineering judgement (e.g. Hoek et al., 1997) in Case Study I; the particular values are marked with a star (*).

Parameter		Unit	Fault (st)	Joint 1 (k1)	Joint 2 (k2)	Joint 3 (k3)	Joint 4 (k4)
Orientation	DD/D	[°]	098/70	302/87	348/60	151/50	038/72
Spacing	X	[m]	> 2	0.6 to 2	0.2 to 0.6	> 2	0.2 to 0.6
Surface description	-	[-]	Planar, smooth	Planar, smooth	Planar, rough	Planar, rough	Planar, rough
Persistence	P	[-]	high	high	medium	high	medium
Friction angle*	φ	[°]	22 ± 5	30 ± 5	40 ± 5	40 ± 5	40 ± 5
Residual friction angle*	φ_{res}	[°]	20 ± 5	25 ± 5	37 ± 5	37 ± 5	37 ± 5
Dilation*	ι	[°]	2	5	10	10	10
Cohesion*	c	[Pa]	$5 \cdot 10^5$	0	0	0	0
Residual cohesion*	c_{res}	[Pa]	$2.5 \cdot 10^5$	0	0	0	0
Maximum dilation distance*	z_{dil}	[m]	0.005	0.005	0.005	0.005	0.005

The joints are described as dominantly planar and smooth with values for the friction angle between 25° and 35° (GT1) and between 20° and 30° (GT2). A minor and local water inflow has been documented. The joints are almost closed with an aperture of less than 0.5 mm. The trace lengths range from 3 to more than 20 m. The rock mass has a low anisotropy with three to four joint sets (GT1) and more than four joint sets in GT2. The joint set spacing ranges between 20 and 60 cm (GT1), respectively 6 to 60 cm in GT2. The joint frequency is higher in the lower right part of tunnel face. The block shape is prismatic to rhombohedral. The rock mass behaviour is dominated by the joint network geometry.

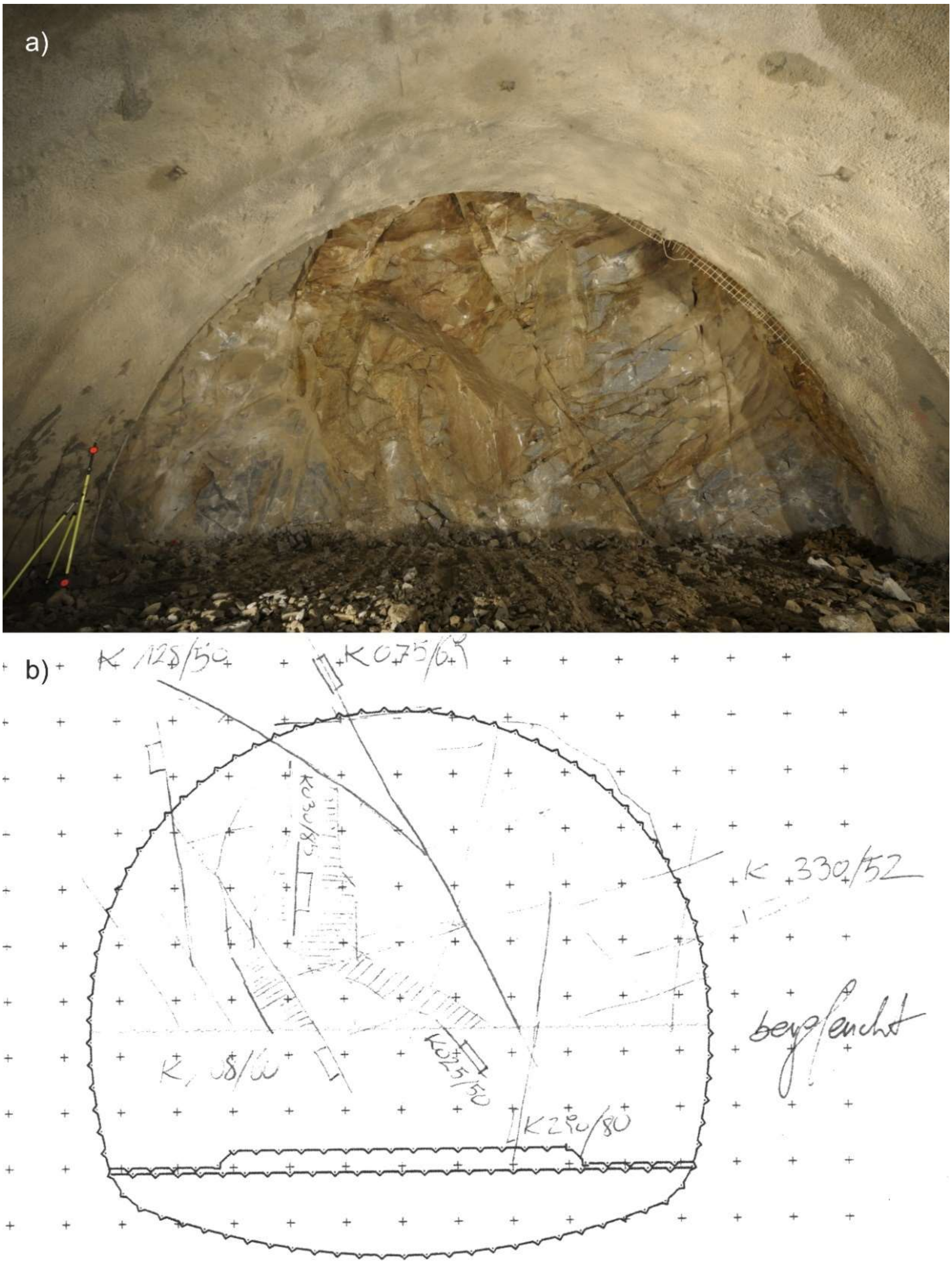

Figure 3.1: (a) Investigated tunnel face in Case Study I; the photograph shows the varying colours due to changes in the exposure to the light as well as weathering; the range pole in the lower left side is used for scaling the DSM in SMX, it has a height of 1.35 m; b) geological sketch of the exposed tunnel face, highlighting dominant joint traces with the corresponding Müller flags and orientation values; the sketch is projected on the design tunnel profile and shows a minor overbreak in the upper right side (dashed line outside the design profile).

The tunnel face was photographed with a calibrated DSL NIKON D300s at a focal length of 12 mm, mounted on a tripod, in order to generate a DSM of the tunnel face. Furthermore, the DSM and the photographs are directly coupled and a reference between each other is easy. The image resolution is 4288 x 2848 Pixel. The distance of the camera position and the tunnel face was 8.7 m. The average geometric image resolution can be approximated with 3 mm^2/pixel. The specifications of the 3D point clouds are given in Table 3.3. The shaded DSM is displayed in Figure 3.2.

Table 3.3: Statistical specifications of the 3D point cloud in Case Study I.

Parameter	Unit	Value
Number of 3D points	[-]	630274
Minimal area patch size for orientation measurements	[m^2]	0.004
Surface area (cut)*	[m^2]	244
Average 3D point spacing	[m]	0.02

* the surface model has been cut in order to exclude the lining from the analyses.

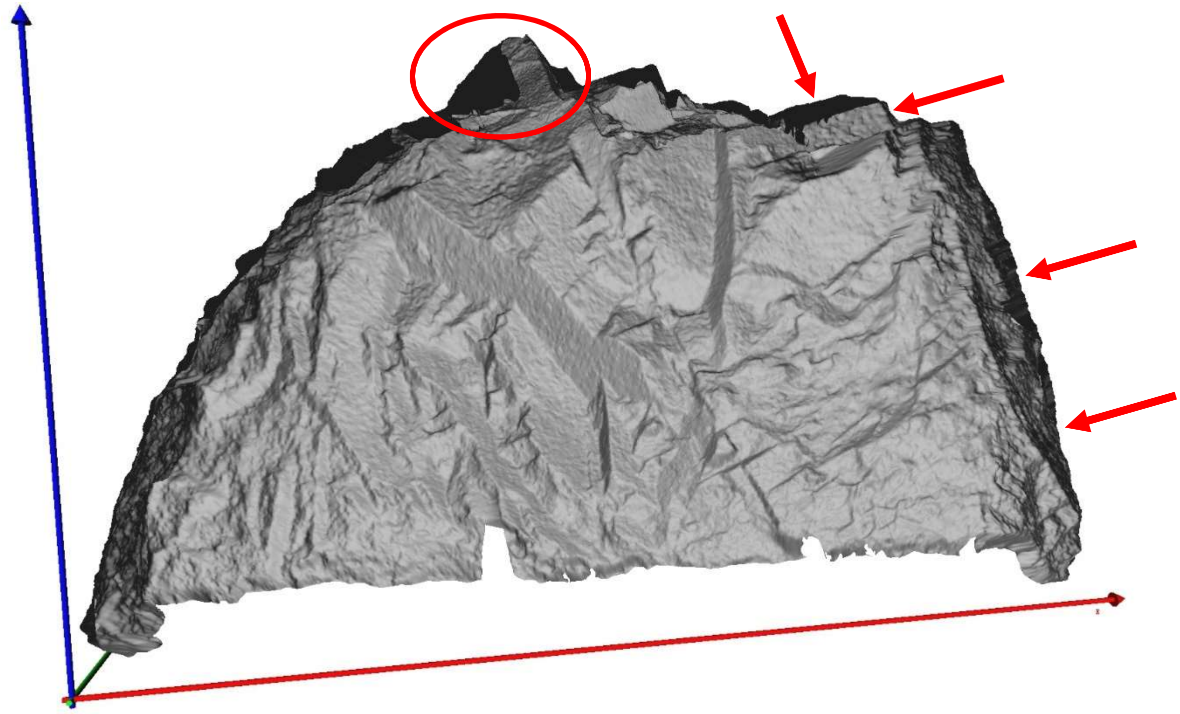

Figure 3.2: Shaded Digital Surface Model of the tunnel face in Case Study I; brighter areas are exposed more direct to the point of view, than darker areas; block detachments can be seen in the roof section (red circle) and the right side wall along with distinct joint planes in the mid-section of the tunnel face (red arrows); the red vector points towards East, the blue is pointing upwards and the green vector indicates the North direction, the height of the tunnel face is approximately 5 m.

3.1.1 Joint Network

The following sub-section presents the results of the applied algorithms and methodologies regarding the mapping of discontinuities in Case Study I.

Joint Trace Detection

In total 576 joint traces were detected based on their pixel- and neighbourhood specifications. The computation time took approximately 10 hours (610 min) and produced after the secondary orientation filtering nine dominant joint trace orientations. The results are displayed in Figure 3.3. A description of the identified joint traces is given in Table 3.4. The orientation values (ψ) are given in a range between -90° and +90°. The values are referenced to a horizontal line, with positive values in a counter-clockwise direction.

Figure 3.3: Resulting joint trace map from the pixel-based joint trace detection in Case Study I; the lines represent 2D joint traces according to changes in shading and colouring of the input image; the single joint traces are coloured according to the different orientation cluster, in total nine different clusters are distinguished.

Table 3.4: Results of the pixel-based joint trace detection for Case Study I; ψ is the mean inclination angle of all enveloping ellipses and a horizontal line, $\bar{L}$ refers to the mean number of pixel belonging to a detected joint trace, $\tilde{L}$ is the median number of pixel belonging to a detected joint trace and L_{max} is the maximum number of pixel belonging to a detected joint trace; the mean and median eccentricity of the enveloping ellipses are given with $\bar{E}$ and $\tilde{E}$.

Cluster ID	ψ [°]	$\bar{L}$ [Px]	$\tilde{L}$ [Px]	L_{max} [Px]	$\bar{E}$ [-]	$\tilde{E}$ [-]	Number of Traces
JTD_1	-61	77.8	48	368	0.9985	0.9988	123
JTD_2	-55	62.4	43	325	0.9977	0.9982	58
JTD_3	-17	86.2	46	359	0.9982	0.9986	47
JTD_4	1	67.9	48	377	0.9982	0.9991	49
JTD_5	20	74.2	48	426	0.9982	0.9989	107
JTD_6	34	74.1	50	233	0.9984	0.9990	48
JTD_7	47	78.2	54.5	183	0.9984	0.9990	24
JTD_8	60	69.5	47.5	247	0.9982	0.9989	102
JTD_9	88	46.6	33.5	146	0.9981	0.9986	18

Joint Plane Detection

829 distinct joint planes were detected in the point cloud of Case Study I. The results are listed in Table 3.5 and displayed in Figure 3.4. In total six dominant joint set orientations were selected.

Table 3.5: Results of the vector-based joint plane detection with DSE for Case Study I; the density refers to the probability density of the single point normal vectors within one principal pole.

Set ID	Dip Direction [°]	Dip Angle [°]	Density [%]	Number of Planes	Color in Figure 3.4
JPD_1	216	61	11.24	177	Blue
JPD_2	067	47	7.57	128	Dark gren
JPD_3	146	81	11.25	145	Bright green
JPD_4	318	27	12.76	101	Yellow
JPD_5	233	26	12.22	102	Orange
JPD_6	338	65	11.35	176	Red

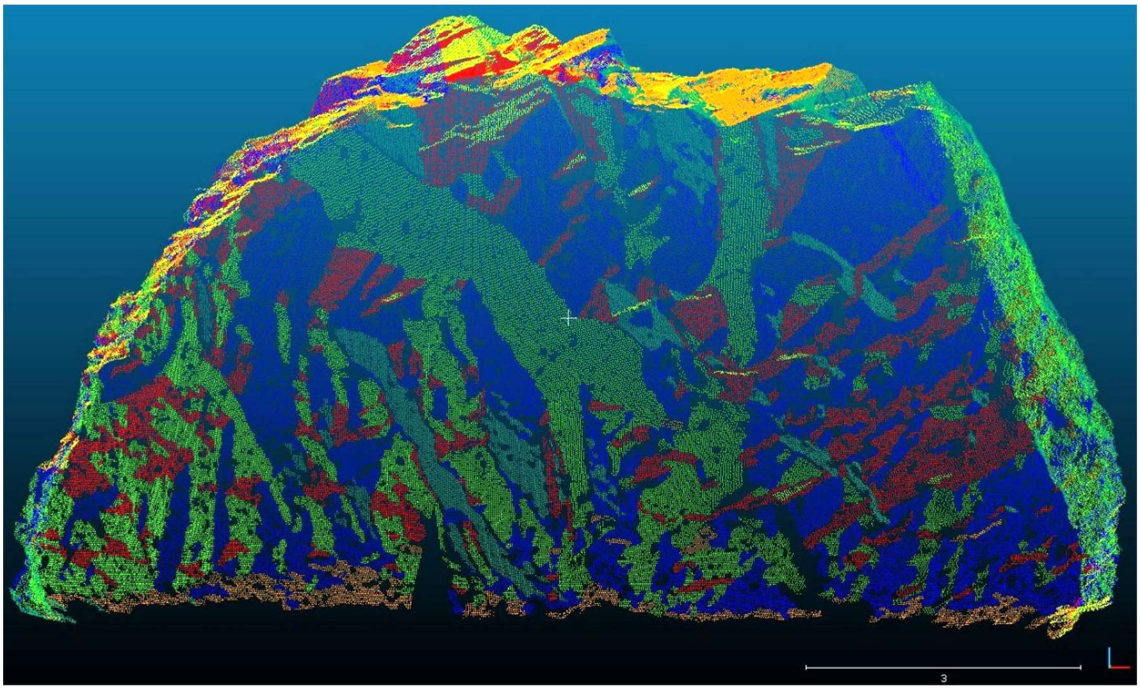

Figure 3.4: Coloured point cloud of Case Study I; the points are coloured in different colours, which represent the different joint sets: JPD_1 is displayed in blue, JPD_2 is coloured in dark green, JPD_3 is coloured in bright green, JPD_4 is displayed in yellow, JPD_5 is coloured in orange and JPD_6 is displayed in red.

Conjunction

The conjunction of both information sources, JTD and JPD, enables the generation of a highly detailed joint structure map. In total 1405 single discontinuities are identified, which can be distinguished into five main joint sets. The number of single joints is the combined number of detected joints from the JTD and JPD. The number of joint sets after the conjunction and its difference to the previous joint sets is discussed in subsection 4.1.2. The specifications of the set orientations are given in Table 3.6. The corresponding stereographic projection (lower hemisphere, equal angle) is shown in Figure 3.5. The joint network can be described according to Table 3.7.

Table 3.6: Results of the conjunction of the joint information from JPD and JTD in Case Study I regarding the joint set orientation prior to the elimination of doublets; SA = spherical aperture, DoC = Degree of Concentration, CoC = Cone of Confidence, NoM = Number of Measurements.

Set ID	Dip Direction [°]	Dip Angle [°]	SA [°]	Concentration	DoO [%]	CoC [°]	NoM	Colour in Figure 3.5
JS1	122	71	24.3	11.75	83.1	2.7	247	Green stars
JS2	343	71	24.3	11.8	83.1	3.0	201	Blue crosses
JS3	243	13	22.1	14.1	85.8	1.8	462	Red triangles (upwards)
JS4	256	79	21.8	14.5	86.2	2.3	277	Yellow circles
JS5	207	85	23.3	12.7	84.3	2.8	218	Orange triangles (downwards)

Table 3.7: Results of the conjunction of the joint information from JPD and JTD in Case Study I regarding the spatial deviation and lateral extent of the single joint sets; P_{10} = linear fracture intensity/frequency, $\bar{X}_S$ = Mean set normal spacing, $\tilde{X}_S$ = Median set normal spacing, $\bar{L}_S$ = Mean set trace length, $\tilde{L}_S$ = Median set trace length, ς = Standard deviation.

Set ID	P_{10} [1/m]	$\bar{X}_S$ [m]	$\tilde{X}_S$ [m]	ς_{Xs} [m]	$\bar{L}_S$ [m]	$\tilde{L}_S$ [m]	ς_{Ls} [m]	$\bar{D}_S$ [m]	$\tilde{D}_S$ [m]	ς_{Ds} [m]
JS1	1.64	0.61	0.30	0.74	0.40	0.24	0.53	0.63	0.48	0.57
JS2	3.12	0.32	0.15	0.44	0.41	0.26	0.46	0.87	0.54	1.08
JS3	2.99	0.33	0.06	0.64	0.39	0.25	0.41	0.70	0.51	0.66
JS4	1.33	0.75	0.21	1.32	0.27	0.20	0.23	0.48	0.35	0.38
JS5	4.70	0.21	0.11	0.27	0.36	0.23	0.40	0.76	0.53	0.83

Figure 3.7 displays the results of the cumulated joint size distribution and the approximation of the curve with the double-exponential function (equation 2.9) exemplarily for JS1. The fittings for the other joint sets look very similar and can be depicted in the Appendix A – Figure 6.1 and Figure 6.2. The variables for each function are given in Table 3.8.

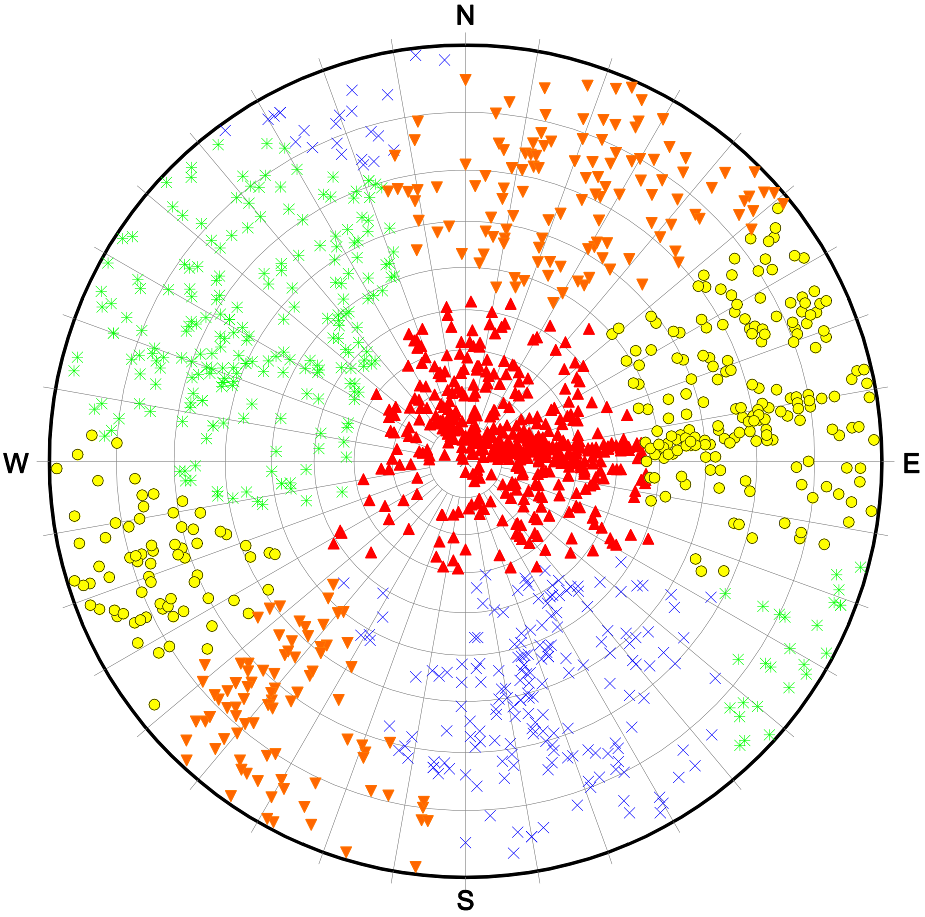

Figure 3.5: Stereographic projection (lower hemisphere, equal angle) of the pole points, clustered according to their set ID (Table 3.6) in Case Study I, JS1 is represented with green stars, JS2 is shown with blue crosses, JS3 is depictured with red triangles (pointing upwards), JS4 is shown with yellow triangles (pointing downwards) and JS5 is given with yellow circles.

Figure 3.6 shows the histogram distribution of the joint spacing measurements from the multiple scanline tool in SMX Analyst at the example of JS1. Since there are only minor differences between the plots of the other joint sets, one can have a look at a complete composition of all histograms in the Appendix A – Figure 6.3 and Figure 6.4.

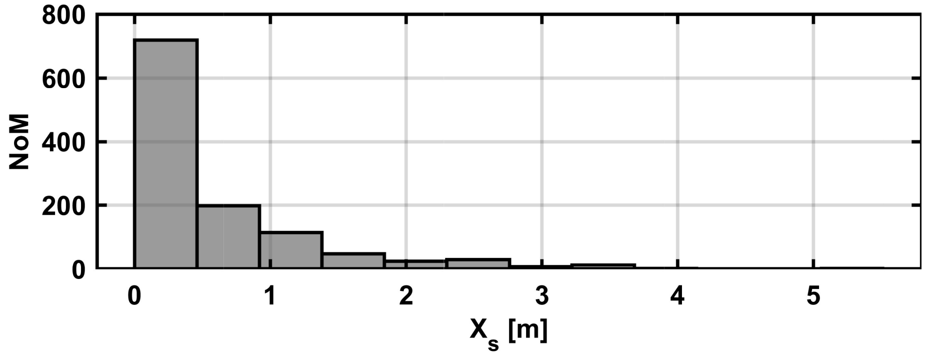

Figure 3.6: Histogram representation of the distribution of the joint set spacing measurements using the multiple scanline tool in SMX Analyst at the example of JS1 of Case Study I.

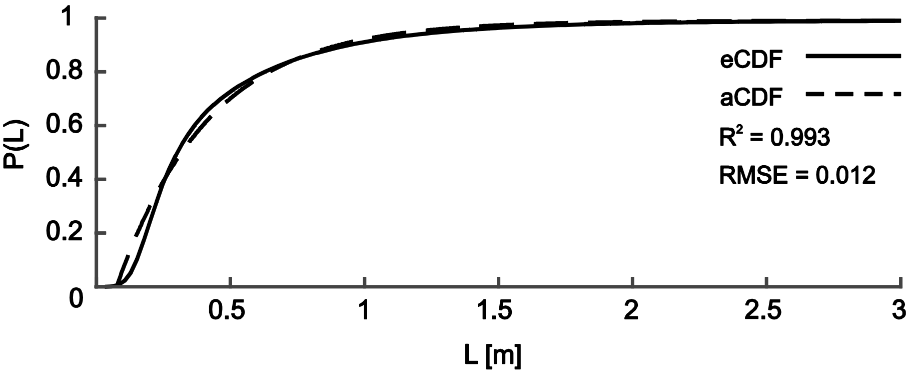

Figure 3.7: Exemplary depiction of the empirical cumulative probability distributions (eCDF) of the two farthermost points in on structure as a reference for the joint size distribution (solid lines) for JS1 in Case Study I; the cumulative density distributions are approximated with the double-exponential function (aCDF) according to eq. 2.9 (dashed lines); each subplot includes the coefficient of determination (R^2) as well as the root mean squared error (RMSE).

Table 3.8: Variables *a* to *d* of the fitted double-exponential function, to describe the analytical cumulative probability distribution (aCDF) of the joint sizes per set as well as the coefficient of determination (R^2) and the root mean square error (RMSE) of the functions in Case Study I.

Set ID	*a*	*b*	*c*	*d*	R^2	RMSE
JS1	0,9851	0,0016	-1,2298	-2,9223	0.993	0.012
JS2	0,9812	0,0020	-1,1910	-2,3759	0.994	0.011
JS3	0,9789	0,0036	-1,22149	-2,8583	0.996	0.011
JS4	0,9792	0,0065	-1,4019	-4,1456	0.993	0.016
JS5	0,9592	0,0069	-1,2656	-3,1100	0.993	0.014

In Figure 3.8, the joint trace measurements from SMX Analyst (filled bars) and the statistically derived joint size distributions (unfilled bars) for each joint set according to sub-section 2.1.4 are displayed. The data is within a range of 0 and 1.5 m. Since the histograms of the other joint trace length distributions look very similar, a complete depiction of all data is given in the Appendix A – Figure 6.5 and Figure 6.6. The statistical values for the mean and median set joint size, representing the diameter of a disc in the DFN, as well as the corresponding standard deviation are given in Table 3.7. The differences between the measured joint traces (L_{SMX}) and the statistically increased joint traces of the DFN (L_{DFN}) are discussed in sub-section 4.1.1.

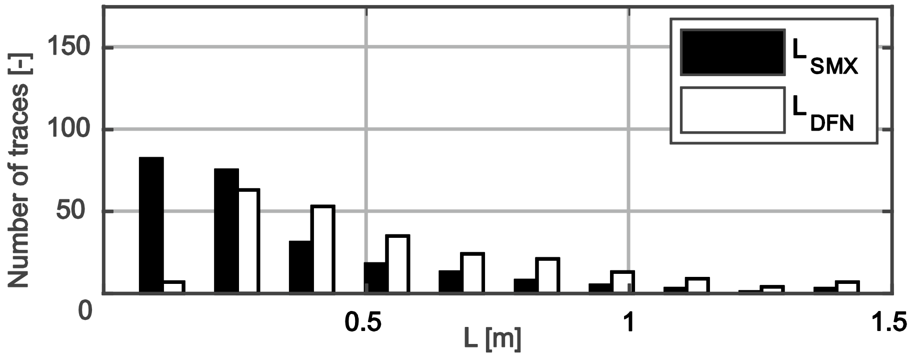

Figure 3.8: Exemplary histogram representation of the joint trace lengths (L_{SMX}/L_{DNF}) between 0 and 1.5 m for JS1 in Case Study I; the bars represent the joint trace lengths obtained from SMX Analyst, the lines represent the results obtained by the statistical recalculation of the joint size distribution for the DFN.

3.1.2 Rock Mass Geometry

In Case Study I the joints are medium spaced (20 to 60 cm); the volumetric joint count can be classified as high with $\overline{J_V} = 11.8$ 1/m and $\widetilde{J_V} = 23.4$ 1/m (ÖNORM EN ISO 14689).

Block size, shape and orientation distributions are displayed in Figure 3.9-a to c, using the illustrative devices introduced in sub-section 1.3.2. The quantile-values of the block sizes are listed in Table 3.9. The block shapes are dominated by platy and cubic as well as cubit to platy shaped blocks. β predominantly ranges between 1 and 2, whereas α has a peak distribution between 1 and 1.1 as well as 9.8 and 10. A dominant orientation of the longest block vertices cannot be identified clearly, however several trend and plunge cluster exist: 188/00, 067/01, 261/29, 336/90 and 079/33 (peaks are revealed at density deviations higher than 0.6). The block size is classified according to (ÖNORM EN ISO 14689) as small (using $\widetilde{V_B}$) to medium (using $\overline{V_B}$) sized.

Table 3.9: IBSD of the DFN in Case Study I, $V_{B,25}$ and $V_{B,75}$ represent the 25 %- and 75 %-quantile, $\widetilde{V_B}$ refers to the median and $\overline{V_B}$ to the mean block size, the minimum block size is given with $V_{B,min}$, whereas $V_{B,max}$ is giving the maximum block size.

	$V_{B,25}$	$\widetilde{V_B}$	$V_{B,75}$	$\overline{V_B}$	s_{VB}	$V_{B,min}$	$V_{B,max}$
Volume [m³]	0.004	0.014	0.06	0.124	0.467	0.0002	11.206

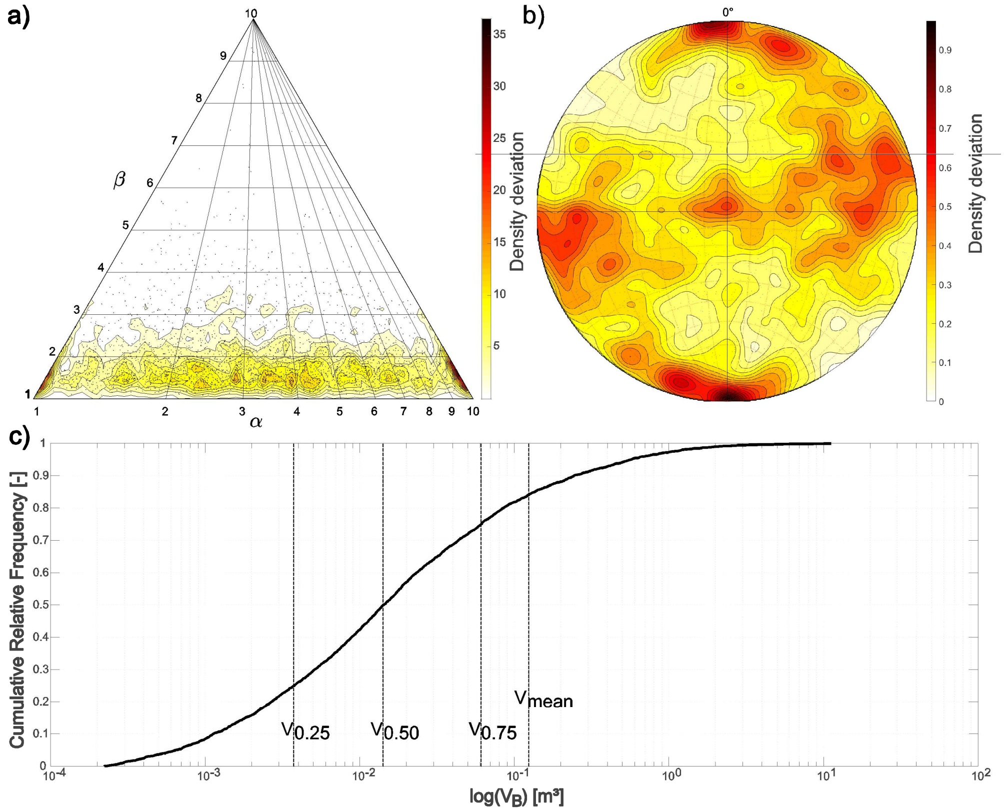

Figure 3.9: Geometric characterization of the joint network in the DFN of Case Study I; a) resembles the block shape distribution in contour patches, b) displays the distribution of the block orientations in trend and plunge values referring to the vector orientation of the longest block inter-vertex chord and c) shows the cumulative block size distribution (bold line) along with the mean, median and quantile values for the block volumes, as given in Table 3.9.

3.1.3 Block Stability Analysis

In the following sub-section, the results of the block stability analysis and sensitivity analyses are presented for Case Study I.

In order to identify the sensitivity of the used friction angles Table 3.10 shows the total volumes of blocks, moving more than 1 cm in each excavation step. The values are also plotted in Figure 3.10. The calculations were performed, considering a j_{kn} of $1 \cdot 10^{11}$ Pa/m and a j_{ks} of $1 \cdot 10^{10}$ Pa/m. The tunnel is excavated considering an overburden of 20 m at a K of 0.33. In the first excavation sequence the tunnel is excavated 4.4 m ahead of the SOI, in the second sequence (SSS-2) another 2.2 m are excavated. The remaining 2.2 m to reach the SOI are excavated in the third excavation step (SSS-3). In the last sequence (SSS-4), the next round length after the SOI is excavated (Figure 2.6).

Table 3.10: Total volume of blocks, moving more than 1 cm in each excavation sequence in Case Study I for a K equal to 0.33 and decreasing friction angles.

K	Excavation Sequence	$\Sigma V_{B,0.01}$ [m³] φ + 5°	 φ	 φ - 5°
0.33	SSS-1	0,028	0,028	0,028
	SSS-2	0,035	0,035	0,035
	SSS-3	4,399	4,790	4,943
	SSS-4	11,783	17,104	18,158

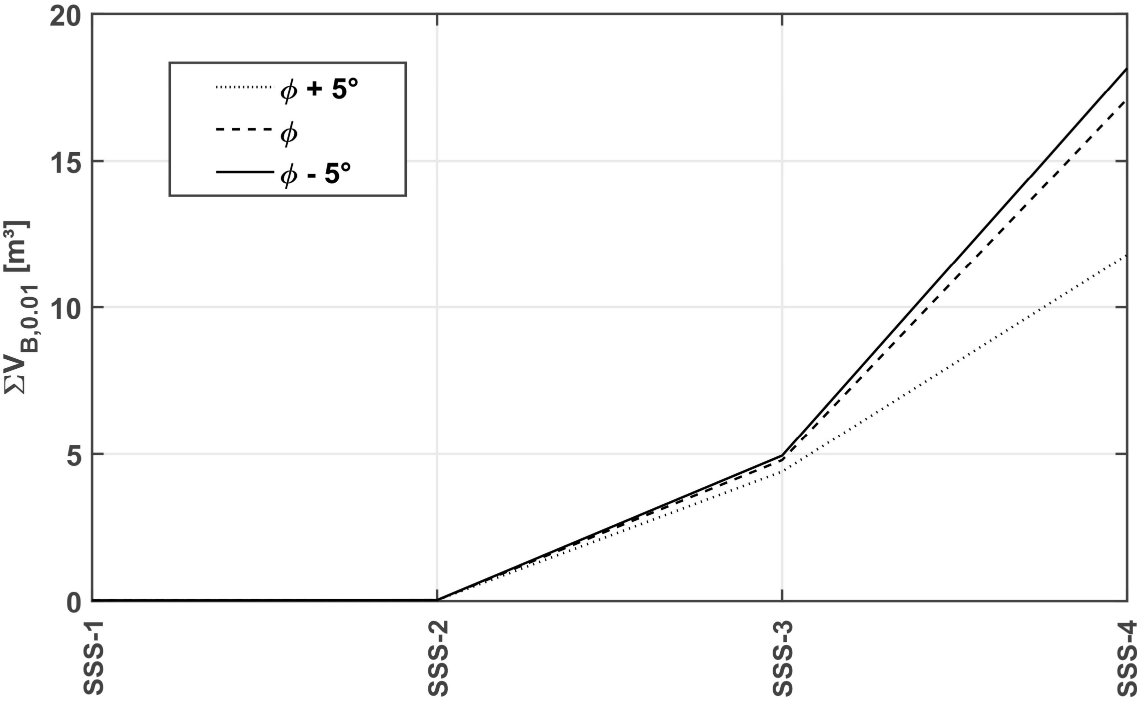

Figure 3.10: Changing $\Sigma V_{B,0.01}$ in each excavation sequence (SSS-1 to SSS-4) depending on the applied joint friction angle: the dotted line represents the case of φ + 5°, the dashed line represents the case of φ and the solid line plots the values of φ - 5°.

Table 3.10 and Figure 3.10 show an increase of the total block volume with a decreasing friction angle (φ) after reaching the SOI (SSS-3 and SSS-4). The difference between $\Sigma V_{B,0.01}(\varphi)$ and $\Sigma V_{B,0.01}(\varphi + 5°)$ in SSS-3 is 0.391 m³ and in SSS-4 5.321 m³. The difference between $\Sigma V_{B,0.01}(\varphi - 5°)$ and $\Sigma V_{B,0.01}(\varphi)$ in SSS-3 is 0.1.53 m³ and in SSS-4 is 1.054 m³.

In order to check the modelled with the actual excavation profile the excavation profiles after calculating SSS-3 and SSS-4 as well as changing joint friction angles are compared with the DSM of the SOI. The results are shown in Figure 3.11-a and b (φ + 5°) Figure 3.11-c and d (φ) and Figure 3.11-e and f for φ - 5°. Blocks moving more than 1 cm have been deleted from the model to show the overbreak. The DSM is displayed in brown, whereas the rock mass is displayed in transparent white. In regions, where the DSM superimposes the modelled rock mass (brown is clearly visible), DCF occurred, unless the rock mass behind has not been excavated. Vice versa, in regions where the transparent white rock mass superimposes the DSM, not blocks have been excavates or have detached. It can be seen that minor block detachments occur in the tunnel face (Figure 3.11-a, c and e) and minor to major DCF occurred in the left crown section. No overbreak can be observed in the right crown section.

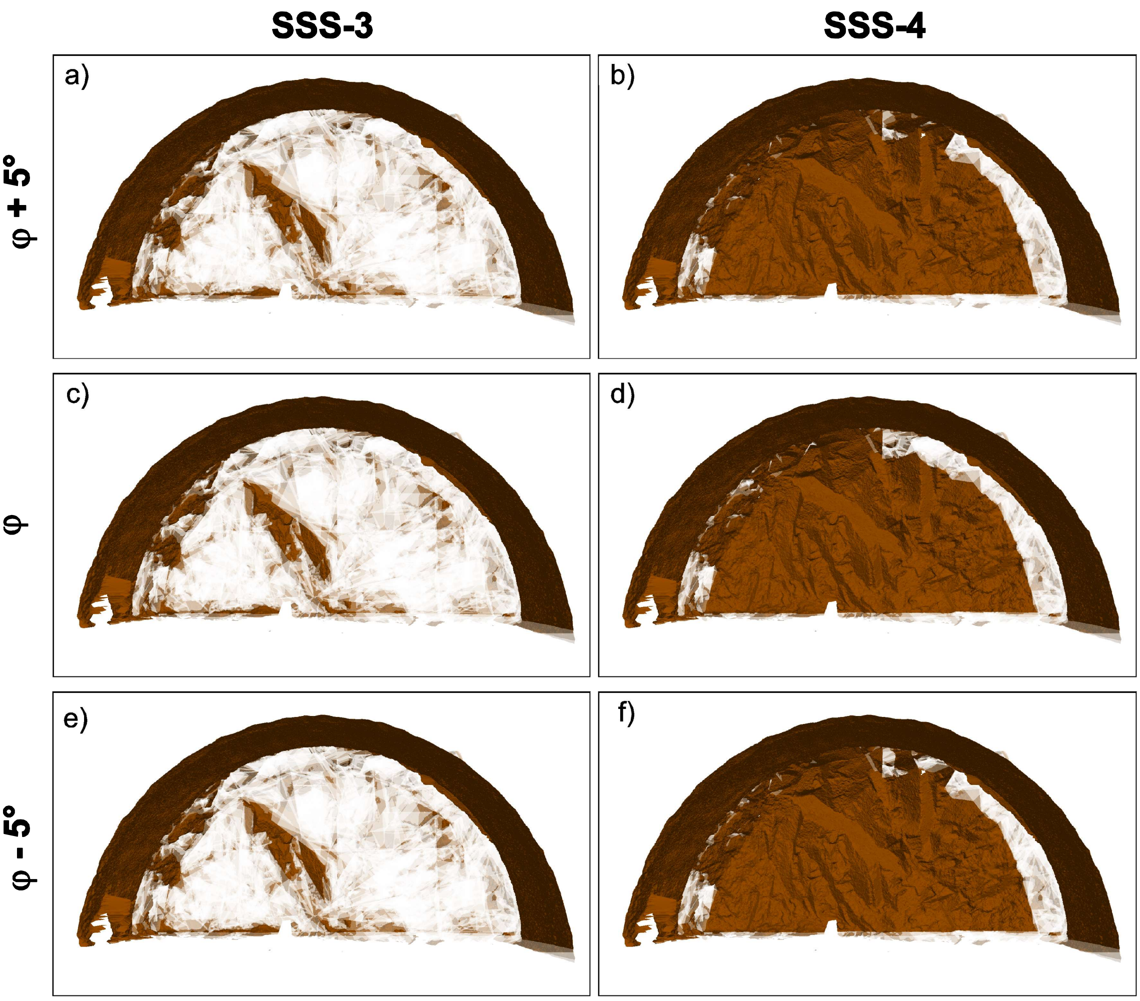

Figure 3.11: Comparison of the modelled and the actual excavation profile for the excavation sequences 3 and 4 in Case Study I in the case of φ + 5° (a and b), φ (c and d) and φ – 5° (e and f); the rock mass is displayed in transparent white, whereas the DSM is displayed in brown; blocks moving more than 1 cm are excluded from the figure, to indicate DCF; in general, if the DSM superimposes the rock mass, DCF occurred, unless the rock mass has not been excavated.

3.2 Case Study II – Foliated Rock Mass

Assessing the joint network geometry in Case Study II is more sophisticated than in Case Study I. Here the rock mass consists of a foliated gneiss, which controls the excavation profile especially in the crown section, although no dominant joint planes are present. The foliation appears both as sub-horizontal and folded and is represented by frequently changing bright and dark layers. Furthermore, the joint network expresses a very dense fracturing, and to ensure a representative sample size a large number of measurements is necessary. To ensure a sufficient number of measurements the application of automated mapping tools is favoured. However, due to the lack of distinct joint planes e.g. of the foliation, some joints set might be underrepresented and an additional source of information is necessary for a comprehensive assessment of the joint network geometry. This additional data shall be collected by the novel approach for a pixel-based JTD.

For the investigations, data were kindly provided by the company ASFINAG BAU MANAGEMENT GMBH – Bmstr. Ing. Herwig Moser – and the company Geoconsult ZT GmbH – Mag.rer.nat Dr.rer.nat. Gerald Pischinger. The data consists of various digital images of the tunnel faces, scaled and oriented SMX models, the geological-geotechnical documentation (Geoconsult ZT GmbH, 2015) and the report about the conducted laboratory program (MAPAG Materialprüfung G.m.b.H, 2015). From this data, the exemplary tunnel station 2240.6 was selected. The tunnel face specifications are given in Table 3.11.

Table 3.11: Specifications of Case Study II according to Geoconsult ZT GmbH (2015).

Section	Unit	Value
Oberburden	[m]	338.9
Round length	[m]	2.2
Orientation of the tunnel face	[°]	150/90
Lithology		
Amphybolite	[%]	5,78
Granitgneiss	[%]	80.02
Fault material	[%]	10.2
Rock Mass Types		
GT1	[%]	90
GT2	[%]	10
Documented joint sets		sf, st, k (H)*
Comments		narrow spaced foliation controls tunnel profile in roof section, two minor fault zones (middle/ left side wall) several discontinuity-controlled block failures in the left side wall and the tunnel face, partly with slickensides (H)

*sf = Foliation, st = Fault, k (H) = Joint (with slickensides)

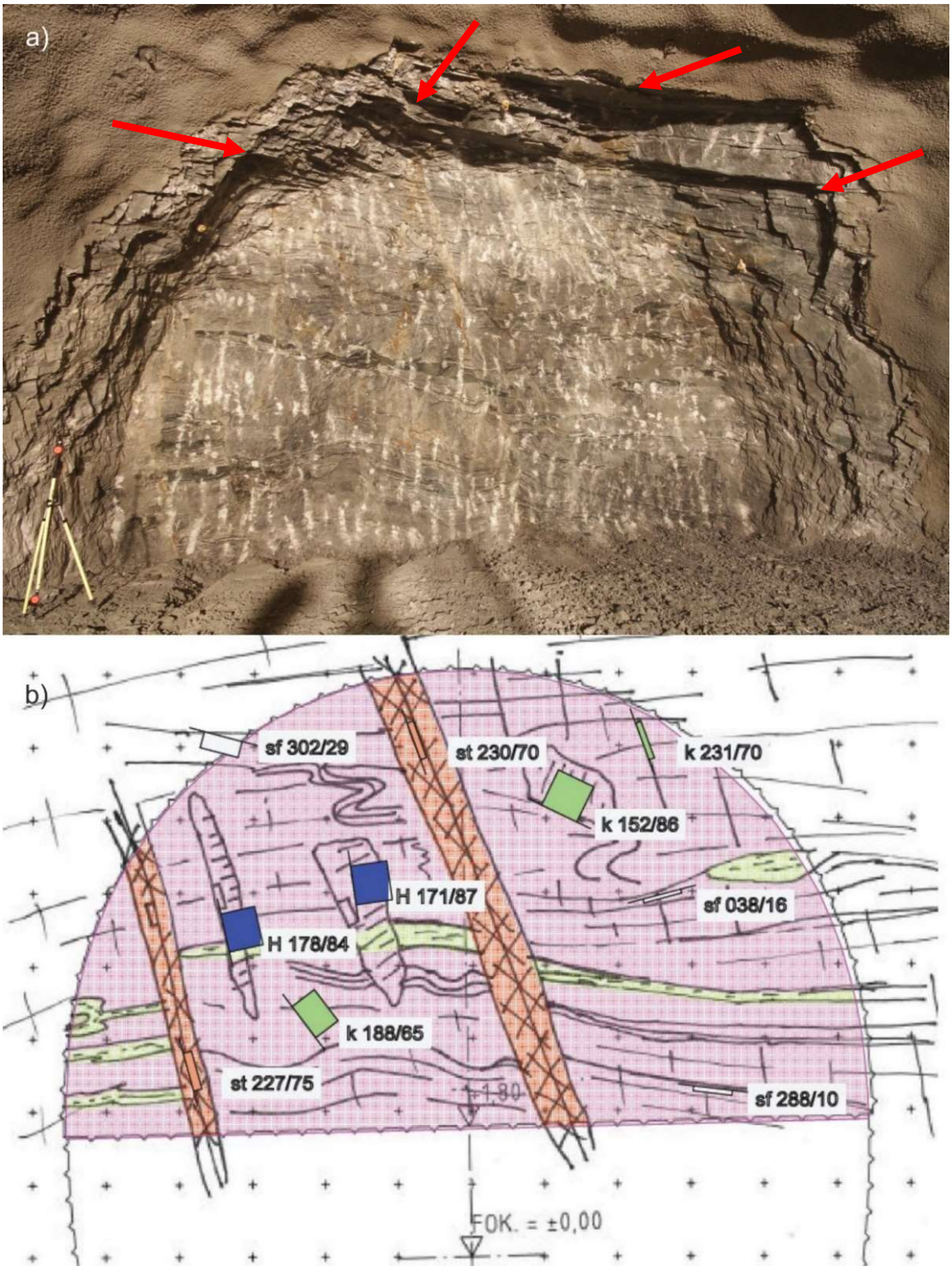

Figure 3.12: Tunnel face in Case Study II (a); block detachments control the tunnel shape in the roof section (red arrows); white traces in the tunnel face are scratch marks from the excavator; the foliation can be anticipated by an alteration in the mafic and leucocratic units; a slight offset in these layers indicates a fault zone; the range pole at the left side is 1.35 m long; b) Geological documentation of the tunnel face displaying changes in the lithology (purple vs. green colour vs. orange), as well as measurements for the foliation and other joints; in the middle and left tunnel face, two faults are mapped.

According to Geoconsult ZT GmbH (2015) the investigated tunnel section consists to the most parts of Granitgneiss with minor layers of Amphibolite and fault material. The strength for the Granitgneiss is given with a range of 50 to 100 MPa. The strength of the fault material is given with 5 to 25 MPa. The rock mass is mostly unweathered, but with minor areas of moderate weathering. No water inflow was documented. The GSI is given with 25 to 40.

Figure 3.12-a shows a good correspondence with the geological sketch (Figure 3.12-b), however the number of measurements for describing the joint network geometry is quite low and only the most dominant features are mapped. Also, changes in the foliation due to folding are sketched but not measured, and the thickness of the fault zones are only given by the sketch rather than by the photograph. Since the foliation obviously is a major factor for controlling the excavation profile, it is necessary to quantify the corresponding geometrical characteristics as good as possible.

According to the project documents (MAPAG Materialprüfung G.m.b.H, 2015, Geoconsult ZT GmbH, 2015), no information is provided about the rock properties (e.g. Young's modulus, base friction angle, and cohesion) in the selected section. The density was assumed with 2600 kg/m³. Since the numerical representation of the rock mass considers only rigid bodies, properties for the block deformation and shear resistance, like the Young's modulus, the Poisson ratio, the base friction angle and the cohesion were not deemed relevant. The joint set specifications are given in Table 3.12. The values for the joint shear resistance were selected according to engineering judgement and the verbal description in (Hoek et al., 1997, Geoconsult ZT GmbH, 2015).

Table 3.12: Joint set specifications in Case Study II according to the documentation (Geoconsult ZT GmbH, 2015) and engineering judgement (e.g. Hoek et al., 1997); values in the brackets indicate the friction angles for the sensitivity analyses; literature values are marked with "*".

Parameter				Joint type	
		Unit	Foliation (sf)	Joint (k/H)	Fault (st)
Orientation	DD/D	[°]	288/16	172/81	229/73
Spacing	X	[m]	0.06-0.2	0.2-0.6 (0.6-2)	>2
Surface description	-	[-]	Planar, smooth	Planar, rough	Planar, polished
Trace length	L	[m]	1-2	2-3	> 5
Friction angle*	φ	[°]	32 ± 5	38 ± 5	22 ± 5
Residual friction angle*	φ_{res}	[°]	30 ± 5	33 ± 5	20 ± 5
Dilation*	ι	[°]	2	10	0
Cohesion*	c	[Pa]	0	0	$5 \cdot 10^5$
Residual cohesion*	c_{res}	[Pa]	0	0	$2.5 \cdot 10^5$
Maximum dilation distance*	z_{dil}	[m]	0.005	0.005	0.005

The tunnel faces were documented and photographed in 2014 with a calibrated DSL Canon EOS 7D with a focal length of 10 mm, mounted on a tripod. The image resolution is 5184 x 3456 Pixel. The distance between the camera position and the tunnel face was 7.8 m. The average geometric image resolution can be approximated with 10 mm²/pixel. The specifications of the 3D point clouds are given in Table 3.13.. The shaded DSM is displayed in Figure 3.13.

Table 3.13: Statistical 3D point cloud specifications of in Case Study II.

Parameter	Unit	Value
Number of 3D points	[-]	1,995,875
Minimal area patch size for orientation measurements	[m²]	0.001
Surface area	[m²]	168
Average 3D point spacing	[m]	0.01

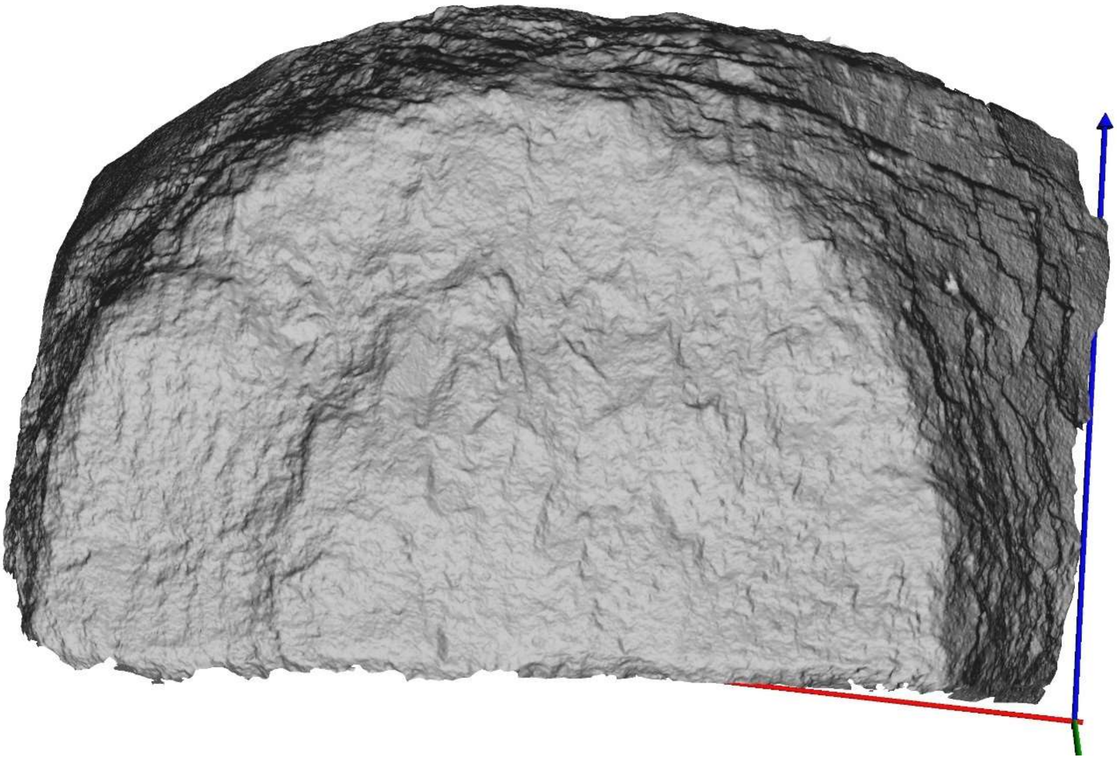

Figure 3.13: Shaded digital surface model of the tunnel face in Case Study II, the brightness is an indicator for the exposure towards the inspector, hence darker areas are more parallel to the line of sight than brighter areas, which eases the identification of joint planes; the red vector points towards, East, the green towards North and the blue is parallel to the z-axis; the height of the tunnel face is approximately 6 m.

3.2.1 Joint Network

In the following paragraphs, the mapping results of the joint network in Case Study II are presented.

Joint Trace Detection

In total 1264 joint traces were detected based on their pixel- and neighbourhood specifications. The computation time took almost two days (2877 min). The 2D results are displayed in Figure 3.14. The traces are classified into four dominant orientation clusters: JTD_1 (-56°) displayed in red, JTD_2 (-31°) is displayed in green, JTD_3 (-1°) is displayed in blue and JTD4 (71°) is coloured in cyan. Table 3.14 provides detailed information about the identified joint traces.

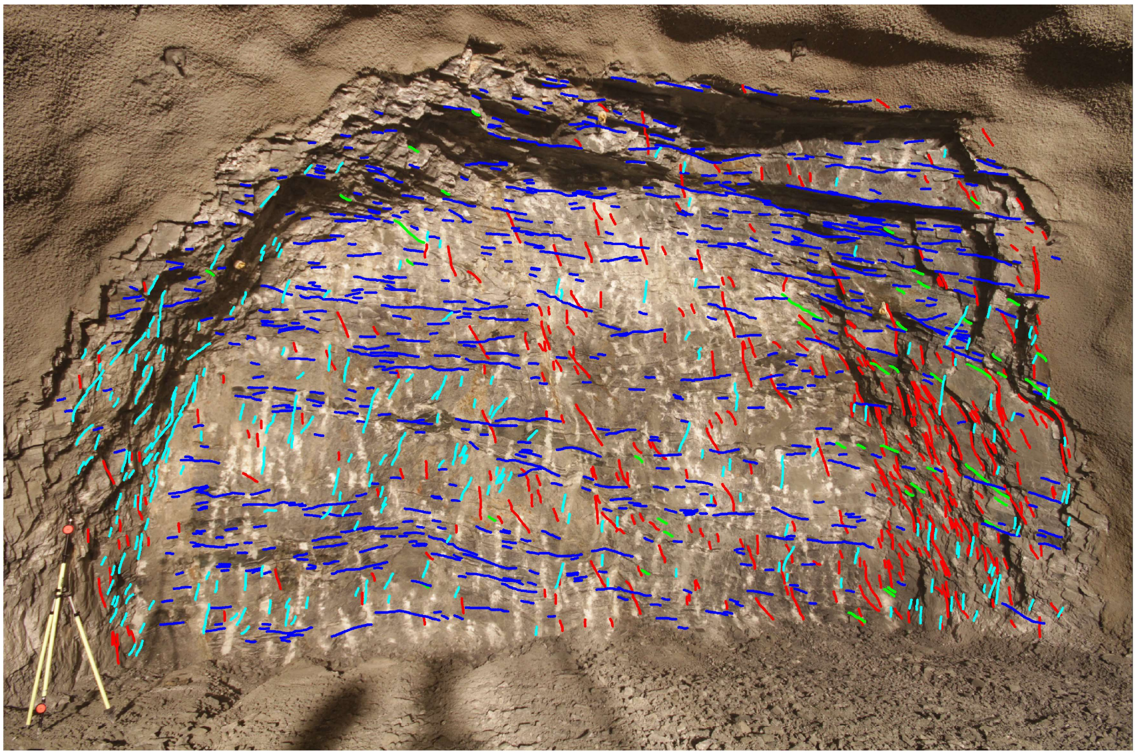

Figure 3.14: Resulting joint traces of the pixel based JTD in Case Study II; each coloured line represents a detected joint trace, following a morphological edge or line; each line is assigned to an orientation cluster according to the four dominant orientations and are coloured in red (JTD_1, -56°), green (JTD_2, -31°), dark blue (JTD_3, -1°) and cyan (JTD_4, 71°).

Table 3.14: Results of the pixel-based joint trace detection for Case Study II; ψ is the angle between the enveloping ellipses and a horizontal line, $\bar{L}$ refers to the mean trace length, respectively the number of pixel assigned to the structure, $\tilde{L}$ is the median trace length and L_{max} is the maximum trace length per cluster in pixel; the mean and median eccentricity of the ellipses are given with $\bar{E}$ and $\tilde{E}$.

Cluster ID	ψ [°]	$\bar{L}$ [Px]	$\tilde{L}$ [Px]	L_{max} [Px]	$\bar{E}$ [-]	$\tilde{E}$ [-]	Number of Traces
JTD$_1$	-56	67	46.5	380	0.9981	0.9985	358
JTD$_2$	-31	57.5	42	199	0.9979	0.9987	43
JTD$_3$	-1	81.3	50	430	0.9985	0.9990	621
JTD$_4$	71	60.5	45.5	256	0.9982	0.9988	242

Joint Plane Detection

The joint plane detection delivered 1295 planes in Case Study II. The results are listed in Table 3.15 and displayed in Figure 3.15.

Table 3.15: Results of the vector-based joint plane detection with DSE for Case Study II.

Set ID	Dip Direction [°]	Dip Angle [°]	Density [%]	Number of Planes	Color in Figure 3.15
JPD$_1$	148	81	47.83	228	Blue
JPD$_2$	216	60	24.69	393	Green
JPD$_3$	321	26	6.39	373	Yellow
JPD$_4$	067	37	12.93	301	Red

Joint planes are detected predominantly in the left and right side-wall as well as in the roof section (subordinated). The actual tunnel face is considered more or less as one single discontinuity and only very few other joint planes are identified here.

Conjunction

The conjunction of the two structure maps (JPD/JTD), followed by a re-clustering of the measurements, resulted in the definition of five distinct structure sets with 2468 single measurements. During the conjunction, 91 doublets were deleted. The specifications of the distinguished joint sets are given in Table 3.16. The stereographic projection of the pole points is displayed in Figure 3.16.

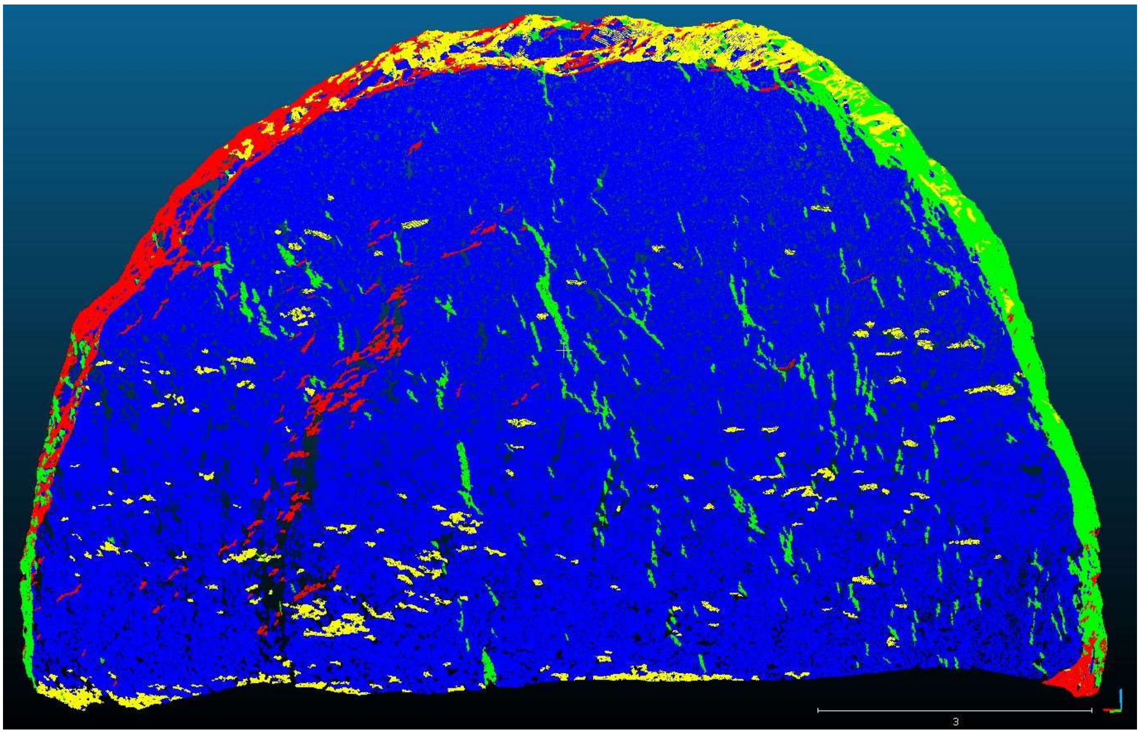

Figure 3.15: Results of the vector-based joint plane detection at Case Study II; each displayed point is coloured according to its allocated joint set, and enables the localisation of distinct joint planes; JPD$_1$ is coloured in blue, JPD$_2$ is displayed in bright green, JPD$_3$ is displayed in yellow and JPD$_4$ is coloured in red.

Table 3.16: Results of the conjunction of the joint information from JPD and JTD in Case Study II regarding the joint set orientation, prior to the elimination of doublets; SA = spherical aperture, DoC = Degree of Concentration, CoC = Cone of Confidence, NoM = Number of Measurements.

Set ID	Dip Direction [°]	Dip Angle [°]	SA [°]	Concentration	DoO [%]	CoC [°]	NoM	Colour in Figure 3.16
JS1	196	72	23.5	12.6	84.2	1.9	489	Green diamonds
JS2	325	5	18.5	19.9	90.0	1.2	703	Blue crosses
JS3	059	77	21.8	14.5	86.2	1.8	467	Red triangles (upwards)
JS4	320	40	18.1	20.6	90.3	1.4	493	Yellow squares
JS5	114	85	27.8	9.2	78.3	2.6	361	Orange triangles (downwards)

Table 3.17: Results of the conjunction of the joint information from JPD and JTD in Case Study II regarding the spatial deviation and lateral extent of the single joint sets; P_{10} = linear fracture intensity /frequency, $\bar{X}_s$ = Mean set normal spacing, $\tilde{X}_s$ = Median set normal spacing, $\bar{L}_s$ = Mean set trace length, $\tilde{L}_s$ = Median set trace length, $\bar{D}_s$ = Mean set fracture size (diameter), $\tilde{D}_s$ = Median set fracture size, ς = Standard deviation.

Set ID	P_{10} [1/m]	$\bar{X}_s$ [m]	$\tilde{X}_s$ [m]	ς_{Xs} [m]	$\bar{L}_s$ [m]	$\tilde{L}_s$ [m]	ς_{Ls} [m]	$\bar{D}_s$ [m]	$\tilde{D}_s$ [m]	ς_{Ds} [m]
JS1	1.53	0.65	0.39	0.82	0.20	0.13	0.36	0.30	0.23	0.38
JS2	2.57	0.39	0.09	0.70	0.22	0.14	0.30	0.39	0.27	0.46
JS3	1.03	0.97	0.14	1.92	0.19	0.12	0.35	0.39	0.23	0.81
JS4	1.40	0.71	0.41	0.86	0.20	0.13	0.21	0.36	0.25	0.34
JS5	1.28	0.78	0.42	0.95	0.20	0.13	0.49	0.34	0.25	0.63

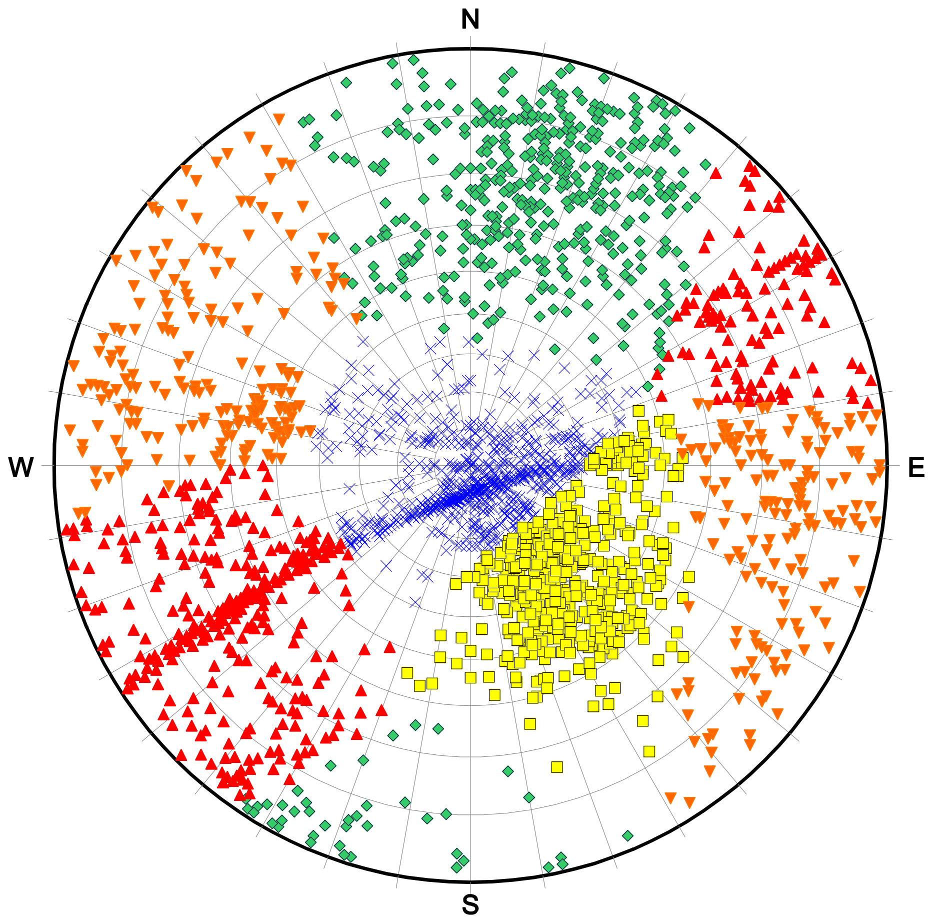

Figure 3.16: Results of the conjoined discontinuity identification at Case Study II (stereographic projection, lower hemisphere); JS1 is coloured in green diamonds, JS2 is displayed in blue crosses, JS3 is displayed in red triangles (pointing upwards), JS4 is coloured in yellow squares and JS5 is coloured in orange triangles (pointing downwards).

Figure 3.17 displays the results of the cumulated joint size distribution and the approximation of the curve with the double-exponential function (equation 2.9) for JS1. The fittings for the other joint sets look very similar and can be depicted in the Appendix B – Figure 6.7 and Figure 6.8. Table 3.18 specifies the parameters *a* to *d* for the double-exponential function of the analytical approximation of the measured trace lengths. The parameters are given along with the goodness of fitting (coefficient of determination – R^2 and the root mean square error – RMSE).

Table 3.18: Variables *a* to *d* of the fitted double-exponential function to describe the analytical cumulative probability distribution of the joint sizes per set as well as the coefficient of determination (R^2) and the root mean square error (RMSE) of the functions in Case Study II.

Set ID	*a*	*b*	*c*	*d*	R^2	RMSE
JS1	0.9956	0.0004	-1.2656	-6.1140	0.989	0.009
JS2	0.9844	0.0025	-1.2002	-5.1426	0.992	0.011
JS3	0.9926	0.0007	-1.2285	-6.0467	0.989	0.010
JS4	0.9682	0.0119	-1.2322	-5.7704	0.990	0.018
JS5	0.9973	0.0001	-1.1763	-5.3942	0.984	0.010

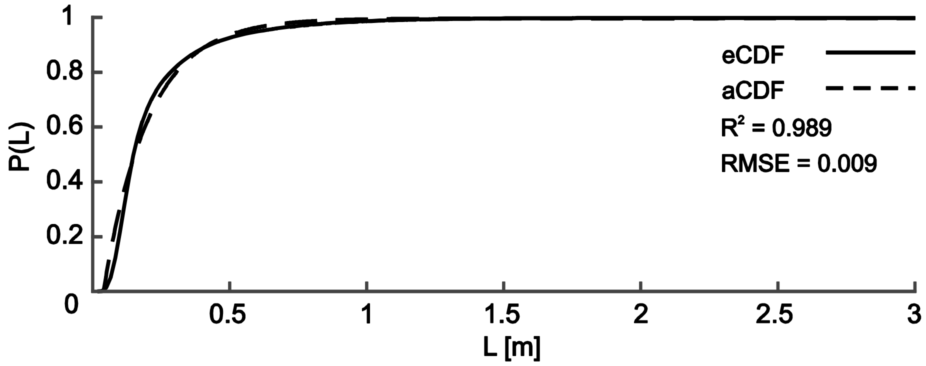

Figure 3.17: Empirical cumulative probability distributions (eCDF) of the two farthermost points in on structure as a reference for the joint size distribution (solid lines) at the example of JS1 in Case Study II; the cumulative density distributions are approximated with the double-exponential function (aCDF) according to eq. 2.9 (dashed lines).

Figure 3.18 represents a histogram plot of the spacing measurements at the example of JS1 using the multiple scanline tool in SMX Analyst. Since there are only minor differences between the plot of JS1 to JS5, a complete composition can be found in the Appendix B – Figure 6.9 and Figure 6.10.

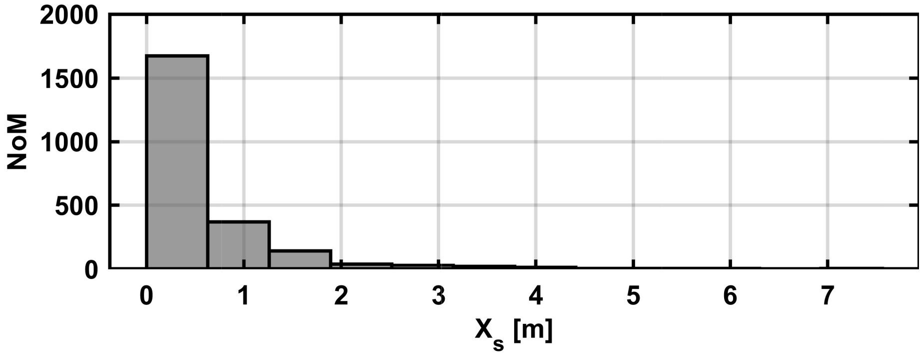

Figure 3.18: Histogram representation of the distribution of the joint set spacing measurements using the multiple scanline tool in SMX Analyst at the example of JS1 of Case Study II.

Figure 3.19 shows the exemplary joint trace length and size distributions (diameter) for JS1 between 0 and 1.5 m. The figure includes both the trace length distribution, obtained from SMX Analyst (L_{SMX}, filled black bars), and the joint size distribution used for the generation of the DFN (L_{DFN}, unfilled bars). Since the histograms of the other joint trace length distributions look very similar, a complete depiction of all data is given in the Appendix B – Figure 6.11 and Figure 6.12. The statistical values for the mean and median set joint size, representing the diameter of a disc in the DFN, as well as the corresponding standard deviation are given in Table 3.17.

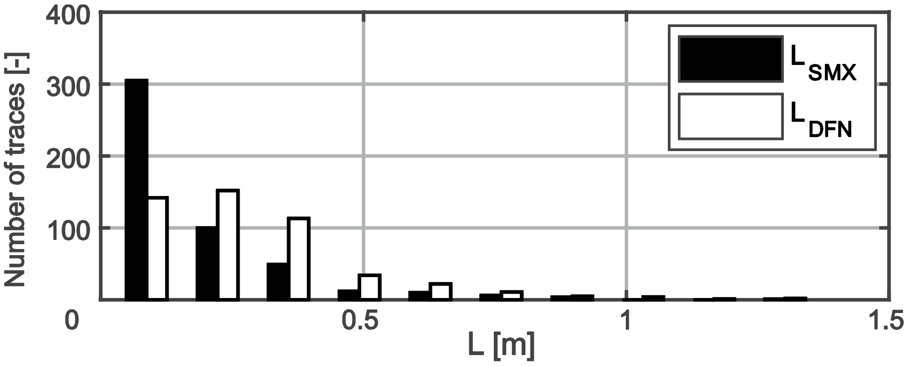

Figure 3.19: Exemplary histogram representation of the joint trace lengths (L_{SMX}/L_{DNF}) between 0 and 1.5 m for JS1 in Case Study II; the bars represent the joint trace lengths obtained from SMX Analyst, the lines represent the results obtained by the statistical recalculation of the joint size distribution for the DFN.

The differences between the measured joint traces (L_{SMX}) and the statistically increased joint traces of the DFN (L_{DFN}) are discussed in sub-section 4.1.1.

3.2.2 Rock Mass Geometry

In Case Study II the rock mass geometry can be described according to (ÖNORM EN ISO 14689) as a rock mass with closely spaced discontinuities (60 to 200 mm). The mean volumetric joint count ($\bar{J}_v$) is given with 6.5 1/m and 12.9 1/m for the median volumetric joint count ($\tilde{J}_V$). Hence, the volumetric joint count can be classified as moderately high to high.

The block size, shape and orientation distributions are displayed in Figure 3.20-a to c using the visualization tools described in sub-section 1.3.2. The quantile-values of the block sizes are listed in Table 3.19. The block shapes are dominated by platy shaped blocks (α higher than 9.5) with a tendency towards the intermediate class cubic to platy. β usually ranges between 1 and 3. Apparently, the dominant block orientation is 339/02 (density deviation higher than 1). Subordinated, two other peak orientations exist with 272/27 and 093/29 with densities higher than 0.9. The block size is classified according to (ÖNORM EN ISO 14689) as small ($\widetilde{V_B}$) to medium ($\overline{V_B}$) sized blocks.

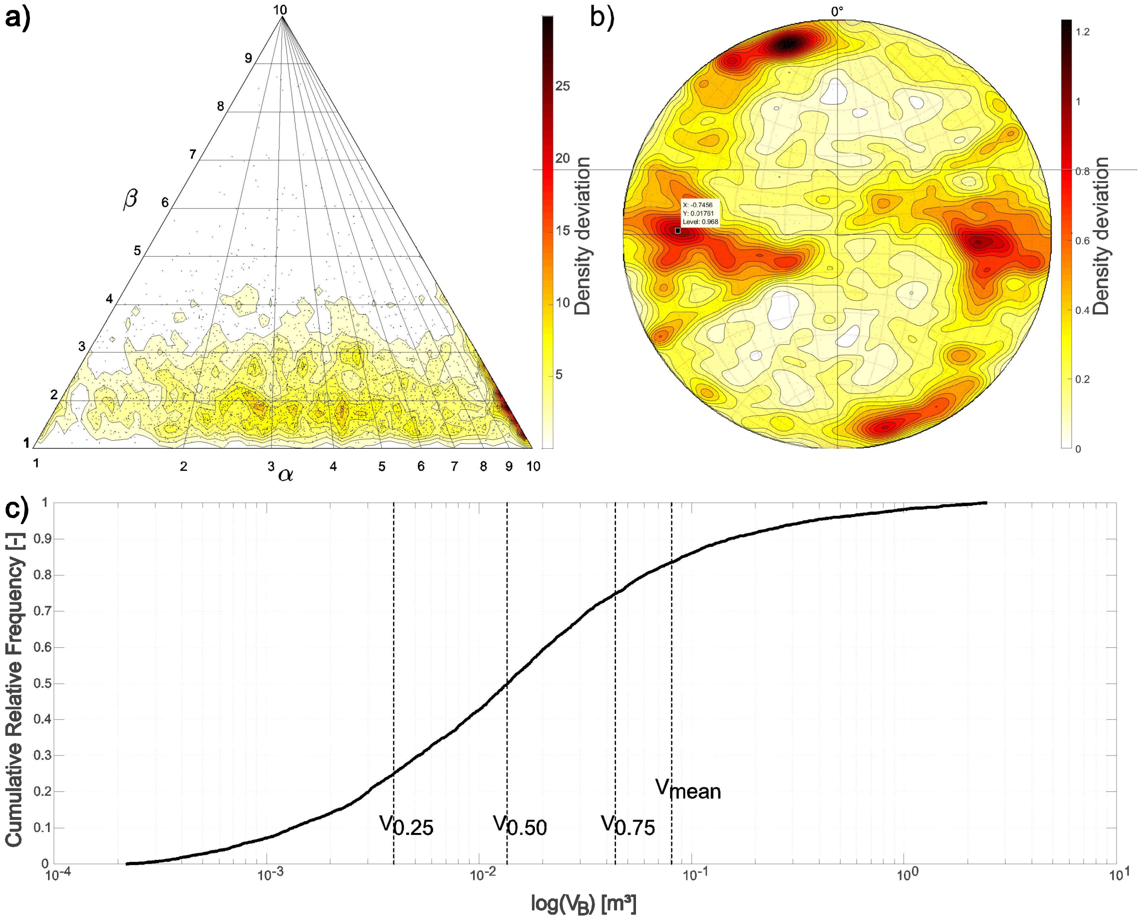

Figure 3.20: Geometric characterization of the joint network in the DFN of Case Study II; a) resembles the block shape distribution depending on the elongation and flatness of the single blocks, b) displays the distributions of the block orientations, regarding the vector-orientation of the longest block inter-vertex chord and c) shows the cumulative block size distribution (bold line); the values for the block volumes are given in Table 3.19.

Table 3.19: IBSD of the DFN in Case Study II, $V_{B,25}$ and $V_{B,75}$ represent the 25 %- and 75 %-quantile, .$\widetilde{V_B}$ is the median and $\overline{V_B}$ the mean block size.

	$V_{B,25}$	$\widetilde{V_B}$	$V_{B,75}$	$\overline{V_B}$	s_{VB}	$V_{B,min}$	$V_{B,max}$
Volume [m³]	0.004	0.014	0.044	0.081	0.243	0.0002	2.457

3.2.3 Block Stability Analysis

The results of the sensitivity analysis regarding the block stability analysis in Case Study II are shown in Figure 3.21 and listed in Table 3.20. The sensitivity analyses considered changing variations in the ratio between the principal normal stresses, ranging from $K = 0.33$, to 0.66 and 1, as well as different joint friction angles φ + 5°, an unchanged φ, and φ – 5°. As can be seen in Figure 3.21, $\Sigma V_{B,0.01}$ is increasing with each excavation sequence, ranging from almost 0 m³ in SSS-1 to more than 10 m³ after SSS-4 (at φ – 5°). Furthermore, the joint friction angle has apparently no influence on the block stability in the first excavation sequence, contrary to *K*: a low *K* allows block movements even in SSS-1. In contrast, no blocks are moving for $K \geq 0.66$. In SSS-2 the influence of both *K* and φ becomes more apparent. Whilst $\Sigma V_{B,0.01}$ is generally increasing, the blocks under higher circumferential stresses start to move also at a lower friction angle. This trend, however, is not observable for $K = 0.33$.

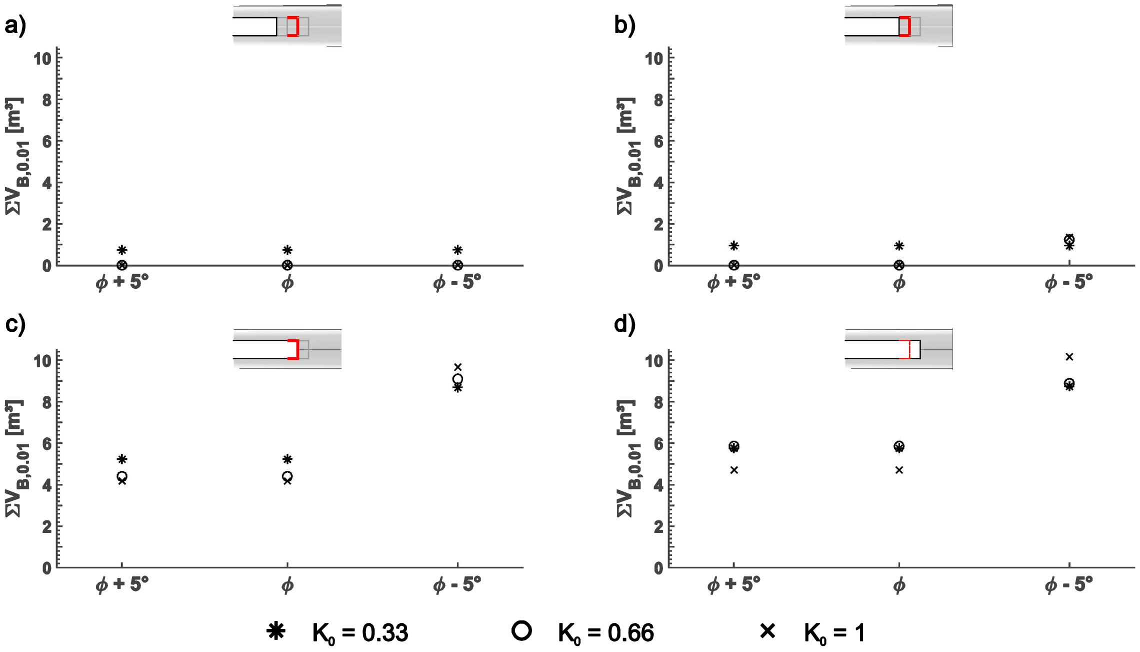

Figure 3.21: Results of the sensitivity analyses in Case Study II regarding the influence of the stress conditions (e.g. variations in *K*) and the joint friction angles (φ - 5°. φ and φ + 5° on the x-axis) on the total volume of blocks moving more than 1 cm after each excavation sequence ($\Sigma V_{B,0.01}$, on the y-axis); Results for $K = 0.33$ are given with a "*", $K = 0.66$ is given with a "o" and $K = 1$ is shown with a "x"; the results are given for each excavation sequence (SSS-1: subplot a, SSS-2: subplot b, SSS-3: subplot c, SSS-4: subplot d).

In excavation sequence 3 and 4 (Figure 3.21-c and d) the largest detaching block volumes are observed. Again, the models with φ – 5° led to a detachment of the highest $\Sigma V_{B,0.01}$ in both sequences. Furthermore, the influence of the lateral confinement also becomes more apparent. A higher volume of moving blocks is reached in SSS-3 for a lower *K*-value. The trend is, however, rather unaffected by the friction angles (with an exception of φ – 5°). The similar conclusions can be drawn from Figure 3.21-d, but with the difference that *K* seems to show dwindling importance with regard to the block stability. Additionally, $\Sigma V_{B,0.01}$ in SSS-4 is almost equal to $\Sigma V_{B,0.01}$ in SSS-3.

Table 3.20: Total volume of blocks, moving more than 1 cm in each excavation sequence in Case Study II for different joint friction angles ($\varphi + 5°$, φ and $\varphi - 5°$) and changing ratios between σ_1 and σ_3 ($K = 0.33$, 0.66 and 1).

K	Excavation Sequence	$\Sigma V_{B,0.01}$ [m³]		
		φ + 5°	φ	φ - 5°
0.33	SSS-1	0,748	0,749	0,750
	SSS-2	0,953	0,954	0,955
	SSS-3	5,234	8,168	8,688
	SSS-4	5,759	7,699	8,743
0.66	SSS-1	0,014	0,014	0,014
	SSS-2	0,014	0,015	1,242
	SSS-3	4,405	6,303	9,090
	SSS-4	5,851	6,408	8,889
1	SSS-1	0,012	0,012	0,014
	SSS-2	0,014	0,015	1,352
	SSS-3	4,187	6,670	9,674
	SSS-4	4,720	6,961	10,169

Figure 3.22 shows a comparison between the actual tunnel shape with the DSM (coloured in brown) and the numerical excavation profile (white, transparent blocks) for the SSS-3 (1st column) and 4 (2nd column) for the sensitivity case $\varphi - 5°$ and under different lateral confinements (rows). Blocks with a movement of more than 1 cm are deleted from the model to ease the visual comparability. In regions, where the approximation of the real excavation profile is poor, the brown DSM is less visible due to the overlay of several transparent blocks. This is particularly important for the tunnel face in SSS-3 as well as the tunnel periphery in SSS-4, where the actual tunnel face is already excavated. Apparently, the DSM is approximated poorly in the mid-section of the tunnel face in SSS-3, where the DSM is caving towards the rock mass. However, a god fit is reached in the left and right upper side walls – especially at the right side. The best fit in SSS-3 is reached in case of $K = 1$. In the last excavation sequence, K does not seem to affect the excavation profile considerably, since the numerical profiles look almost the same. This is confirmed by the very small differences in $\Sigma V_{B,0.0,1}$ especially between $K = 0.33$ and 0.66 (Table 3.20).

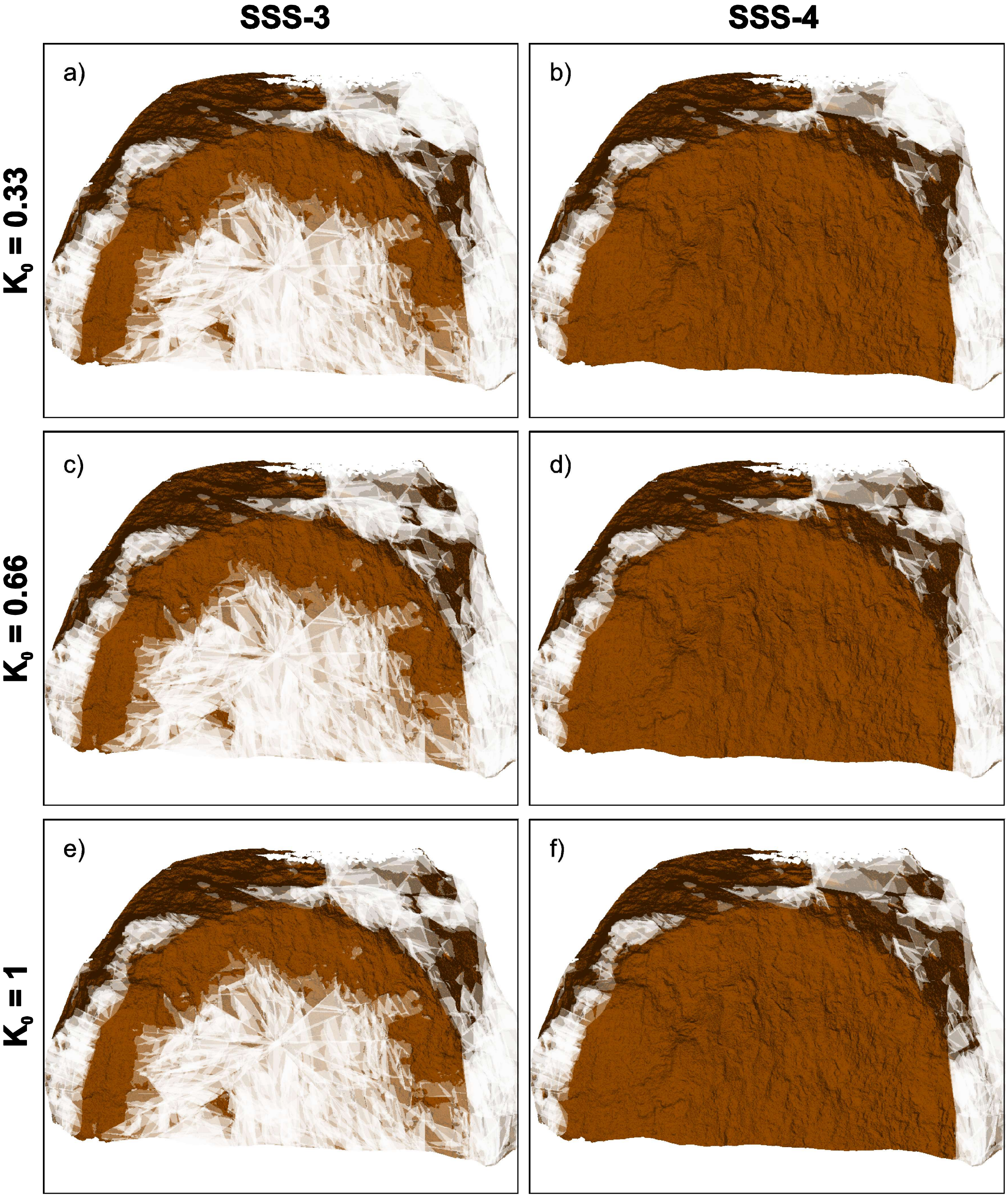

Figure 3.22: Comparison of the numerical excavation profile and the real tunnel shape (DSM) for different for *K* and a constantly reduced friction angle (φ – 5°); the DSM is displayed in brown, whereas the numerical excavation profile is displayed in form of transparent white blocks; blocks, moving more than 1 cm are deleted from the model; a and b show the SSS-3 and SSS-4 at $K = 0.33$, c and d show the SSS-3 and SSS-4 at $K = 0.66$ and figures e and f are the SSS-3 and SSS-4 at $K = 1$; the better the DSM is visible, the less blocks overlay it and the better is the approximation of the real excavation profile.

4 Discussion

The following sections discuss the results of the previous chapter. First, the methodology and the resulting joint network identification are discussed (section 4.1), second, the obtained characteristics of the rock mass regarding the block geometry are discussed (section 4.2). The discussion of the block stability analyses is given in section 4.3. Prior to the detailed discussion of each case study considerations are made about the general performance of the applied algorithms.

4.1 Joint Network

Prior to the discussion of the case-specific results of the joint network identification some general remarks about the performance are given. Afterwards, the results of Case Study I and II are compared to the tunnel documentation and prior publications, to discuss the case-specific performance of the applied methodology.

4.1.1 General Considerations

Comparing the geological sketches of the two case studies, it is very obvious that the amount of information provided by the sketches is quite different. While there are only some rough strokes for the joint traces and detached blocks, or only a few measurements for the joint orientations in the first case study (Figure 3.1), the drawing in Case Study II (Figure 3.12) has a very high level of detail. It provides not only information about the small-scale joint network geometry and the foliation and quite a number of joint orientations, but also lithological classes and locations of faulted/ruptured rock. This difference clarifies the necessity of an objective assessment of the rock mass, to ensure that everybody can draw the same conclusions from the same joint mapping and that there is as little room for interpretation as possible.

First of all, with both JTD and JPD a very large number of measurements were obtained. However, neither JTD nor JPD were able to map all the structures all alone. Otherwise the conjunction of both structure maps won't have been a simple addition or, as in Case Study II, more than 91 doublets would have been deleted. Instead, both techniques enhance the strengths and reduce the shortcomings of one another.

The rock mass in Case Study I is a paragon for the application of JPD due to the numerous distinct joint planes, whereas there are quite few joint traces and many changes in the colour, resulting in a poor performance of JTD. Case Study II was no paragon for JPD due to the lack of dominant joint planes; however, with high variations in colouring and shading due to the foliation, the application of JTD is favoured. As a consequence, the joint network could be identified mostly unsupervised in both case studies and still, the obtained results are very good and have an extremely high number of measurements (Case Study I: 1405; Case Study II: 2468) at a very high precision (see CoC in Table 3.6 and Table 3.16).

However, as stated in Buyer et al. (2018), both approaches are density based. This means that in JTD the kernel smoothening function was used to determine peak probabilities in the trace orientations and in the JPD, only peak values in the density distribution of the vector-orientations were used to identify principal joint planes. This means that only the most dominant structures are identified. The dominance is expressed either in large joint plane sizes or numerous smaller joint planes of the same orientation (JPD), or in clear orientation preferences of joints and lithological variations (JTD). If a structure occurs only as a single feature, like the documented faults in Case Study II (Figure 3.13-a), which leads neither to a considerably change in the surface morphology, nor appears as an explicit joint trace/change in the texture, these features cannot be located explicitly.

Although the applied methodology encompasses a two-staged segment linking, still some segments, which obviously belong to one structure, remain unlinked. A good example is the highly persistent joint trace in the mid-section of Case Study I, which is also mapped as a fault (Figure 4.1).

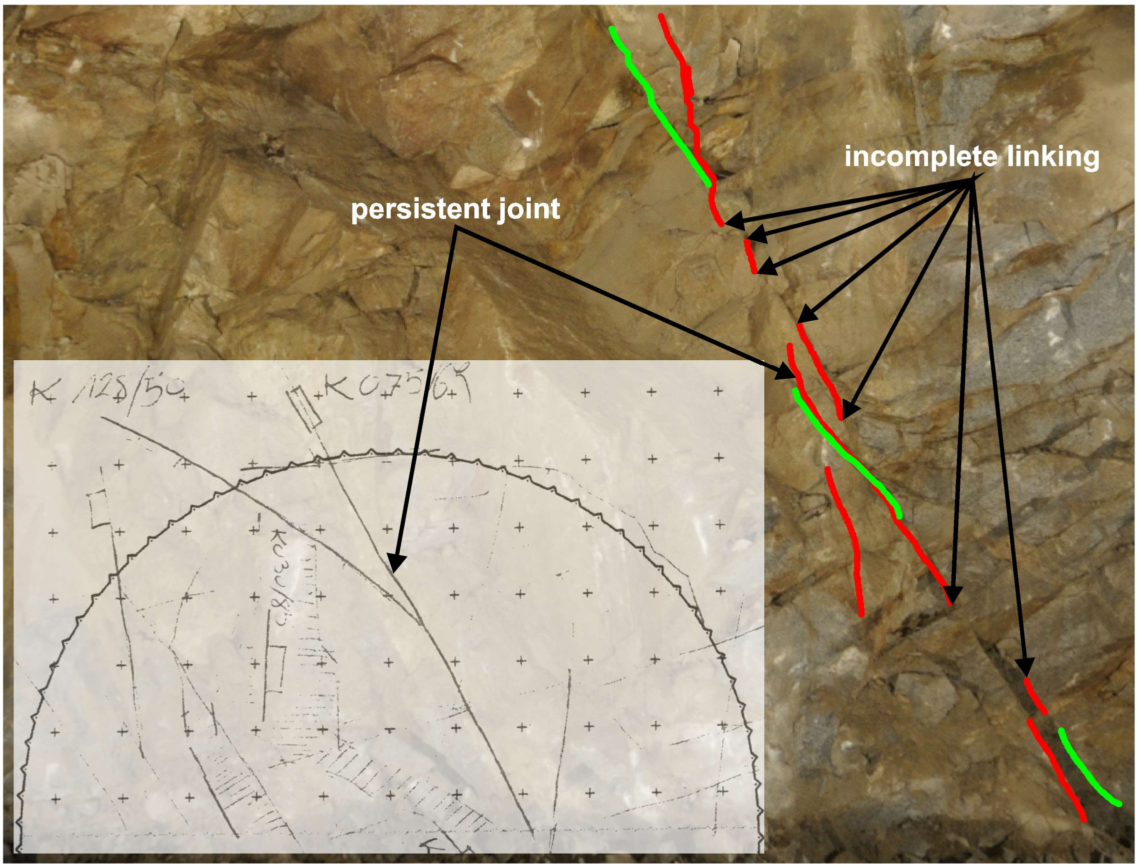

Figure 4.1: Example of an incomplete segment linking in Case Study I; according to the geological sketch (lower left figure), there is a highly persistent joint/fault passing through the mid-section of the tunnel face; in the JTD the general orientation is well captured (green and red traces), however the single line segments are interrupted and the linking is incomplete.

The JTD delivers parts of the joint trace, however, due to a) an assignment of the single segments to a different orientation cluster, those segments are not evaluated during the segment linking process, and b) due to too categorical boundary conditions for the linking (angular deviation, distance and linearity). Here, a higher flexibility, like a distance dependent angular deviation, or additional criteria, like neighbourhood characteristics might provide a higher robustness. Still, due to the extreme high number of measurements, those imperfections are not deemed to be statistically significant.

Regarding the post-processing in ShapeMetriX^{3D}, one of the major problems was the definition of the adequate number of joint sets. Mathematically valid results were obtained with a distinction of four to eight joint sets. However, a comparison with the geologic documentation led to a reduction of the number of joint sets. Especially in Case Study I, the JTD delivered nine distinct orientation cluster and the JPD delivered six distinct joint plane orientations. In contrast, only five sets were mapped by the geologist. By the combination of the information from JTD with the information from the JPD, each having their specific density peaks in the orientation values, a new density distribution is generated and the k-means clustering algorithm results in different set cluster. Additionally, the number of peak orientations from the JTD in Case Study I was extremely high due to the large variability of the 2D measurements. Nonetheless, those differences in the 2D orientation partly vanish when projected into 3D space. When a joint is intersected by two differently oriented surfaces, the 2D representation of the joint traces will show different angles. Still, not all documented joint measurements could be confirmed as distinct joint set orientations. Maybe also different clustering methods, like the DBSCAN-algorithm, and additional set specifications, like a characteristic joint size distribution or spatial location, might help in handling the higher number of set members and clustering single structures into distinct sets.

Nonetheless, a comparison of the proposed method with the on-sight mapping results from an experiences geologist shows that the automatically mapped sets are reasonably accurate and objective. Due to the very high quantity and the distinct localization of each single structure the direct generation of a discrete fracture network for numerical analyses is possible. Furthermore, a definition of distinct joint sets is only necessary in the calculation of the cumulative probability function of the apparent joint size distribution and the statistical enhancement towards the theoretical joint size distribution.

In both case studies, the computation of a statistical joint size distribution, based on real measurements, showed a clear shift of the values from very short joint traces towards larger sizes. Small joint sizes are more likely increased than bigger joint sizes, whilst avoiding an oversizing of large joints. This supports the underlying theory according which the apparent joint size can only be a lower value for the natural joint size distribution. Another side effect of the methodology is the shift of the distribution from a Weibull-function towards a Gaussian distribution.

The standard deviation, the mean and median values of the joint set spacing and trace length indicate that the values are not distributed uniformly and can be best approximated by a log-normal or Weibull distribution, as mentioned in Priest (1993), Stavropoulou (2014), Havaej et al. (2016) and Miyoshi et al. (2018).

Despite the very high fitting success of fitting the empirical CDF of the apparent joint trace lengths (R^2 is almost 1 and the RMSE is below 0.02 in all cases) there is a major drawback in this approach. The analytical function tends to underfit shorter joint traces and overfit longer joint traces up to the point, where the functions approximate the probability limit of 100 %. Exemplary values from the fitted function in Case Study I – JS1 are given in Table 4.1.

Table 4.1: Differences due to under-fitting of the analytical solution onto the empirical cumulative density function of the apparent joint trace lengths in JS1 of Case Study I.

$P(L)$ [%]	L_a [m]	L_t [m]
0.1	1,125	0.113
0.7	4,646	0.499

By interpolating the aCDF, this under- and overfitting can be eliminated. However, with a fitted analytical function, the rock mass can be described in numeric values, which eases the classification, description and comparison of different rock masses. This is not possible, if $P(L_t)$ is derived by interpolating the eCDF. Nonetheless, the interpolation would result in a higher precision. Furthermore, according to equation 2.9, no joint sizes below the variables $a + c$ are allowed. This can be observed in Figure 3.19 and Figure 3.8 and explains, why the line diagrams do not start at 0,0 or with the values from apparent joint size distribution. This seems like a drawback in the methodology, but under the assumption that a) small joints do not contribute to the general rock mass stability and b) small joints form only small blocks, which are therefore below the block size criterion, the incapability to detect joints below this threshold ($a + c$) is deemed acceptable, since both a and c are floating values in a centimetre range.

4.1.2 Case Study I

The joint trace detection delivered almost 600 distinct joint traces, which included also the fault traces, which were not detectable with a purely vector-based joint plane detection. These 576 single traces are assigned to nine distinct orientation cluster and some seem to be almost subparallel to each other despite belonging to different clusters. This is on the one hand due to the fact that with the chosen setting for the secondary orientation filtering, a very high degree of detail and therefore a high number of distinct peak orientations has been achieved. Hence, the angular deviation between two adjacent clusters is very little and in a further post-processing, most of the orientation cluster will be merged into one major cluster. However, although a two-staged segment linking technique was applied, there are still some line segments, which are linked either incorrectly (some line segments still expressed branching), or not at all, although the geological judgement would connect the two separated lines (see joint traces of fault structure in the mid-section). This is on the one hand caused by the assignation of segments into different orientation clusters, or the relatively simple linking criteria, since they only base on the deviation of the orientation of the linking line compared to the separated line segment and the distance criterion. A more sophisticated interaction of distance-related linking boundaries is expected to lead to improvements in the results.

However, the resulting joint trace maps is still consistent and depicts the joint network good. On the second hand, a joint trace, intersecting two different joint planes appears in 2D with two different trace angles, which are consequently assigned to different orientation cluster in the JTD. If the traces are transposed into 3D space, the two orientation clusters are merged into one set again. Therefore, the number of orientation cluster from the JTD exceeds in the most cases the number of joint sets from a 3D analysis.

Since the chosen tunnel face expresses a very blocky rock mass with very clear joint planes, the vector-based point cloud processing delivered also apparently reasonable results (Figure 3.4). In total, almost 800 distinct planes and six different joint sets were distinguished. The joint plane detection led to the identification of distinct joint planes in both the tunnel face, as well as the side walls and roof section. However, the highly persistent fault in the mid-section of the tunnel face was not detected, since it dipped directly along the line of sight and appears only as a joint trace without clear joint planes. The denser fracturing on the right bottom region (classified as GT2) is also captured with some measurements. One of the most sensitive parameters in the DSE analysis was the selection of the minimum joint size, represented by the minimum number of assigned points. This parameter however correlates with the resolution of the point cloud or the average 3D point spacing. In the processed point cloud, the point spacing was 2 cm due to the relatively low number of points (~600k) in the point cloud.

The conjunction of JTD and JPD reduced the number of the previously determined joint sets to five. This however is surprising, since the JTD delivered nine dominant orientation sets and six distinct sets were distinguished via JPD. The extremely high number of orientation cluster from the JTD is qualified earlier. There is not much of a difference between the number of sets from the JPD and the conjoined set information. The re-clustering via the k-means algorithm resulted in an optimum clustering result of five distinct joint sets, but a higher number of distinct sets is not excluded. However, the project documents revealed also five distinct joint sets. Nonetheless, there is still quite some difference, expressed with the acute angle between the manually and the digitally mapped joint set orientations (Table 4.2).

Table 4.2: Acute angles between the mapped and the semi-automatically derived joint sets; SA refers to the spherical aperture of the conjoined joint set, a weak match, where a connection can only be guessed is marked in italic and bold; a good match, where the angular difference is less or close to the SA are highlighted in bold upright numbers.

			Project documents					
	Joint Set	SA	fault	k1	k2	k3	k4	Tunnel face
Joint Sets in Case Study I	JS1	24°	*53°*	*39°*	*51°*	**21°**	*72°*	*31°*
	JS2	24°	*75°*	*43°*	**12°**	*60°*	*52°*	*25°*
	JS3	22°	*81°*	*80°*	*64°*	*52°*	*84°*	*84°*
	JS4	22°	***38°***	*46°*	*86°*	*86°*	*47°*	*76°*
	JS5	23°	*74°*	*85°*	*51°*	*61°*	**25°**	*27°*

Some joint set from the digital joint mapping correlate very well with the set orientations from the project documents (e.g. JS1 with k3, or JS2 with k2 and JS5 with k4), where the angular deviation is less or very close to the spherical aperture of the respective conjoined joint set. In other cases, a connection can only be guessed (e.g. JS4 with the fault structure) or cannot be established at all (JS3, or k1). The most reasonable explanation for this is the fact that joint sets from the manual mapping are based on a very low number of measurements, missing the natural variability in the orientation values of a joint set: During the tunnel documentation, only seven joints were mapped on-site and the rock mass classification is based mostly on the geological understanding and experience of the mapping geologist. On the opposite, the results of the proposed method have a very high accuracy (CoC $\leq 3°$) and statistical reliability. This leads to the assumption that a higher number of measurements might result in a better correspondence between the automatically derived joint sets and the manually mapped sets due to a higher accuracy of the manual results. As an example, Buyer & Schubert (2017) performed a detailed manual mapping of the tunnel face in Case Study I. The results are listed in Table 4.3. The measurements were also distinguished into five distinct joint sets. A comparison to the conjoined mapping results from JTD and JPD is given in Table 4.4.

Table 4.3: Results of the manual joint mapping of the tunnel face in Case Study I according to Buyer & Schubert (2017); DoC = Degree of Concentration, CoC = Cone of Confidence; NoM = Number of Measurements.

Set ID	Dip Direction [°]	Dip Angle [°]	SA [°]	DoO [%]	CoC [°]	NoM
I	45	59	6.4	17.5	91.0	25
II	123	65	7.9	21.4	86.7	25
III	220	87	5.7	18.1	90.4	33
IV	312	74	5.0	18.0	90.4	42
V	236	36	5.8	23.3	84.3	53

Table 4.4: Acute angles between the obtained results from the manual joint mapping according to Buyer & Schubert (2017) given in roman numerals (I to V) and the coupled joint identification in the tunnel face of Case Study I (JS1 to JS5); angles below or close to the set specific spherical aperture (Table 4.2) are highlighted in bold letters.

			Manual mapping from Buyer & Schubert (2017)				
	Joint Set	SA	F	II	III	IV	V
Joint Sets in Case Study I	JS1	24.3°	84	***30***	65	42	69
	JS2	24.3°	57	59	61	***31***	84
	JS3	22.1°	72	70	74	72	**23**
	JS4	21.8°	51	58	***37***	55	46
	JS5	23.3°	57	59	60	***31***	84

The angular deviations reveal that again there is no perfect correspondence between the manual mapping results from Buyer & Schubert (2017) and the results of the proposed method. Still a better match than with the documented set is achieved, since five instead of three matches are found. The angular deviation between the manually and digitally mapped structures shows that the acute angle between the joint sets JS1 and II, JS2 and IV as well as JS5 and IV are very close to the spherical aperture. JS3 and joint set V show a very good match. Joint set III can be roughly referred to JS4.

This supports the theory that a higher number of measurements for a natural joint set increases the accuracy in its identification. Still, the five matches include a double-correspondence (JS2 and JS5 with IV), which means that a unique assignation cannot be achieved, and 4 of the five matches are only weak, meaning that the angular deviation is larger than the spherical aperture of the conjoined set. Furthermore, joint set I has no counterpart in the automatically mapped sets. Referring to Table 4.3, the very low spherical apertures (5° to 7.9°), compared to the automatically mapped sets is obvious (21.8° to 24.3°). This clarifies, that the mapped structures are mapped subconsciously according to their spatial orientation and although the mapping results were also re-clustered afterwards using the k-means algorithm, their original similarity in orientation prevails. Hence, the results are slightly biased by the subjective assessment of the rock mass geometry. In contrast, the proposed method works completely objective, checking only for mathematical solutions and hence results in both a higher deviation from the mean set orientation (i.e. a larger SA) but also a more accurate assessment of the joint set orientation due to a much higher number of measurements (more than 1400 measurements by the proposed method vs. 178 manual measurements).

The spacing of JS4, which also includes the fault of the geological mapping can be shown off with a mean set spacing of 0.75 m and a standard deviation of 1.32 m (Table 3.7) and a median set spacing of 0.21 m instead of the mapped/estimated 2 m (Table 3.2), but still, the joint set spacing of JS4 is the highest of all distinguished joint sets, which corresponds also to the project documents. The set also shows the lowest joint frequency. Unfortunately, the high persistence is not captured by the methodology. This lack is mainly due to the fact, that the actual joint is not captured as one single structure, but composed of several small to medium sized structures. Furthermore, the fault is not revealed as one single feature but belongs to a larger set of measurements with varying size. The applied clustering is based on orientation values without consideration of the geologic genesis of the structures. A possible criterion, to distinguish automatically between genetically different structures might be e.g. the joint size.

An accordance was found between k2 and JS2 in both the orientation values and computed joint set spacing. The set spacing according to the geological documentation is given with 20 to 60 cm. The computed mean set spacing is given with a mean spacing of 0.32 and a standard deviation of 0.42 m, which is within the estimated range. Even so, the median set spacing (0.15 m) is lower than the estimated range. A comparison of the values for the set spacing of JS5 with the mean joint normal spacing of k4 expresses a similarly result with a mean set normal spacing of 0.21 and a standard deviation of 0.27 m matching with the estimated range of 20 to 60 cm, but a much lower median set spacing of 0.11 m. Large differences are in the documented and computed mean set spacings of JS1 and k3. The analyses resulted in a mean normal spacing of 0.61 m and a median spacing of 0.3 m, which is much less than the documented 2 m spacing for k3. The standard deviation is with an value of 0.74 m relatively high. This difference can either be explained by a biased analysis, e.g. insufficient segment linking or insufficient detection and exclusion of doublets, or by an overestimation of the set spacing by the mapping geologist. k1 does not appear as a distinct joint set and hence a direct comparison with the computed set spacings is hardly possible. The results clarify that with the proposed method it is possible to assign tangible numbers and numeric ranges, given e.g. as a standard deviation, to ground types, rather than being limited to estimated ranges and categories for the spacing (ISRM, 1978, ÖNORM EN ISO 14689).

Generally, the joint traces are short (0.48 to 0.87 m, Table 3.7) and the high persistencies (up to more than 2 m) of the documentation are not captured. This on the one hand originates from the incomplete segment linking, which still leads to an underestimation of the actual joint trace length and on the other hand from the blockiness of the tunnel face, since the applied algorithms deliver only distinct joint planes, two planes, which would belong to one geological structure or lie on one plane cannot be merged. Still, the suggested method of the statistical increase of the joint size, based on the joint diameter, seems also promising. The results (Figure 3.8) show that small joints were generally increased by size and the larger joints remain unchanged.

4.1.3 Case Study II

The exposed tunnel face in Case Study II (Figure 3.13) does not show many obvious joint planes. In fact, the rock mass is dominated by the foliation, which is evident by a layered alternation of felsic and mafic units (Figure 3.12-a and b). Therefore, the investigated point cloud is not a paragon for the application of JPD. Instead, very good results were expected from the JTD. However, the lacking applicability of the JPD was partly compensated by the high density of the point cloud, having a disadvantage in detecting more noise and increased computation time.

As described in the tunnel documentation (Table 3.11), overbreak occurs due to block detachments along the foliation and by the intersection of joints with the foliation in the side walls. The foliation, however, does not daylight as large, distinct planes. Hence, the foliation was captured by the JPD only with a low density (JPD_3 in Table 3.15). Still, the angular deviation between the documented foliation and JPD_3 is 15°. Although the DSE results do not reveal joint planes in the region of the mapped fault zones, it seems that there are quite some fault related structures in the rock mass. This is proven with a very good accordance between JPD_2 and the fault orientation at an angular deviation of only 18°. Nonetheless, a biasing influence of the almost planar tunnel during the JPD analyses can be seen at the example of JPD_1: The set orientation deviates only by 9° from the tunnel face and the very high density of the assigned points superimposes subordinated/subparallel structures.

A comparison of the on-sight mapped joint sets with the conjoined mapping results from JTD and JPD in Table 3.16 is given in Table 4.5. The table is showing the acute angles between the manually and digitally mapped joint sets as well as the mean orientation of the tunnel face (150/90).

Table 4.5: Acute angles between the manually mapped joint sets and the joint sets obtained by the conjunction of JTD with JPD; angles below or close to the set specific spherical aperture (Table 3.16) are highlighted in bold letters; SA refers to the spherical aperture of the conjoined joint set.

			Project Documents			
	Joint Set	SA	sf	k	st	Tunnel face
Joint Sets in Case Study II	JS1	*23.5°*	*73°*	**25°**	*83°*	*49°*
	JS2	*18.5°*	**12°**	*85°*	*69°*	*85°*
	JS3	*21.8°*	*88°*	*70°*	***32°***	*89°*
	JS4	*18.1°*	***28°***	*65°*	*78°*	*51°*
	JS5	*27.8°*	*79°*	*58°*	*68°*	***36°***

According to this comparison, there is a very good consensus between JS2 and the foliation (12° angular difference!), a good consensus between JS1 and k as well as a fairly well accordance between JS5 and the tunnel face. A very weak conformity can be seen between the set orientations of JS3 with the fault zone and JS4 with the foliation as well.

JS2 and JS4 are apparently representing the foliation, including its metamorphic character. The geological sketch also indicates that the foliation is wavy and folded. Hence, JS2 is representing the sub-horizontal discontinuities, whereas JS4 is representing the inclined foliation in folds. A combination of JS2 with JS4 into one joint set would not only reduce the number of mathematically distinguished joint sets to the actually documented number of joint sets, but would also lead to an angular deviation of only 9° between the foliation and the mean orientation of JS2∪JS4 (321/17).

Unlike with the sole application of JPD, a clear distinction of the tunnel face is not possible anymore after conjoining JPD and JTD. This shows the necessity of combining the two information sources, in order to minimize the bias. In this case it is the superimposing of a hidden structure (JS1 respectively k), which would be missed by a sole application of the DSE. The actual tunnel face however, is assigned to JS5, but again there seems to be a hidden structure due to the larger angular deviation between the tunnel face and JS5. The fault structure is not very obvious in neither the point cloud nor the digital image, still JS3 shows a weak connection to the fault zone and the measurements primarily result from the JTD. But the large angular deviation between the fault orientation and JS3 suggest that the results are biased and a close inspection of the structure elements in JS3 reveals, that quite a few assigned joint traces in the tunnel face are actually such scratch marks. However, the majority of the set structures occur all over the left side wall and partly at the lower right side wall, and therefore suggest the existence of a real discontinuity set.

At a close investigation of Figure 3.16, one might notice the accumulation of measurements occurring in the pole point distributions of JS2 (foliation) and JS3. Most of the measurements are resulting from the JTD. A reason for this alignment is on the one hand a biased measurement due to an ambiguous plane fitting in SMX due to a too low morphology in the point cloud or too short trace lengths. On the other hand, it seems that this accumulation is connected to the tunnel face orientation (150°), since it seems to follow a great circle with a dip direction of 170° and 330°, respectively.

Especially the median joint normal spacing of JS2 ($\tilde{X}_s$ = 0.09 m) fits within the estimated range of the foliation from the tunnel documentation (0.06 to 0.2 m, Table 3.12 and Table 3.17). The mean value ($\bar{X}_s(JS2)$ exceeds the estimated range almost by the factor 2. The computed standard deviation is also relatively high (0.7 m). $\tilde{X}_s(JS1)$ and $\bar{X}_s$(JS1) are computed with 0.39 m and 0.65 m, which also matches with the documentation (0.2 to 0.6 cm and wider). Since JS5 is representing a joint set, which is sub-parallel to the tunnel face and is not specified in the project documents, a comparison of the values for the normal spacing is not possible. The median set normal spacing of JS3 ($\tilde{X}_s$ = 0.14 m) underestimated the values from the documentation to a very large extent. Nonetheless, the mean set normal spacings approximates the estimations from the tunnel documentation: $\bar{X}_s$(JS3) = 0.97 m. Even so, there is also a high standard deviation in the measurements (s_{Xs}(JS3) = 1.92 m). The differences between the mean and the median values as well as the high standard deviations are blamed to the non-uniform distribution of the measurements.

The approximation of the cumulative density distribution of the joint sizes by the double-exponential function worked very well and only small deviations occurred primarily in the range of joint sizes below 0.5 m (Figure 3.17). The comparison of the density distributions of the joint sizes respectively the trace lengths (Figure 3.19) shows that most joints are rather short (0.1 to 0.25 m). This fact remains even after the statistical enlargement. However, the distributions are clearly shifted towards longer trace lengths and therefore larger joint planes in the DFN. Still, a comparison of the enlarged joint sizes (Table 3.17) with the documentation (Table 3.12) reveals that the majority of the joints are still underestimating the actual size. This is explained by the mentioned incomplete segment linking during the JTD and the fact that there were no major joint planes detected in the JPD.

The relatively high computation time for capturing the joint network is a ramification for the on-sight application. However, the computation time is highly dependent on a) the number of measurements – the lower, the faster – b) the computational power of the used computation unit and c) the implementation and efficiency of the numerical code. Referring to a) a very high number of joint traces was analysed. This high number is caused by the relatively low threshold for the minimum joint trace length. Hence, with a higher threshold, the number of measurements would drop and the computation time as well. Referring to b) the trend for an increasing computation power is still present and reductions in the computation time are expected here as well. Regarding point c) it is very likely that the code can be improved to a large extend, which also leads to a reduced computation time.

4.2 Rock Mass Geometry

As stated in sub-section 1.3.2 an objective determination of the rock mass geometry is important for the block stability and consequently the excavation profile. Furthermore, it influences the consumption of explosives and the amount of material, which has to be mucked.

4.2.1 General Considerations

The determination of the rock mass geometry is very objective since they are obtained purely based on the blocks within the DFN region and their geometric properties, like vertex coordinates, volume and surface area. The obtained joint network led in both case studies to the generation of platy and cubic shaped blocks. Elongated blocks were not observed. This is in accordance with the geologic documentation and the impressions by the DSM of the tunnel faces.

However, 3DEC allows only convex blocks. Hence, in case an intersection of fractures, which would lead to the generation of a concave block, will subdivide the area in two (or more) smaller but convex blocks. Hence, the block size distribution might be blurred. But this is seen as rather subordinated and not sensitive to the results.

Since the export of the necessary block information from 3DEC is easy and the evaluation of the data was performed with an automated Matlab-script, the results were produced very fast (~5 to 10 min) despite the very high number of single blocks. This high number is also a source of reliability and statistical reproducibility.

4.2.2 Case Study I

As shown in Figure 3.9-a, most of the blocks are assigned to the shape classes “platy” and “cubic”, with subordinated peak distributions in “cubic to platy”. β ranges between 1 and 2 and α has a peak distribution between 1 and 1.1 as well as 9.8 and 10. This is in good correspondence with the information about the general joint set specifications, especially the spacing, which is very similar for all joint sets, and the orientation, since the dip angles are also very similar.

A dominant block orientation cannot be detected (Figure 3.9-b). Although there are five peak densities in the plot (densities higher than 0.6), only two of these peaks can be assigned to specific joint sets: it seems like JS2 and JS3 control the block orientation. In case of JS2, the results are also consistent with the set normal spacing, which is the highest of all detected joint sets (0.87 m). This high value suggests that once a block is formed by the intersection of joint planes with structures from JS2, its size and hence influence on the results is very high. The dominance of JS3 can be explained by the sheer number of measurements, which is by far the highest, compared to the other sets. Hence, the probability that JS3 is forming a block is also very high. The other peak orientations are rather obscure, since there are neither big differences in the spacing, orientation or number of measurements. Still, since JS3 is not confirmed by the on-sight mapping, it is also possible that the results are highly biased.

The rock mass in the DSM appears very blocky with large-sized blocks, however, the determined median block volume is only 0.014 m^3 (≙ 14 l). In contrast, the mean block size is almost ten times bigger (0.0124 m^3) and the very high standard deviation (~ 0.5 m^3) indicates that the block size distribution is neither following a normal distribution, nor appears to be very homogeneous. This wide range of block sizes is a result of the wide range of joint sizes in each set (Table 3.7). Since the measurements due to the blocky character of the rock mass, are well spread across the tunnel face, a bias due to local differences in fragmentation can be excluded. Nonetheless, during the model generation, e.g. definition of the tunnel geometry, segmentation of the excavation sequences and the densification, artificial cracks are introduced into the model, which might lead to a higher fragmentation as it would naturally be. Still, a comparison of the determined block sizes with the conventionally determined block volumes, according to Palmström (2001), Cai et al. (2004), or Wang et al. (2003) would clearly show that V_B, determined by the DFN is still higher, than the empirical approaches, which is quite reasonable, since the standard empirical approaches a) consider persistent joints, b) allow only a limited number of joint sets and c) neglect local deviations in the fracture pattern. This theory, however, has not been tested, since the approaches are restricted to three distinct joint sets. The assumption is based on the explicit implementation of the joint size, respectively persistence, which is poorly considered in the analytical formulations. The size increasing effect of a considered and neglected joint persistence is displayed in Figure 4.2. The results obtained by the DFN representation are shown with a solid line. The results of a statistically rock mass representation, with considering infinite joint sizes is displayed with dashed lines. The statistical representation uses the joint set specifications given in Table 3.7, including standard deviations for the orientation (ς_{DD} and $\varsigma_D = 5°$). The persistence is set to 100 %. With regard to the statistical deviation, the model was generated with 20 replications. The quantile values of the statistical and DFN representation are given in Table 4.6. It is obvious, that the block sizes, obtained by the DFN simulation are higher than the block volumes in the statistical rock mass geometry by a factor of almost 2 to 3. This difference in the IBSD is quite good, since in the theoretical model, the infinite persistence leads to an underestimation of the actual block size: With infinite joint planes, too many intersections are possible, which are not present in nature (e.g. Kluckner et al., 2015, Aichinger, 2018). Hence, the better the persistence or joint size can be approximated, the better is the resulting ISBD. Consequently, with the innovative approach to estimate the joint size, and the deterministic modelling of the fracture network, the ISBD is approximated very well.

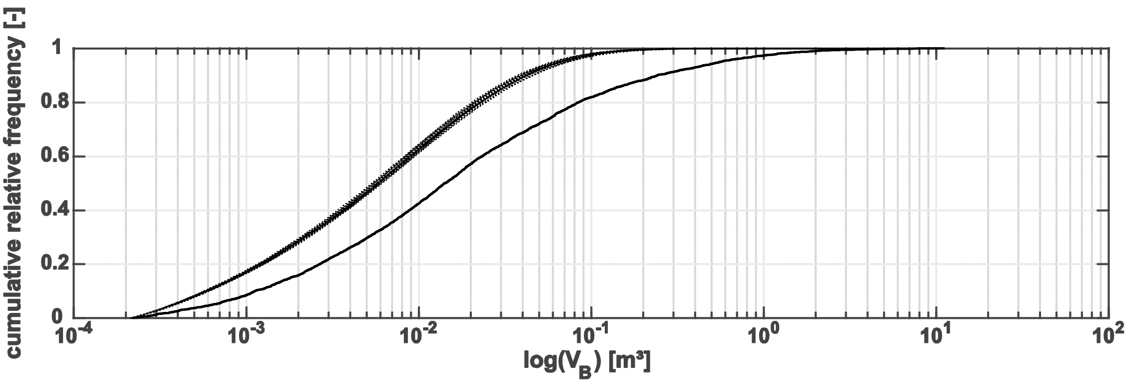

Figure 4.2: Comparison of the block size distributions obtained by the generation of the DFN (solid line), including information about the joint size, with a statistical representation of the joint network geometry (dashed lines) according to the set specifications in Case Study I and a persistence of 100 %.

Table 4.6: Quantile values of the IBSD of the DFN and the statistical rock mass geometry (sRMG) in Case Study I, $V_{B,25}$ and $V_{B,75}$ represent the 25 %- and 75 %-quantile, .$\widetilde{V_B}$ is the median and $\overline{V_B}$ the mean block size.

Rock mass representation	$V_{B,25}$ [m³]	$\widetilde{V_B}$ [m³]	$V_{B,75}$ [m³]	$\overline{V_B}$ [m³]
DFN	0.004	0.014	0.061	0.081
sRMG	0.002	0.007	0,020	0,018

4.2.3 Case Study II

In Case Study II the block shape is dominated by the “platy” class with decreasing densities in “cubic to platy” and “cubic” (Figure 3.20-a). This block shape class is characteristic for foliated rock masses and is confirmed by the very low joint spacing for the foliation (JS2, Table 3.17). The platy appearance is also indicated by the geological sketch of the tunnel face in Figure 3.12-b. This platy shape is disrupted by the other four joints and the resulting blocks are rather cubic in shape.

Another correspondence is achieved in the determination of the dominant block orientation. As shown in Figure 3.20-b, the peak densities range around 339/02, which matches with the orientation of the intersection of JS3 with the foliation (JS2). This dominance is caused clearly by the extremely large number of measurements, their even distribution in the numerical model, as well as the very high joint frequency. The subordinated peak orientation of 272/27 is probably caused by the intersection of JS1, which has the second highest joint frequency and represents fault zone related structures, with JS4, which represents foliation elements with a steeper inclination. The third peak orientation cannot be assigned to any specific set intersection, but if the orientation of the density centre is switched by + 180°, it coincides with the second peak orientation again. Hence blocks, generated by the intersection of JS1 with JS4 seem to be unspecific in their orientation, which can be caused by the more compact block shape character, i.e. a higher tendency to cubic shaped blocks.

The block size distribution using the DFN approach, gives a median V_B of 0.014 m^3. However, the high mean value and standard deviation indicate the heterogeneity of the generated block sizes. This heterogeneity is caused by a non-uniform distribution of the joints in the numerical model, since most of the measurements and therefore discrete fractures are positioned at the tunnel periphery and only a few joints are located right in the tunnel face – apart from measurements for the foliation. A second source for a biased result is, like in Case Study I, the process of the model generation itself. Artificial cracks due to the excavation geometry and sequencing can bias the natural IBSD. Nonetheless, the real block size distribution seems to be approximated very well.

The main advantage of using a DFN, directly linked to mapping results, is that no assumptions had to be made regarding the joint sizes or set persistence. The difference between the DFN based block size distribution (solid line) and a statistical representation of the rock mass with infinite joints (dashed lines) is shown in Figure 4.3. The deterministic DFN-approach, presented in this thesis, includes explicit information about the joint sizes and persistence and locations, whereas the statistical approach is using the joint set specifications given in Table 3.17 and uses a persistence of 100 % for each joint set. The curves express similar shapes, but the sizes are apparently smaller. The quantile values of the statistical and DFN representation are given in Table 4.7. It is obvious that the block sizes, obtained by the DFN simulation, are almost twice as high as in the statistical rock mass geometry.

Table 4.7: Quantile values of the IBSD of the DFN and the statistical rock mass geometry (sRMG) in Case Study II, $V_{B,25}$ and $V_{B,75}$ represent the 25 %- and 75 %-quantile, .$\widetilde{V_B}$ is the median and $\overline{V_B}$ the mean block size.

Rock mass representation	$V_{B,25}$ [m³]	$\widetilde{V_B}$ [m³]	$V_{B,75}$ [m³]	$\overline{V_B}$ [m³]
DFN	0.004	0.014	0.044	0.081
sRMG	0.002	0.006	0,018	0,016

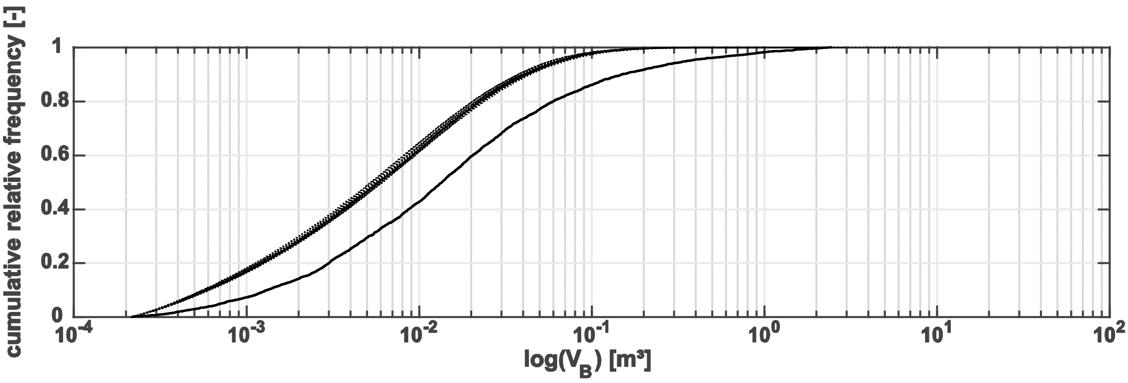

Figure 4.3: Comparison of the block size distributions obtained by the generation of the DFN (solid line), including information about the joint size, with a statistical representation of the joint network geometry (dashed lines) according to the set specifications in Case Study II and a persistence of 100 %.

4.3 Assessment of Computed Overbreak

In the following section, the computed excavation profiles, after deleting all blocks moving more than 1 cm in the numerical models, are compared to the geological documentation (Figure 3.1-b and Table 3.1 for Case Study I; Figure 3.12-b and Table 3.11 for Case Study II) and digital surface models. The results preliminary focus on the stability trends, controlled by the shear resistance of the joints (i.e. variations in φ) and the lateral stress conditions (i.e. variations in *K*), rather than on the determination of the real joint and rock mass properties, or stress conditions.

4.3.1 General Considerations

In general, the jointed rock mass was represented very well in the numerical analyses. The position of the block failures according to the geological documentation fitted with the block detachments in the numerical analyses. Also, the amount of overbreak did in no case exceed the documentation significantly. Very good correspondences were achieved in the investigated cases with a low circumferential stress around the excavation and low joint friction angles. The difficulty in defining a persistence value for the joint sets was avoided by measuring the apparent joint trace length and computing an analytical joint size, which was used in the DFN representation of the joint network. This also enabled a unique and site-specific reconstruction of the actual conditions at the investigated tunnel faces.

The simulations were performed with a limited number of calculation steps (Table 2.4). Instead of searching for a stable state, the simulations were stopped earlier. This resulted in an incomplete mobilization of all possible blocks, but prevented long computation times, when only block falling occurred. Hence, the results for $\Sigma V_{B,0.01}$ in Table 3.10 and Table 3.20 are not representing the block volumes in equilibrium and might increase at more computation steps, but the general trend is demonstrated.

A practical side effect of using a DFN in the numerical simulations is the reduced number of blocks, which are still sufficient to investigate the tunnel stability: blocks are only generated, where discrete fractures intersect and the number of fractures – although it is very high within a given area – is rather low compared to the number of distinct joints, which would have been generated in a statistical representation of the rock mass. This becomes most obvious in Case Study II where the foliation is controlling the tunnel shape and therefore needs to be represented as detailed as possible but has on the contrary an extremely narrow spacing of only a few centimetres. An accurate representation of this narrow spacing would require the generation of numerous blocks, which would consequently increase the computation time approximately by the power of 2. With a highly detailed representation of the joint network at the station of interest and its vicinity, the narrow spacing as well as the local deviations are captured very well and still, the number of blocks is limited.

4.3.2 Case Study I

The applied method resulted in a generally well to fairly good match of the modelled excavation profile with the real profile (Figure 3.11). The location of DCF, when it occurred in the numerical analyses, was in a good correspondence with the DSM, however with minor differences in the magnitude and depth due to the joint network geometry. This is particularly the case for the tunnel periphery. The tunnel face was not reconstructed in a too good correspondence with the DSM, which might be either caused by too high friction or dilation angles, resulting in too high resisting forces on the sliding planes. Nonetheless, with decreasing friction angles, the location of numerical DCF was similar to the DSM.

In Table 4.8, the correspondences of the modelled excavation profile with the DSM in the last two excavation sequences (SSS-3 and SSS-4) are summarized according to the considered friction angles. The correspondences are classified in poor ("-"), moderate ("o") and well ("+"), to ease the comparison. In SSS-3, block sliding on joint planes is possible in the tunnel face of the SOI. In SSS-4, only blocks detaching from the roof and subordinated block sliding from the side walls is possible, since the SOI is already excavated.

Table 4.8: Comparison of the computed excavation profile with the DSM in the excavation sequences SSS-3 and SSS-4 with variations of φ in Case Study I; poor correspondences are given with "-", moderate correspondences with "o" and well correspondences are given with "+".

Variation of φ	Excavation Sequence	
	SSS-3	SSS-4
φ + 5°	-	+
φ	o	+
φ – 5°	+	+

A further decrease of the friction angle is not deemed necessary, since the trend of the values (Table 3.10 and Figure 3.10) already points to a stabilisation of the rock mass, with the majority of potentially instable having detached. The higher joint friction angle (φ + 5°) leads to a stabilization of almost 30 % of the kinematically free blocks.

The sensitivity analyses confirm that the block detachments in the roof section are rather independent from the friction angle, whereas the mechanical freedom of blocks, detaching from the tunnel face, is sensitive to φ. At a *K* of 0.33, no or only very low circumferential stresses are present in the crown and hence no or very little resisting forces, acting against block failure, are mobilized on the sliding planes (Yeung & Leong, 1997, Pötsch, 2002). Furthermore, once, the shear resistance of the sliding planes is exceeded in the roof section, detaching blocks directly fall down, due to gravity. On the contrary, a higher friction angle on the sliding planes mobilizes also higher resisting forces and counteracts DCF in the tunnel face, where the failure mechanism is block sliding, rather than falling.

The best correspondence of the modelled and the actual excavation profile, apparent only in the left and mid-region of the roof section, as well as the improving match between the DSM with the numerical excavation profile is achieved with decreasing friction angles. This suggests that the used friction and/or dilation angles are still higher than in reality. Furthermore, the huge overbreak in the right crown section and right side wall, apparent in the DSM, is not reconstructed in the numerical analyses at all. This is due to the fact that the DSM features some holes in this region (Figure 3.2) and hence the joint network is not captured completely by neither the JTD nor JPD. As a consequence, blocks in this region are formed, but they lack kinematical freedom.

4.3.3 Case Study II

The simulations showed clearly that the documented and modelled excavation profiles have a good correspondence. Table 4.9 compares the quality of the approximation of the real excavation profile with the numerical analyses, based on visual inspection and depending on K as well as φ in the excavation sequences SSS-3 and SSS-4. The quality is given with “-“ for a poor correspondence, “o” for a moderate and “+” for a good correspondence. A poor correspondence is assigned in cases, where many numerical blocks overlay the DSM. The better the DSM is visible in the numerical model, the better is consequently the approximation. The table shows that the real excavation profile was reconstructed generally moderately to well. Only at $K = 0.66$, the performances especially in SSS-3 was poor, compared to the results from $K = 0.33$ or 1. Furthermore, in all cases, a lower friction angle resulted in a better visibility and hence approximation of the DSM. This fact is supported by the values, given in Table 3.20, where a higher $\Sigma V_{B,0.01}$ is generally reached at a lower φ. The comparison also leads to the conclusion, that kinematically free blocks experience a lower lateral confinement at a lower K-value, but seem to be squeezed out at $K = 1$. The single excavation sequences are discussed in detail in the following paragraphs.

Table 4.9: Comparison of the computed excavation profile with the DSM in SSS-3 and SSS-4 with variations in φ and K in Case Study II; poor correspondences are marked with “-“, moderate correspondences with “o” and well correspondences with “+”.

K	Variation of φ	Excavation Sequence	
		SSS-3	SSS-4
0.33	$\varphi + 5°$	o	-
	φ	o	o
	$\varphi - 5°$	o	+
0.66	$\varphi + 5°$	-	-
	φ	-	o
	$\varphi - 5°$	+	+
1	$\varphi + 5°$	-	-
	φ	o	o
	$\varphi - 5°$	+	+

As shown in Figure 3.21 and Table 3.20, there are minor block movements in excavation sequence 1, although the excavation has not yet reached the actual station of interest and the region, where the rock mass is jointed due to the DFN. This can be explained by the detachment of small blocks due to the model generation. The tunnel is generated as radial cracks, beginning from the tunnel centre, spreading towards the outer model boundaries and stopping at the next block boundary from the densification process. Furthermore, the trend of the tunnel is 150° and the model is not symmetrical anymore. Hence, many artificial cracks and blocks exist even before the actual introduction of the DFN and the blocks moving in excavation sequence 1 (especially at low circumferential stresses around the excavation) are obviously caused by these cracks, rather than the DFN. However, their influence, since it is constant throughout all excavation sequences and due to the low volumes, can be neglected.

In excavation sequence 2, the first discrete fractures are exposed in the roof section causing minor block movements on the right side (Figure 4.4). The detachments occur particularly in the upper, right side wall and subordinated from the tunnel face. Such behaviour was also observed during the geological documentation. In case of $K = 0.66$ and 1, these blocks are confined and show almost no movement in the case of φ and $\varphi + 5°$. But once the friction angle is low enough ($\varphi - 5°$), these blocks detach. Paradoxically, $\Sigma V_{B,0.01}$ also increases with an increasing K.

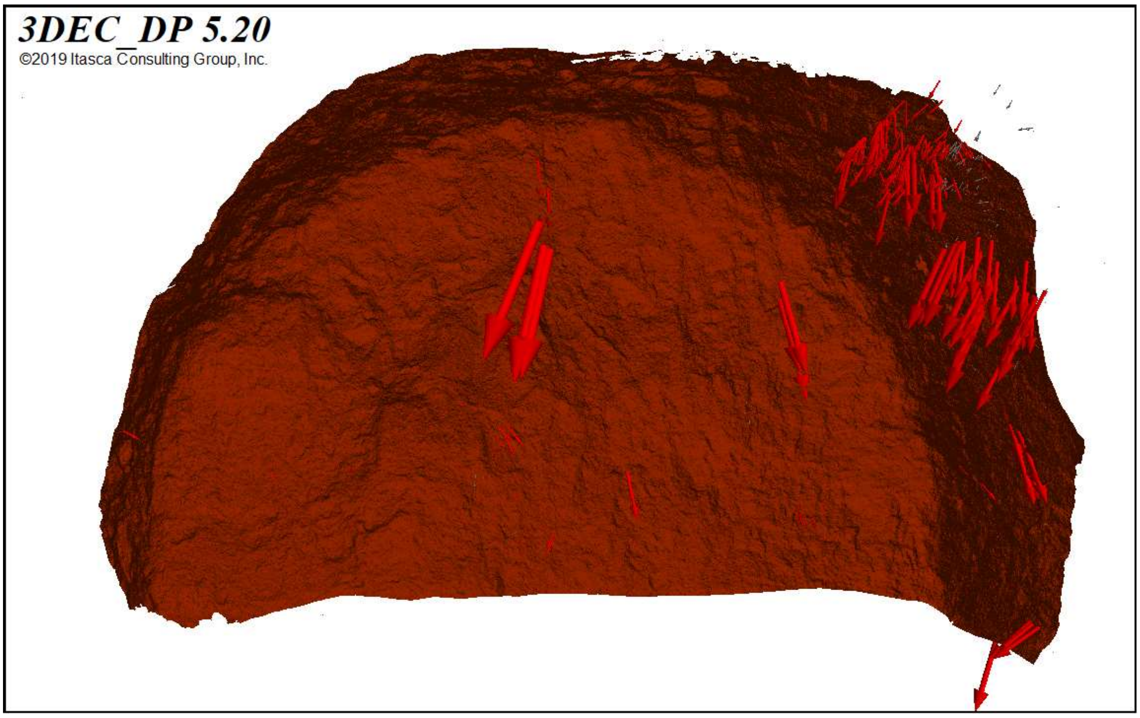

Figure 4.4: Location of detaching blocks in excavation sequence 2 ($\varphi - 5°$, $K = 1$); the red arrows indicate the direction and magnitude of movement of blocks, moving more than 1 cm; the grey arrows indicate movements less than 1 cm; the DSM is displayed in brown.

This increasing total volume of moving blocks as well as its locations is on the one hand explained by the existence and intersection of discrete fractures at this particular position and on the other hand probably due to the increased horizontal stresses, resulting in larger radial displacements. It appears that the blocks are squeezed into the opening at higher K-values. Especially at $K = 1$ and $\varphi - 5°$, the effect becomes obvious and can be observed throughout all different excavation stages. At $K = 0.33$ the effect is not observed at all.

Under low K, the block weight is predominantly controlling the block stability, whereas at higher K, the stress levels are increased on the block faces and the shear resistance as well as the joint dilation properties and rock mass stiffness are controlling the failure behaviour (Yeung & Leong, 1997, Sofianos et al., 1999, Pötsch, 2002). However, this effect is not observed in the calculations. With $K = 1$, $\Sigma V_{B,0.01}$ is much higher in SSS-4, than at a lower K, which contradicts the prior theorem. The effect is less obvious at higher friction angles and in SSS-3, but can still be anticipated. This is explained by the fact that in SSS-3, the block movement consists on the one hand of block sliding in the tunnel face as well as from the lower side walls. In SSS-4 all blocks assigned to SSS-3 are deleted and the remaining blocks in the tunnel periphery are kinematically free. Since block sliding is only subordinated, the influence of K on the block stability gains consequently in importance. Regarding the block geometry, it can be stated that blocks with an orientation almost perpendicular to the direction of loading are more stable than blocks with a subparallel orientation. Furthermore, the shear resistance is increased with the flatness-index (α, eq. 2.15): the higher the surface region of a block, the more shear resistance can be mobilized. In conclusion, elongated blocks, with a majority of block faces oriented subparallel to the direction of loading are more stable than cubic shaped blocks. This theory is supported by Pötsch (2002), who describes a higher stability of slender blocks (lower intersection angle) than compact blocks (higher intersection angle) under different circumferential stress conditions around the excavation.

The effect is depicted in Figure 4.5, where two cases with different blocks in 2D are shown. Case 1 displays a slender block with an intersection angle (γ) between the two planes of 30°. In Case 2, the angle γ is 60° and the block is less slender with a tendency to a cubic shape. In both cases, the unit weight of the blocks is equal and a joint friction angle of 25° acts on the joint planes. For simplicity reasons, only one contact plane of the block is considered. In case 1, the factor of safety (FOS) equals to 1 since the driving and the resisting forces are equal. In case 2 however, the FOS is lower than 1 and the block is not stable. This is only caused by the intersection angle and block geometry respectively. The direction of the resulting driving and resulting resisting forces indicates that the less slender block is also squeezed out of the rock mass. This effect is enhanced by increased tangential forces acting on the joint planes (higher K) and not existent at $K \leq 0.33$.

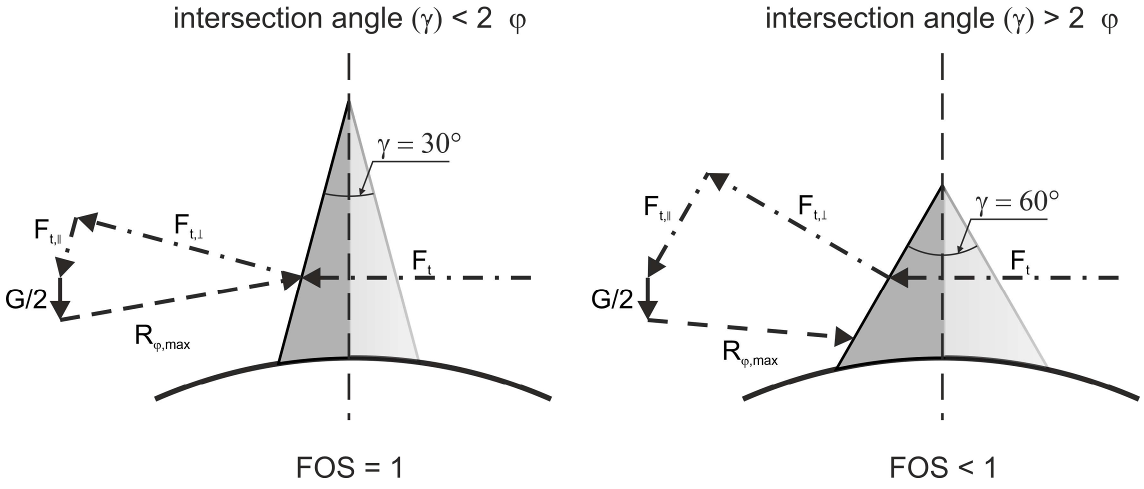

Figure 4.5: Exemplary investigation on the influence of the intersection angle (γ) of two joints forming a block subject to a tangential force; the unit weight (G) and tangential forces (F_t, dashed-dotted line) are equal for both cases, the joint friction angle (φ) equalt to 25° and not cohesion is acting on the joint planes; the power triangle are shown only for one joint plane, therefore $G/2$ is applied (solid line), the maximum mobilized shear resistance due to the joint friction ($R_{\varphi,\max}$) is shown in a dashed line.

Regarding Case Study II, Figure 3.20 displays that the dominant block form of the rock mass is platy and the block orientation is subparallel to the foliation, the joint planes, forming kinematically free blocks usually intersect at an angle between 80 and 90° (JS2∩JS3 and JS2∩JS5), which is higher than twice the applied joint friction angles on the joint planes (64° and 76°). In consequence, a lower resisting force can be mobilized on the joint planes. Simultaneously, the driving forces are increased due to the increased K. Hence, even at a higher K the mobilized shear resistance on the block faces is not high enough to counteract both the gravitational failure or the increased shear force on the joint planes and the blocks are generally less stable. The less slender block cannot be stabilized by the tangential force but is squeezed out of the rock mass.

5 Summary, Contributions and Future Research

5.1 Summary

In section 1.4 it was stated that answers to the research questions will be given in the summary. The questions are repeated here, followed by the answers found with this thesis. The primary goal of this thesis was to develop applications, which improve design strategies and increase the cost efficiency of rock engineering projects. As demonstrated in subsection 1.3.1, this is on the one hand achieved by an improved data acquisition by means of the geometrical joint network properties, an issue addressed by the research questions 1 to 3, and on the other hand by improved and more realistic numerical analyses. The benefits of using digital joint mapping directly in numerical simulations to assess the tunnel stability is addressed in research question 4. In short, with a well-known joint network and block geometry, tunnel support can be installed more specifically and adapted to the on-sight conditions. Prognoses for the pending round lengths can be improved, based on an early detection of a changing joint network pattern, or large discontinuities. This also helps in the adaption of the necessary tunnel support and increases the safety for the staff and equipment.

1. *Can the degree of detail of rock mass characterization be improved by using automated and computer aided characterization tools like JPD and JTD?*

As described in chapter 1, there is a lack in gathering enough objective data for an encompassing description of the joint network and rock mass structure. This leads to the necessity of generating statistical representations of the rock mass structure, which can seldom represent the actual situation on-site and hence will hardly allow a realistic analysis of the block stability. With the new methodology developed as part of this work and presented in chapter 2, a consistent way is shown, which can lead to a better understanding of the rock mass and a better design strategy with short term adaptions to the on-site conditions. By the combination of two very powerful tools for detecting both joint traces and joint planes, the joint network can be mapped as detailed as possible. This combination was recommended by several authors but has not been done before. The combination of the two information sources made use of their strengths and reduced their weaknesses. The mapping process runs semi-automatically with the well-known JPD and is fully automatized for the JTD. Subsequently, a highly realistic reconstruction of the in-situ joint network geometry in 3DEC was possible, due to the proposed application of using an explicit DFN rather than a statistical implementation of the joint set properties. The application of the DFN, which is not based on any probabilistic set characteristics, was only possible due to the extreme level of detail achieved by the applied combination of JTD with JPD. In addition, the information is directly implemented in a numerical representation of the rock mass, allowing the determination of its geometrical characteristics as well as site specific block stability analyses and the back calculation of material and joint properties.

The number of measurements for assessing the joint network geometries is extremely high and can never be reached by manual techniques (within the same time). This means that the derived statistical information from the mapping results are also very accurate, even if the (semi-)automatic approach is density based and still includes false positives. In both case studies, the documented joint sets were found and could be extended by further structure sets increasing the degree of detail. In Case Study I – the blocky rock mass – the joint plane detection algorithm worked particularly well and led to the detection of almost all relevant structure sets. By expanding the measurements by the detection of joint traces by the JTD, the results became even more representative, since features, which were not present as distinct joint planes or underrepresented in the results from the JPD were also detected. In Case Study II – the foliated rock mass – the JTD acquired precise measurements on the orientation and deviation of the foliation, which is most important for the general excavation profile. By only applying vector-based point cloud analyses, this joint set would have been disregarded as a distinct joint set, since the density cluster of the point normal vectors is superimposed by the very high number of point normal vectors, assigned to the tunnel face. Hence, by combining JTD and JPD, the degree of detail of mapping results is increased significantly and allows the analyses of not only very blocky rock masses, but also foliated and less blocky outcrops. This very accurate description of the joint network geometry also allowed a very precise determination of the block size and shape distributions, as well as the determination of the dominant block orientations in the rock mass. All three properties are necessary to understand the rock mass behaviour and the load distributions, which can lead to a mechanical stabilization or destabilization of kinematically free blocks. By using the proposed method of Kalenchuk et al. (2006), an objective and highly robust approach was used for describing the block shapes. The block sizes were directly drawn from 3DEC and no analytical approximations were necessary. The block orientations are given as the trend and plunge values of the longest inter-vertex chord per block.

2. *Can a value for the joint size be derived from the spatial information of the mapped joint sets?*

As written in section 1 and explained in sub-section 1.3.3, the persistence or joint size is a crucial parameter in analysing a jointed rock mass. An overestimation of the persistence leads to an excessive fracturing of the rock mass, leading to too small block sizes and a higher instability, whereas an underestimation of the persistence leads to an overestimation of the rock mass stability and block size distribution. By using discrete fractures, assigned with a set specific size, it is possible to avoid rough estimations of the joint set persistence. The approach makes use of the high quantity of measurements in one structure set and allows to a) parametrize the size distributions in analytical terms and b) get a statistical distribution of the joint sizes within one orientation cluster. This is by far a better approximation of the real joint size distribution, than by estimating a rather fictive persistence value or by simply using the apparent joint trace length as a reference size. In consequence, the better the approximation of the real joint size, the better is the resulting characterization of the rock mass geometry.

3. *Does the application of a DFN in block stability analyses result in a good reconstruction of the real excavation shape?*

Modelling the jointed rock masses by using a DFN resulted in both case studies in a very good approximation of the real tunnel shape with the given input parameters and computation steps. Especially the localization of the detaching blocks was in very good accordance with the tunnel documentation, this would not have been possible with a statistical rock mass model. In addition, the number of computation steps was rather low, to reach the desired block failures and capture the general trend within the single excavation sequences, since the number of movable blocks in the model was also rather low, compared to a fully jointed rock mass model as it would have been with a statistical representation of the joint network geometry.

4. *Which mechanical factors influence over-excavation in the investigated rock masses?*

It has been shown in sub-section 4.3.3 that especially the joint friction angle and the ratio between σ_1 and σ_3 are controlling the block stability in the investigated tunnel sections. This result was already confirmed by previous researchers (e.g. Yeung & Leong, 1997, Sofianos et al., 1999, Pötsch, 2002). However, the performed sensitivity analyses showed that it is possible to approximate the real shear strength properties as well as the secondary stress conditions, which led to the particular excavation shape in Case Study II. Although the performed analyses were restricted in several ways, like only rigid body movements, no intact rock bridges, or fixed joint stiffnesses, the possibilities could be demonstrated. It could also be shown that the block stability is also susceptible to the block shape, which highlights the necessity of determining this parameter during the design and excavation process as well. The numerical results also showed, that in case of excavation sequence 3, when blocks can slide from the tunnel face, the system stability is more sensitive to the joint friction angle, than *K*. However, once the station of interest is excavated and blocks only detach from the roof and side walls, the secondary stress conditions gain influence on the block stability.

5. *What limitations and uncertainties remain, where the operator must have the possibility to interfere with the results?*

The applied methods work well and are consistent but still not flawless. While identifying joint traces, also chisel traces and shadow borders were detected and although these false positives did not influence the resulting set clusters, they are still part of the DFN and hence can contribute to misinterpretation. In addition, the obtained results are heavily depending on the densities of either a frequently occurring 2D joint trace orientation, which results in the definition of an orientation cluster, or in a frequently occurring point normal orientation, which leads to the detection of a joint plane. By this, only the dominant structures can be detected and features, like the fault zones in Case Study II are missed, although their influence on the tunnel stability can be significant. Also, the incomplete segment linking process biases the true joint size distribution and thus influences the block stability analyses to a major extent. Such cases need the interference of an expert. Such an expert can for example deselect false positives and pre-define the orientations of geotechnically relevant structures, which can subsequently be used for the seeding points of an initial orientation clustering. In cases of incomplete segment linkages, a user can also interfere and manually post-process the structure maps by linking the segments according their geological-geotechnical properties. At this stage, the applied method for mapping the joint network can be used to support the mapping geologist in documentation and by increasing the reliability of the mapping results. However, the results always need to be controlled and counterchecked with the on-site measurements and geological model in order to avoid a false sense of security. Nonetheless, the benefit of implementing the mapping results directly in a 3DEC model cannot be denied.

5.2 Contributions

This thesis contributes to an improved design and risk assessment in tunnelling by the application of digital characterization methods and numerical stability analyses. The significant contributions are as follows:

- The applied methodology represents a consistent way for mapping the joint network, assessing the rock mass geometry and running deterministic stability analyses in rock engineering.

- The joint network is mapped automatically and the mapping results have an extreme level of detail, exceeding manual mapping results by far in precision, statistical reliability and quantity (section 2.1, sub-sections 3.1.1 and 3.2.1).

- The pixel-based joint trace detection, proposed by this thesis (sub-section 2.1.1), leads to a valuable increase of the level of detail.

- By combining 3D point cloud analyses with 2D image processing, the field of application for semi-automated joint network characterization is expanded also to non-blocky and foliated rock masses (e.g. Case Study II, section 3.2).

- A novel way is proposed to compute a particular joint size, rather than an imprecise and subjective estimation of this value (sub-section 2.1.4).

- Due to the high quality and quantity of the mapping results, the rock mass could be reconstructed realistically by generating a deterministic DFN (sub-section 2.3.2).

- The research demonstrated the influence of the joint friction angle and *K* on the block stability and highlighted the necessity of determining the site-specific rock mass geometry.

In addition, the following contributions support the applied methodology.

- An orientation dependent correlation filtering, which is proposed in sub-section 2.1.1, helps identifying dominant joint trace orientations.

- Using a two-staged segment linking process, results in a very good detection of joint traces (sub-sections 2.1.1, 3.1.1 and 3.2.1).

- On short distances, the orientation dependent segment linking produces good linking results (sub-section 2.1.1).

- The grey distance transformation applicable to connect remote line segments (sub-section 2.1.1).

- As discussed in section 4.1, automated joint mapping techniques are able to capture the most important joint structures in a rock mass and can support geologists in collecting data.

- The methodology to describe the joint size (sub-section 2.1.4) uses the empirical probability distribution of the measured apparent joint trace lengths per set and approximates the curve by an analytical function.

- The set specific joint size distribution can be described by constants of a double-exponential function.
- The Block Shape Characterization Method, developed by Kalenchuk et al. (2006) could be expanded by using the KDE, to determine dominant and subordinated block shapes (sub-section 2.2.2).
- The dominant orientations of the longest inter-vertex chord lengths can now be given in trend and plunge (sub-section 2.2.2) and set into relation to the local stress field.
- With a deterministic reconstruction of the real rock mass, back calculations regarding the rock mass and joint properties are possible (sub-section 2.3.4).
- By back-calculating the rock mass and joint properties according to the excavation profile and numerical results, it is possible to specify the amount of overbreak in the investigated tunnel section.
- With known material properties, and the exact description of the joint network, short term predictions about the hazard and amount of overbreak in upcoming rounds can be made.
- It could be shown that not only mechanical properties control the block stability, but also the block shape.
- With a deterministic rock mass model, the exact position of block failures can be reconstructed and their volume estimated.
- By using a deterministic DFN, rather than a statistic rock mass model, the computation time was decreased whilst preserving the realistic ground behavior.

5.3 Future Research

The methodology to detect joint planes does not leave much room for improvement, but since it is heavily depending on the quality of the analysed point cloud, advances in the generation of the DSM would also lead to improved results in the JPD. Much more improvements can be expected in the detection of joint traces. Current research investigates the applicability of Deep Neuronal Networks to automatically detect cracks in concrete structures (Pauly et al., 2017), or to determine the geological strength index (Hong et al., 2017) or differentiate different lithological units using machine learning (Patel & Chatterjee, 2016). The results seem promising but the elaboration needs a solid and extensive ground truth on which any ML algorithm can learn. Maybe the proposed methodology can help in generating this ground truth and contribute to this future development in image processing.

So far, the mapping results were used to generate a site-specific discrete fracture network, applicable only on the joint network pattern at the SOI and its close vicinity. However, it should on the one hand be possible to extrapolate the joint set characteristics by determining the underlying statistical set properties and hence enable a prognosis of the joint structure further ahead. On the other hand, a continuous collection of data leads to an even better understanding of the general rock mass structure and improves the excavation design and on-site decision making.

If the computation time can be reduced, the proposed method could also be used for real-time key block analyses for a preliminary detection of critical joint intersections to enable a more targeted installation of support measures. This would also enable an adaptive installation of support measures like systematic spot bolting, since the exact location can be determined precisely and the estimation of the block volume and direction of movement of kinematically free blocks is improved. This includes an adaption of the bolt length, capacity and number.

The method can also help in providing a short-term prognosis for the forthcoming round lengths regarding joint intersections – if the joint sizes exceed the round length or if the collected data are used to compute a statistical and continuously updated DFN – and the necessary/optimum amount of explosives. Furthermore, a highly detailed structure map might help in the prediction of the fracture intensity ahead and around the tunnel project, which might allow conclusions about the tectonization of the surrounding rock mass and pending fault zones.

As mentioned in sub-section 4.2.2, no direct comparison of the IBSD, obtained by the application of a DFN and the block size distribution, obtained by conventional approaches like Palmström & Stille (2015), Cai et al. (2004) and Wang et al. (1991) has been performed, but it is assumed that the DFN based IBSD will be higher than the analytical solutions. Still, a prove is outstanding and future research can provide the evidence.

6 References

3GSM GmbH (Hg.) (2018): ShapeMetriX 3D. JMX Analyst. User Manual.

Aichinger, S. (2018): Determination of the Block Size and Shape Distribution in a Quarry by using Remote Sensing Techniques. Master Thesis. Graz University of Technology, Graz, Austria. Institute of Rock Mechanics and Tunnelling.

Assali, P., Grussenmeyer, P., Villemin, T., Pollet, N. & Viguier, F. (2014): Surveying and modeling of rock discontinuities by terrestrial laser scanning and photogrammetry: Semi-automatic approaches for linear outcrop inspection. In: *Journal of Structural Geology* 66, S. 102–114. DOI: 10.1016/j.jsg.2014.05.014.

Austrian Society for Geomechanics (2010): Guideline for the Geotechnical Design of Underground Structures with Conventional Excavation. 2.1. Aufl. Salzburg: Österreichische Gesellschaft für Geotechnik. Online verfügbar unter https://www.oegg.at/upload/Download/Downloads/Guideline_Geotechnical_Design_conv_2010_01.pdf.

Auzinger, T. (2015): Dreidimensionale Visualisierung und Stabilitätsanalyse von potentiell instabilen Blöcken mittels Fernerkundungsdaten am Beispiel Feldkofel, Kärnten. Master's Thesis. Graz University of Technology, Graz. Institute of Applied Geosciences.

Azarafza, M., Ghazifard, A., Akgün, H. & Asghari-Kaljahi, E. (2019): Development of a 2D and 3D computational algorithm for discontinuity structural geometry identification by artificial intelligence based on image processing Development of a 2D and 3D computational algorithm for discontinuitystructural geometry identification by artificial intelligence basedon image processing techniques. In: *Bull Eng Geol Environ* 78 (5), S. 3371–3383. DOI: 10.1007/s10064-018-1298-2.

Bandis, S. C. (1990): Scale effects in the strength and deformability of rocks and rock joints. In: António Pinto da Cunha (Hg.): Scale effects in rock masses. Proceedings of the First International Workshop on Scale Effects in Rock Masses, Loen, Norway, 7 - 8 June 1990. Rotterdam: Balkema, S. 59–76.

Barton, N., Lien, R. & Lunde, J. (1974): Engineering classification of rock masses for the design of tunnel support. In: *Rock Mechanics* 6 (4), S. 189–236. DOI: 10.1007/BF01239496.

Bieniawski, Z. T. (1973): Engineering classification of jointed rock masses. In: *Trans S. Afr. Inst. Civ.* 15 (12), 335-343.

Bolkas, D., Vazaios, I., Peidou, A. & Vlachopoulos, N. (2018): Detection of Rock Discontinuity Traces Using Terrestrial LiDAR Data and Space-Frequency Transforms. In: *Geotech Geol Eng* 36 (3), S. 1745–1765. DOI: 10.1007/s10706-017-0430-6.

Bonilla-Sierra, V., Scholtès, L., Donzé, F. V. & Elmouttie, M. K. (2015): Rock slope stability analysis using photogrammetric data and DFN–DEM modelling. In: *Acta Geotech.* 10 (4), S. 497–511. DOI: 10.1007/s11440-015-0374-z.

Botev, Z. I., Grotowski, J. F. & Kroese, D. P. (2010): Kernel density estimation via diffusion. In: *Ann. Statist.* 38 (5), S. 2916–2957. DOI: 10.1214/10-AOS799.

Brady, Barry H. G.& Brown, Edwin T. (2006): Rock mechanics for underground mining. 3. ed., repr. with corr. Dordrecht: Springer. Online verfügbar unter http://www.bsz-bw.de/rekla/show.php?mode=source&eid=uni_0_12030170cov.

Buyer, A., Bongarz, R., Pischinger Gerald & Schubert, W. (2017): Neue Möglichkeiten der Gebirgscharakterisierung im Tunnelbau – Ein Beispiel vom Gleinalmtunnel. In: Deutsche Gesellschaft für Geotechnik e.V. (DGGT) (Hg.): FACHSEKTIONSTAGE GEOTECHNIK 2017. Congress Centrum Würzburg, 6.-8. September, S. 28–33.

Buyer, A., Pischinger, G. & Schubert, W. (2018): Image-based discontinuity identification. In: *Geomechanik Tunnelbau* 11 (6), S. 693–700. DOI: 10.1002/geot.201800047.

Buyer, A. & Schubert, W. (2017): Calculation the Spacing of Discontinuities from 3D Point Clouds. In: *Procedia Engineering* 191, S. 270–278. DOI: 10.1016/j.proeng.2017.05.181.

Buyer, A. & Schubert, W. (2018): Joint Trace Detection in Digital Images. In: ISRM International Symposium (Hg.): 10th Asian Rock Mechanics Symposium. 10th Asian Rock Mechanics Symposium The ISRM International Symposium for 2018. Singapore, 29.10. - 03.11.2018. International Society for Rock Mechanics.

Cai, M., Kaiser, P. K., Uno, H., Tasaka, Y. & Minami, M. (2004): Estimation of rock mass deformation modulus and strength of jointed hard rock masses using the GSI system. In: *International Journal of Rock Mechanics and Mining Sciences* 41 (1), S. 3–19. DOI: 10.1016/S1365-1609(03)00025-X.

Canny, J. (1986): A Computational Approach to Edge Detection. In: *IEEE Trans. Pattern Anal. Mach. Intell.* PAMI-8 (6), S. 679–698. DOI: 10.1109/TPAMI.1986.4767851.

Costamagna, E., Oggeri, C., Segarra, P., Castedo, R. & Navarro, J. (2018): Assessment of contour profile quality in D&B tunnelling. In: *Tunnelling and Underground Space Technology* 75, S. 67–80. DOI: 10.1016/j.tust.2018.02.007.

Dershowitz, W. S. & Einstein, H. H. (1988): Characterizing rock joint geometry with joint system models. In: *Rock Mechanics and Rock Engineering* 21 (1), S. 21–51. DOI: 10.1007/BF01019674.

Dershowitz, W. S. & Herda, H. H. (1992): Interpretation of fracture spacing and intensity. In: J. R. Tillerson (Hg.): Rock mechanics. Proceedings of the 33rd U.S. Symposium, Sweeney Convention Center, Santa Fe, New Mexico 3 - 5 June 1992, Bd. 1. Rotterdam: Balkema, S. 757–766.

Dershowitz, W. S., La Pointe, P. R. & Doe, T. W. (2004): Advances in discrete fracture network modeling. In: National Ground Water Association (Hg.): Proceedings of the US EPA/NGWA fractured rock conference. Portland, Maine: National Ground Water Association, S. 882–894.

Dewez, T. B.J., Girardeau-Montaut, D., Allanic, C. & Rohmer, J. (2016): FACETS. A CLOUDCOMPARE PLUGIN TO EXTRACT GEOLOGICAL PLANES FROM UNSTRUCTURED 3D POINT CLOUDS. In: International Society of Photogrammetry and Remote Sensing (ISPRS) (Hg.): The International Archives of the Photogrammetry, Remote Sensing and Spatial Information Sciences, XLI-B5. XXIII ISPRS Congress. Prague, Czech Republic, 12-19.07.2016. International Society of Photogrammetry and Remote Sensing (ISPRS) (XLI-B5), S. 799–804.

Elmo, D., Donati, D. & Stead, D. (2018): Challenges in the characterisation of intact rock bridges in rock slopes. In: *Engineering Geology* 245, S. 81–96. DOI: 10.1016/j.enggeo.2018.06.014.

Elmo, D., Rogers, S., Stead, D. & Eberhardt, E. (2014): Discrete Fracture Network approach to characterise rock mass fragmentation and implications for geomechanical upscaling. In: *Mining Technology* 123 (3), S. 149–161. DOI: 10.1179/1743286314Y.0000000064.

Elmo, D. & Stead, D. (2010): An Integrated Numerical Modelling–Discrete Fracture Network Approach Applied to the Characterisation of Rock Mass Strength of Naturally Fractured Pillars. In: *Rock Mech Rock Eng* 43 (1), S. 3–19. DOI: 10.1007/s00603-009-0027-3.

Elmo, D., Stead, D. & Rogers, S. (2015): Guidelines for the quantitative description of discontinuities for use in discrete fracture network modelling. In: International Society for Rock Mechanics (Hg.): Proceedings of the 13th International Congress of Rock Mechanics. Innovations in Applied and Theoretical Rock Mechanics. Montreal, Canada, May 10-13. International Society for Rock Mechanics.

Elmouttie, M. K. & Poropat, G. V. (2012): A Method to Estimate In Situ Block Size Distribution. In: *Rock Mech Rock Eng* 45 (3), S. 401–407. DOI: 10.1007/s00603-011-0175-0.

Ester, M., Kriegel, H. P., Sander, J. & Xu, X. (1996): A density-based algorithm for discovering clusters in large spatial databases with noise. In: KDD (Hg.): Kdd Proceedings, 96 No. 34, S. 226–231.

Fasching, A. (2000): Improvement of Acquisition Methods for Geotechnical Data. Doctoral Thesis. Graz University of Technology, Graz. Institute of Rock Mechanics and Tunnelling.

Fekete, S. & Diederichs, M. (2013): Integration of three-dimensional laser scanning with discontinuum modelling for stability analysis of tunnels in blocky rockmasses. In: *International Journal of Rock Mechanics and Mining Sciences* 57, S. 11–23. DOI: 10.1016/j.ijrmms.2012.08.003.

Fekete, S., Diederichs, M. & Lato, M. (2010): Geotechnical and operational applications for 3-dimensional laser scanning in drill and blast tunnels. In: *Tunnelling and Underground Space Technology* 25 (5), S. 614–628. DOI: 10.1016/j.tust.2010.04.008.

Francioni, M., Salvini, R., Stead, D. & Coggan, J. (2018): Improvements in the integration of remote sensing and rock slope modelling. In: *Nat Hazards* 90 (2), S. 975–1004. DOI: 10.1007/s11069-017-3116-8.

Franklin, J. A., Maerz, N. H. & Bennett, C. P. (1988): Rock mass characterization using photoanalysis. In: *International Journal of Mining and Geological Engineering* 6 (2), S. 97–112. DOI: 10.1007/BF00880801.

Gaich, A. & Pischinger, G. (2016): 3D images for digital geological mapping. In: *Geomechanik Tunnelbau* 9 (1), S. 45–51. DOI: 10.1002/geot.201500048.

Gaich, A., Poetsch, M., Fasching, A. & Schubert, W. (2004a): Measurement of Rock Mass Parameters based on 3D Imaging. In: G. Barla und M. (eds) Barla (Hg.): Patron editore (MIR), S. 21–45.

Gaich, A. & Pötsch, M. (2011): Böschungsbewertung mit 3D-Bildern. In: *Berg Huettenmaenn Monatsh* 156 (2), S. 47–52. DOI: 10.1007/s00501-011-0626-7.

Gaich, A., Pötsch, M., Fasching, A. & Schubert, W. (2004b): Contact-free measurement of rock mass structures using the jointmetriX3D system. In: *International Journal of Rock Mechanics and Mining Sciences* 41, S. 304–309. DOI: 10.1016/j.ijrmms.2004.03.058.

Gaich, A., Pötsch, M. & Schubert, W. (2006): Basics and application of 3D imaging systems with conventional and high-resolution cameras. In: Fulvio Tonon und Joseph T. Kottenstette (Hg.): Laser and Photogrammetric Methods for Rock Face Characterisation. Report on a Workshop Held in Golden. Colorado, S. 33–48.

Gaich, A., Pötsch, M. & Schubert, W. (2014): Extended rock mass characterization from 3D images. In: Alejano, Perucho, Olalla, Jimenez (Hg.): CRC Press: London, 138 (Abstract); paper: USB storage.

Gaich, A., Pötsch, M. & Schubert, W. (2017): Digital rock mass characterization 2017 - Where are we now? What comes next? In: *Geomechanik Tunnelbau* 10 (5), S. 561–566. DOI: 10.1002/geot.201700036.

Gaich, A., Schubert, W. & Pötsch, M. (2004c): Reproducible rock mass description in 3D using JointMetriX3D system. In: *Proc. of the ISRM Regional Symposium Eurock 2004 & 53rd Geomechanics Colloquy*, S. 61–64.

Geoconsult ZT GmbH (Hg.) (2015): A9 Pyhrn Autobahn, Vollausbau Gleinalmtunnel, Geologische Tunneldokumentation, abfalltechnische Beurteilung und wasserwirtschaftliche Beweissicherung, Geologische Tunneldokumentation: Schlussbericht. Geoconsult ZT GmbH. Salzburg, Austria.

ÖNORM EN ISO 14689 (2018): Geotechnische Erkundung und Untersuchung - Benennung, Beschreibung und Klassifizierung von Fels (ISO 14689:2017).

Gonzalez, Rafael C.& Woods, Richard E. (2018): Digital Image Processing. 4th ed. Edinburgh (England): Pearson Educated Limited.

Goodman, R. E. (1995): Block theory and its application. In: *Géotechnique* 45 (3), S. 383–423. DOI: 10.1680/geot.1995.45.3.383.

Goodman, Richard E.& Shi, Gen-hua (1985): Block Theory and its application to rock engineering. Englewood Cliffs: Prentice-Hall (Prentice-Hall international series in civil engineering and engineering mechanics).

Goricki, A. (2003): Classification of Rock Mass Behaviour based on a Hierarchical Rock Mass Characterization for the Design of Underground Structures. Doctoral Thesis. Graz University of Technology, Graz. Institute of Rock Mechanics and Tunnelling.

Goricki, A. & Goodman, R. (2003): Failure Modes of Rock Slopes Demonstrated with Base Friction and Simple Numerical Models. In: *Felsbau* 21 (2), S. 25–30.

Gottsbacher, L. (2017): Calculation of the Young's Modulus for Rock Masses with 3DEC and comparing it with empirical methods. Master Thesis. Graz University of Technology, Graz, Austria. Institute of Rock Mechanics and Tunnelling.

Grenon, M., Landry, A., Hadjigeorgiou, J. & Lajoie, P. L. (2017): Discrete fracture network based drift stability at the Éléonore mine. In: *Mining Technology* 126 (1), S. 22–33. DOI: 10.1080/14749009.2016.1199296.

Hammah, R. E. & Curran, J. H. (1998): Fuzzy cluster algorithm for the automatic identification of joint sets. In: *International Journal of Rock Mechanics and Mining Sciences* 35 (7), S. 889–905. DOI: 10.1016/S0148-9062(98)00011-4.

Haneberg, W. (2007): Directional roughness profiles from three-dimensional photogrammetric or laser scanner point clouds. In: Erik Eberhardt (Hg.): Rock Mechanics. Proceedings of the 1st Canada-US Rock Mechanics Symposium, Vancouver, Canada, 27-31 May 2007. Hoboken: CRC Press, S. 101–106.

Haneberg, W. C. (2008): Using close range terrestrial digital photogrammetry for 3-D rock slope modeling and discontinuity mapping in the United States. In: *Bull Eng Geol Environ* 67 (4), S. 457–469. DOI: 10.1007/s10064-008-0157-y.

Havaej, M., Coggan, J., Stead, D. & Elmo, D. (2016): A Combined Remote Sensing–Numerical Modelling Approach to the Stability Analysis of Delabole Slate Quarry, Cornwall, UK. In: *Rock Mech Rock Eng* 49 (4), S. 1227–1245. DOI: 10.1007/s00603-015-0805-z.

He, S., Li, Y. & Aydin, A. (2018): A comparative study of UDEC simulations of an unsupported rock tunnel. In: *Tunnelling and Underground Space Technology* 72, S. 242–249. DOI: 10.1016/j.tust.2017.11.031.

Hoek, Evert& Brown, Edwin T. (1994): Underground excavations in rock. Reprinted. London: Spon.

Hoek, Evert, Kaiser, P. K.& Bawden, W. F. (1997): Support of underground excavations in hard rock. 2. print. Rotterdam: Balkema.

Hong, K., Han, E. & Kang, K. (2017): Determination of geological strength index of jointed rock mass based on image processing. In: *Journal of Rock Mechanics and Geotechnical Engineering* 9 (4), S. 702–708. DOI: 10.1016/j.jrmge.2017.05.001.

Huang, J.-Z., Feng, X.-T., Zhou, Y.-Y. & Yang, C.-X. (2019): Stability analysis of deep-buried hard rock underground laboratories based on stereophotogrammetry and discontinuity identification. In: *Bull Eng Geol Environ* 78 (7), S. 5195–5217. DOI: 10.1007/s10064-019-01461-x.

Hudson, John A.& Harrison, John P. (2009): Engineering rock mechanics. An Introduction to the Principles. Amsterdam: Pergamon.

ISRM (1978): Suggested methods for the quantitative description of discontinuities in rock masses. In: *International Journal of Rock Mechanics and Mining Sciences & Geomechanics Abstracts* 15 (6), S. 319–368. DOI: 10.1016/0148-9062(78)91472-9.

Jing, L. (2003): A review of techniques, advances and outstanding issues in numerical modelling for rock mechanics and rock engineering. In: *International Journal of Rock Mechanics and Mining Sciences* 40 (3), S. 283–353. DOI: 10.1016/S1365-1609(03)00013-3.

Kalenchuk, K. S., Diederichs, M. S. & McKinnon, S. (2006): Characterizing block geometry in jointed rockmasses. In: *International Journal of Rock Mechanics and Mining Sciences* 43 (8), S. 1212–1225. DOI: 10.1016/j.ijrmms.2006.04.004.

Kalenchuk, K. S., McKinnon, S. & Diederichs, M. S. (2008): Block geometry and rockmass characterization for prediction of dilution potential into sub-level cave mine voids. In: *International Journal of Rock Mechanics and Mining Sciences* 45 (6), S. 929–940. DOI: 10.1016/j.ijrmms.2007.10.006.

Kemeny, J. & Post, R. (2003): Estimating three-dimensional rock discontinuity orientation from digital images of fracture traces. In: *Computers & Geosciences* 29 (1), S. 65–77. DOI: 10.1016/S0098-3004(02)00106-1.

Kim, B. H., Cai, M., Kaiser, P. K. & Yang, H. S. (2007): Estimation of Block Sizes for Rock Masses with Non-persistent Joints. In: *Rock Mech. Rock Engng.* 40 (2), S. 169–192. DOI: 10.1007/s00603-006-0093-8.

Kim, B.-H., Peterson, R. L., Katsaga, T. & Pierce, M. E. (2015): Estimation of rock block size distribution for determination of Geological Strength Index (GSI) using discrete fracture networks (DFNs). In: *Mining Technology* 124 (3), S. 203–211. DOI: 10.1179/1743286315Y.0000000015.

Kluckner, A., Söllner, P., Schubert, W. & Pötsch, M. (2015): Estimation of the in situ block size in jointed rock masses using three-dimensional block simulations and discontinuity measurements. In: International Society for Rock Mechanics (Hg.): Proceedings of the 13th International Congress of Rock Mechanics. Innovations in Applied and Theoretical Rock Mechanics. Montreal, Canada, May 10-13. International Society for Rock Mechanics.

Kulatilake, P. H. & Wu, T. H. (1984): Estimation of mean trace length of discontinuities. In: *Rock Mechanics and Rock Engineering* 17 (4), S. 215–232.

Kulatilake, P.H.S.W., Wang, S. & Stephansson, O. (1993): Effect of finite size joints on the deformability of jointed rock in three dimensions. In: *International Journal of Rock Mechanics and Mining Sciences & Geomechanics Abstracts* 30 (5), S. 479–501. DOI: 10.1016/0148-9062(93)92216-D.

Lambert, C. & Coll, C. (2014): Discrete modeling of rock joints with a smooth-joint contact model. In: *Journal of Rock Mechanics and Geotechnical Engineering* 6 (1), S. 1–12. DOI: 10.1016/j.jrmge.2013.12.003.

Lemy, F. & Hadjigeorgiou, J. (2003): Discontinuity trace map construction using photographs of rock exposures. In: *International Journal of Rock Mechanics and Mining Sciences* 40 (6), S. 903–917. DOI: 10.1016/S1365-1609(03)00069-8.

Li, X., Chen, J. & Zhu, H. (2016): A new method for automated discontinuity trace mapping on rock mass 3D surface model. In: *Computers & Geosciences* 89, S. 118–131. DOI: 10.1016/j.cageo.2015.12.010.

Liu, Q. (2013): Remote sensing technologies in rock mass characterization. In: Xia-Ting Feng, John A. Hudson und Tan Fei (Hg.): Rock Characterisation, Modelling and Engineering Design Methods. Proceedings of the 3rd ISRM Sinorock Symposium. Shanghai, China, 18-20 June: CRC Press.

Lu, P. & Latham, J.-P. (1999): Developments in the Assessment of In-situ Block Size Distributions of Rock Masses. In: *Rock Mech Rock Eng* 32 (1), S. 29–49. DOI: 10.1007/s006030050042.

Maerz, N. H., Ibarra, J. A. & Franklin, J. A. (1996): Overbreak and underbreak in underground openings Part 1: measurement using the light sectioning method and digital image processing. In: *Geotech Geol Eng* 14 (4), S. 307–323. DOI: 10.1007/BF00421946.

Mahtab, M. A., Rossler, K., Kalamaras, G. S. & Grasso, P. (1997): Assessment of geological overbreak for tunnel design and contractual claims. In: *International Journal of Rock Mechanics and Mining Sciences* 34 (3-4), S. 185. DOI: 10.1016/S1365-1609(97)00086-5.

Mandal, S. K. & Singh, M. M. (2009): Evaluating extent and causes of overbreak in tunnels. In: *Tunnelling and Underground Space Technology* 24 (1), S. 22–36. DOI: 10.1016/j.tust.2008.01.007.

MAPAG Materialprüfung G.m.b.H (2015): Untersuchungsbericht. über Materialprüfungen aus Haupt- und Nebenproben für das BVH A9 Pyhrn Autobahn Vollausbau Gleinalmtunnel. Neubau 2. Röhre. Unter Mitarbeit von H. Gregori. Hg. v. MAPAG Materialprüfung G.m.b.H. MAPAG Materialprüfung G.m.b.H. Gumpoldskirchen.

Mas Ivars, D., Pierce, M. E., Darcel, C., Reyes-Montes, J., Potyondy, D. O., Paul Young, R. & Cundall, P. A. (2011): The synthetic rock mass approach for jointed rock mass modelling. In: *International Journal of Rock Mechanics and Mining Sciences* 48 (2), S. 219–244. DOI: 10.1016/j.ijrmms.2010.11.014.

Mauldon, M., Dunne, W. M. & Rohrbaugh, M. B. (2001): Circular scanlines and circular windows. New tools for characterizing the geometry of fracture traces. In: *Journal of Structural Geology* 23 (2-3), S. 247–258. DOI: 10.1016/S0191-8141(00)00094-8.

Menegoni, N., Giordan, D., Perotti, C. & Tannant, D. D. (2019): Detection and geometric characterization of rock mass discontinuities using a 3D high-resolution digital outcrop model generated from RPAS imagery – Ormea rock slope, Italy. In: *Engineering Geology* 252, S. 145–163. DOI: 10.1016/j.enggeo.2019.02.028.

Menéndez-Díaz, A., González-Palacio, C., Álvarez-Vigil, A. E., González-Nicieza, C. & Ramírez-Oyanguren, P. (2009): Analysis of tetrahedral and pentahedral key blocks in underground excavations. In: *Computers and Geotechnics* 36 (6), S. 1009–1023. DOI: 10.1016/j.compgeo.2009.03.013.

Miyoshi, T., Elmo, D. & Rogers, S. (2018): Influence of data analysis when exploiting DFN model representation in the application of rock mass classification systems. In: *Journal of Rock Mechanics and Geotechnical Engineering* 10 (6), S. 1046–1062. DOI: 10.1016/j.jrmge.2018.08.003.

Palmström, Arild (2001): Measurement and characterization of rock mass jointing.

Palmström, Arild& Stille, Håkan (2015): Rock engineering. 2 ed. London: ICE-Publ. a division of Thomas Telford Ltd.

Palmstrøm, A. (2005): Measurements of and correlations between block size and rock quality designation (RQD). In: *Tunnelling and Underground Space Technology* 20 (4), S. 362–377. DOI: 10.1016/j.tust.2005.01.005.

Patel, A. K. & Chatterjee, S. (2016): Computer vision-based limestone rock-type classification using probabilistic neural network. In: *Geoscience Frontiers* 7 (1), S. 53–60. DOI: 10.1016/j.gsf.2014.10.005.

Pauly, L., Peel, H., Luo, S., Hogg, D. & Fuentes, R. (2017): Deeper Networks for Pavement Crack Detection. In: International Association for Automation & Robotics in Construction (IAARC) (Hg.): 34th International Symposium on Automation and Robotics in Construction and Mining (ISARC 2017), Taipei, Taiwan, 28 June-1 July 2017. New York: Printed by Curran Associates, Inc.

Poropat, G. V. (2006): Remote 3D Mapping Of Rock Mass Structure. In: J. Kottenstette und F. Tonon (Hg.): Laser and Photogrammetric Methods for Rock Face Characterization. GoldenRocks 2006 - The 41st U.S. Rock Mechanics Symposium. Golden, Colorado, 17-18.06.2006. American Rock Mechanics Association. 1 Band, S. 63–75.

Pötsch, M. (2002): Influence of the three-dimensional stress condition at the tunnel face on the stability of removable blocks. Diploma Thesis. Graz University of Technology, Graz. Institute of Rock Mechanics and Tunnelling.

Pötsch, M. (2011): The analysis of rotational and sliding modes of failure for slopes, foundations, and underground structures in blocky, hard rock. Dissertation. Graz University of Technology, Austria. Institute for Rock Mechanics and Tunnelling.

Preiner, A. (2018): Characterization of the Joint Network Geometry and its Influence on the Excavation of the Gleinalmtunnel (2nd tube, Styria, Austria). Master's Thesis. Graz University of Technology, Graz. Institute of Rock Mechanics and Tunnelling.

Priest, S. D. (1980): The use of inclined hemisphere projection methods for the determination of kinematic feasibility, slide direction and volume of rock blocks. In: *International Journal of Rock Mechanics and Mining Sciences & Geomechanics Abstracts* 17 (1), S. 1–23. DOI: 10.1016/0148-9062(80)90002-9.

Priest, S. D. & Hudson, J. A. (1981): Estimation of discontinuity spacing and trace length using scanline surveys. In: *International Journal of Rock Mechanics and Mining Sciences & Geomechanics Abstracts* 18 (3), S. 183–197. DOI: 10.1016/0148-9062(81)90973-6.

Priest, Stephen D. (1993): Discontinuity analysis for Rock engineering. reprinted. [New York]: Springer-science + Business media, b.v.

Reid, T. R. & Harrison, J. P. (2000): A semi-automated methodology for discontinuity trace detection in digital images of rock mass exposures. In: *International Journal of Rock Mechanics and Mining Sciences* 37 (7), S. 1073–1089. DOI: 10.1016/S1365-1609(00)00041-1.

Riquelme, A., Tomás, R., Cano, M., Pastor, J. L. & Abellán, A. (2018): Automatic Mapping of Discontinuity Persistence on Rock Masses Using 3D Point Clouds. In: *Rock Mech Rock Eng* 8. DOI: 10.1007/s00603-018-1519-9.

Riquelme, A. J., Abellán, A. & Tomás, R. (2015): Discontinuity spacing analysis in rock masses using 3D point clouds. In: *Engineering Geology* 195, S. 185–195. DOI: 10.1016/j.enggeo.2015.06.009.

Riquelme, A. J., Abellán, A., Tomás, R. & Jaboyedoff, M. (2014): A new approach for semi-automatic rock mass joints recognition from 3D point clouds. In: *Computers & Geosciences* 68, S. 38–52. DOI: 10.1016/j.cageo.2014.03.014.

Scholtès, L. & Donzé, F.-V. (2012): Modelling progressive failure in fractured rock masses using a 3D discrete element method. In: *International Journal of Rock Mechanics and Mining Sciences* 52, S. 18–30. DOI: 10.1016/j.ijrmms.2012.02.009.

Shang, J., West, L. J., Hencher, S. R. & Zhao, Z. (2018): Geological discontinuity persistence. Implications and quantification. In: *Engineering Geology* 241, S. 41–54. DOI: 10.1016/j.enggeo.2018.05.010.

Slob, S. (2010): Automated rock mass characterization using 3-D terrestrial laser scanning. Dissertation. Technica University Delft, Delft.

Slob, S. & Hack, R. (2004): 3D Terrestrial Laser Scanning as a New Field Measurement and Monitoring Technique. In: S. Bhattacharji, H.J Neugebauer, J. Reitner, K. Stüwe, G.M Friedman, A. Seilacher et al. (Hg.): Engineering Geology for Infrastructure Planning in Europe, Bd. 104. Berlin, Heidelberg: Springer Berlin Heidelberg (Lecture Notes in Earth Sciences), S. 179–189.

Slob, S., Hack, R., Feng, Q., Röshoff, K. & Turner, A. K. (2007): Fracture mapping using 3D laser scanning techniques. In: L. Sousa, E. Ribeiro, Claudio Olalla und N. Grossmann (Hg.): 11th Congress of the International Society for Rock Mechanics. The second half century of rock mechanics : proceedings of the 11th Congress of the International Society for Rock Mechanics (ISRM 2007), Lisbon, Portugal, 9-13 July 2007. London: Taylor & Francis (Balkema-proceedings and monographs in engineering, water, and earth sciences), S. 299–302.

Sofianos, A.I., Nomikos, P. & Tsoutrelis, C.E. (1999): Stability of symmetric wedge formed in the roof of a circular tunnel: nonhydrostatic natural stress field. In: *International Journal of Rock Mechanics and Mining Sciences* 36 (5), S. 687–691. DOI: 10.1016/S0148-9062(99)00033-9.

Soille, P. (1994): Generalized geodesy via geodesic time. In: *Pattern Recognition Letters* 15 (12), S. 1235–1240. DOI: 10.1016/0167-8655(94)90113-9.

Söllner, P. (2014): Determination of the in situ Block Size Distribution as a Parameter for the Rock Mass Characterization based on Measurements and Statistical Methods. Master Thesis. Graz University of Technology, Graz. Institute of Rock Mechanics and Tunnelling.

Song, J.-J. & Lee, C.-I. (2001): Estimation of joint length distribution using window sampling. In: *International Journal of Rock Mechanics and Mining Sciences* 38 (4), S. 519–528. DOI: 10.1016/S1365-1609(01)00018-1.

Stavropoulou, M. (2014): Discontinuity frequency and block volume distribution in rock masses. In: *International Journal of Rock Mechanics and Mining Sciences* 65, S. 62–74. DOI: 10.1016/j.ijrmms.2013.11.003.

Steger, C. (1998): An unbiased detector of curvilinear structures. In: *IEEE Trans. Pattern Anal. Mach. Intell.* 20 (2), S. 113–125. DOI: 10.1109/34.659930.

Stille, H. & Palmstrøm, A. (2003): Classification as a tool in rock engineering. In: *Tunnelling and Underground Space Technology* 18 (4), S. 331–345. DOI: 10.1016/S0886-7798(02)00106-2.

Strouth, A. & Eberhardt, E. (2006): The use of LiDAR to overcome rock slope hazard data collection challenges at Afternoon Creek, Washington. In: American Rock Mechanics Association (Hg.): 41st US Rock Mechanics Symposium (Golden Rocks 2006): 50 Years of Rock Mechanics. Golden, Colorado, 17-21 June. American Rock Mechanics Association, ARMA06-993.

Sturzenegger, M. & Stead, D. (2009a): Close-range terrestrial digital photogrammetry and terrestrial laser scanning for discontinuity characterization on rock cuts. In: *Engineering Geology* 106 (3-4), S. 163–182. DOI: 10.1016/j.enggeo.2009.03.004.

Sturzenegger, M. & Stead, D. (2009b): Quantifying discontinuity orientation and persistence on high mountain rock slopes and large landslides using terrestrial remote sensing techniques. In: *Natural Hazards and Earth System Sciences* 9 (2), S. 267–287. DOI: 10.5194/nhess-9-267-2009.

Sturzenegger, M., Stead, D. & Elmo, D. (2011): Terrestrial remote sensing-based estimation of mean trace length, trace intensity and block size/shape. In: *Engineering Geology* 119 (3-4), S. 96–111. DOI: 10.1016/j.enggeo.2011.02.005.

Szeliski, Richard (2011): Computer vision. Algorithms and applications. London: Springer (Texts in computer science). Online verfügbar unter http://site.ebrary.com/lib/alltitles/docDetail.action?docID=10421311.

The Math Works Inc. (Hg.) (2016): Documentation.

Thiele, S. T., Grose, L., Samsu, A., Micklethwaite, S., Vollgger, S. A. & Cruden, A. R. (2017): Rapid, semi-automatic fracture and contact mapping for point clouds, images and geophysical data. In: *Solid Earth* 8 (6), S. 1241–1253. DOI: 10.5194/se-8-1241-2017.

Thuro, K. (2002): Geologisch-felsmechanische Grundlagen der Gebirgslösung im Tunnelbau. Hablilitationsschrift. Technical University Munich, München. Chair for Engineering Geology.

Tuckey, Z. & Stead, D. (2016): Improvements to field and remote sensing methods for mapping discontinuity persistence and intact rock bridges in rock slopes. In: *Engineering Geology* 208, S. 136–153. DOI: 10.1016/j.enggeo.2016.05.001.

ÖNORM B 2203-1 (2001): Untertagebauarbeiten - Werkvertragsnorm Teil 1: Zyklischer Vortrieb.

van Knapen, B. & Slob, S. (2006): Identification and characterisation of rock mass discontinuity sets using 3D laser scanning. In: *Pre-proceedings of the 10th International Congress IAEG: Engineering Geology for Tomorrow's Cities. Nottingham, United Kingdom* 438.

Vasuki, Y., Holden, E.-J., Kovesi, P. & Micklethwaite, S. (2014): Semi-automatic mapping of geological Structures using UAV-based photogrammetric data. An image analysis approach. In: *Computers & Geosciences* 69, S. 22–32. DOI: 10.1016/j.cageo.2014.04.012.

Vazaios, I., Farahmand, K., Vlachopoulos, N. & Diederichs, M. S. (2018): Effects of confinement on rock mass modulus. A synthetic rock mass modelling (SRM) study. In: *Journal of Rock Mechanics and Geotechnical Engineering* 10 (3), S. 436–456. DOI: 10.1016/j.jrmge.2018.01.002.

Wallbrecher, Eckard (1986): Tektonische und gefügeanalytische Arbeitsweisen. Graph., rechner. u. statist. Verfahren. Stuttgart: Enke.

Wang, H., Latham, J.-P. & Poole, A. B. (1991): Predictions of block size distribution for quarrying. In: *Quarterly Journal of Engineering Geology and Hydrogeology* 24 (1), S. 91–99. DOI: 10.1144/GSL.QJEG.1991.024.01.10.

Wang, L. G., Yamashita, S., Sugimoto, F., Pan, C. & Tan, G. (2003): A Methodology for Predicting the In Situ Size and Shape Distribution of Rock Blocks. In: *Rock Mechanics and Rock Engineering* 36 (2), S. 121–142. DOI: 10.1007/s00603-002-0039-8.

Wetzler, A. (2010): Bresenham optimized for Matlab. Hg. v. The Math Works Inc. File Exchange. Online verfügbar unter https://de.mathworks.com/matlabcentral/fileexchange/28190-bresenham-optimized-for-matlab, zuletzt geprüft am 12.02.2019.

Yeung, M. R. & Leong, L. L. (1997): Effects of joint attributes on tunnel stability. In: *International Journal of Rock Mechanics and Mining Sciences* 34 (3-4), S. 348. DOI: 10.1016/S1365-1609(97)00286-4.

Zhang, L., Einstein, H. H. & Dershowitz, W. S. (2002): Stereological relationship between trace length and size distribution of elliptical discontinuities. In: *Géotechnique* 52 (6), S. 419–433. DOI: 10.1680/geot.2002.52.6.419.

Zhang, L. & Einstein, H.H. (2000): Estimating the intensity of rock discontinuities. In: *International Journal of Rock Mechanics and Mining Sciences* 37 (5), S. 819–837. DOI: 10.1016/S1365-1609(00)00022-8.

Zhang, P., Zhao, Q., Tannant, D. D., Ji, T. & Zhu, H. (2019): 3D mapping of discontinuity traces using fusion of point cloud and image data. In: *Bull Eng Geol Environ* 78 (4), S. 2789–2801. DOI: 10.1007/s10064-018-1280-z.

Appendix

Appendix A Data Case Study I

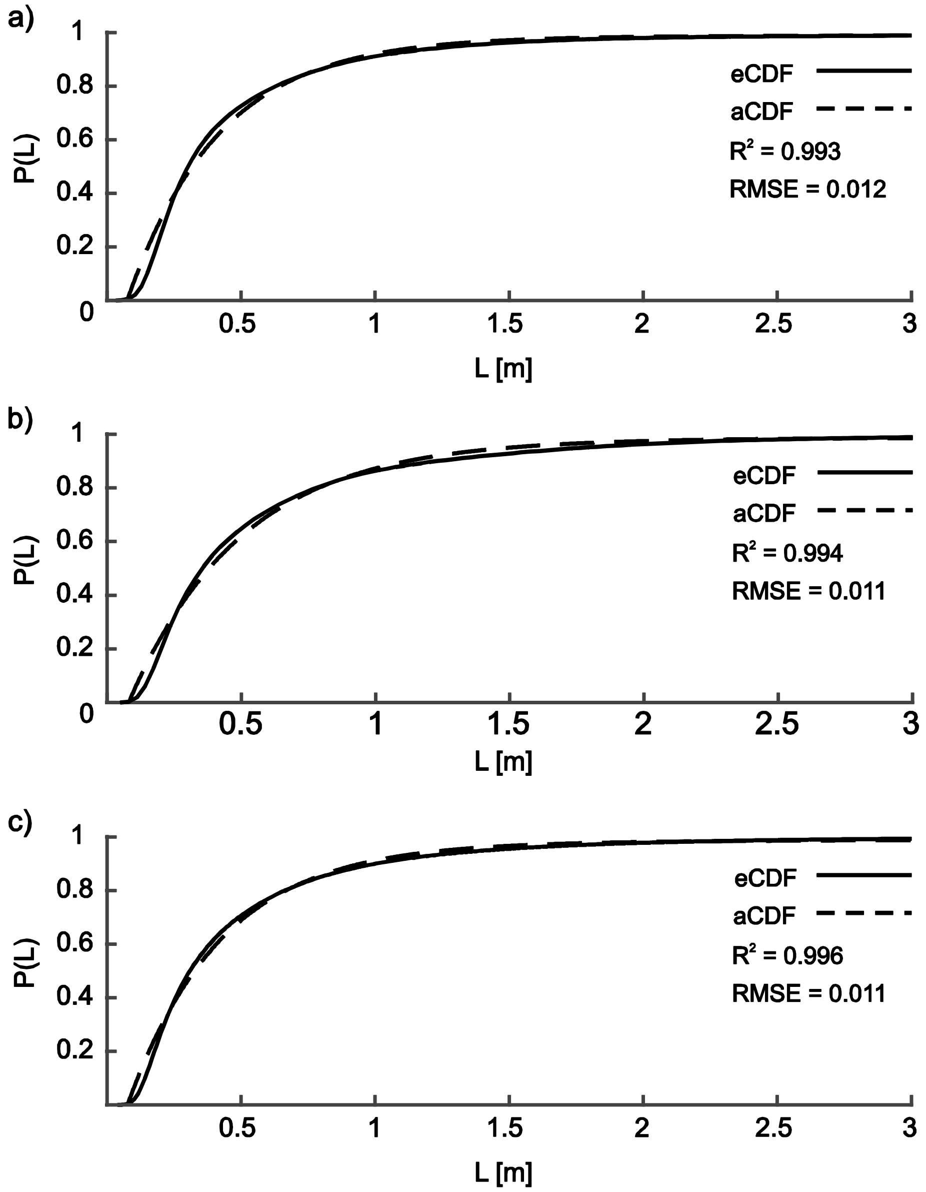

Figure 6.1: Empirical cumulative probability distributions (eCDF) of the two farthermost points in on structure as a reference for the joint size distribution (solid lines) per joint set (a to c) in Case Study I; the cumulative density distributions are approximated with the double-exponential function (aCDF) according to eq. 2.9 (dashed lines); each subplot includes the coefficient of determination (*R^2*) as well as the root mean squared error (RMSE).

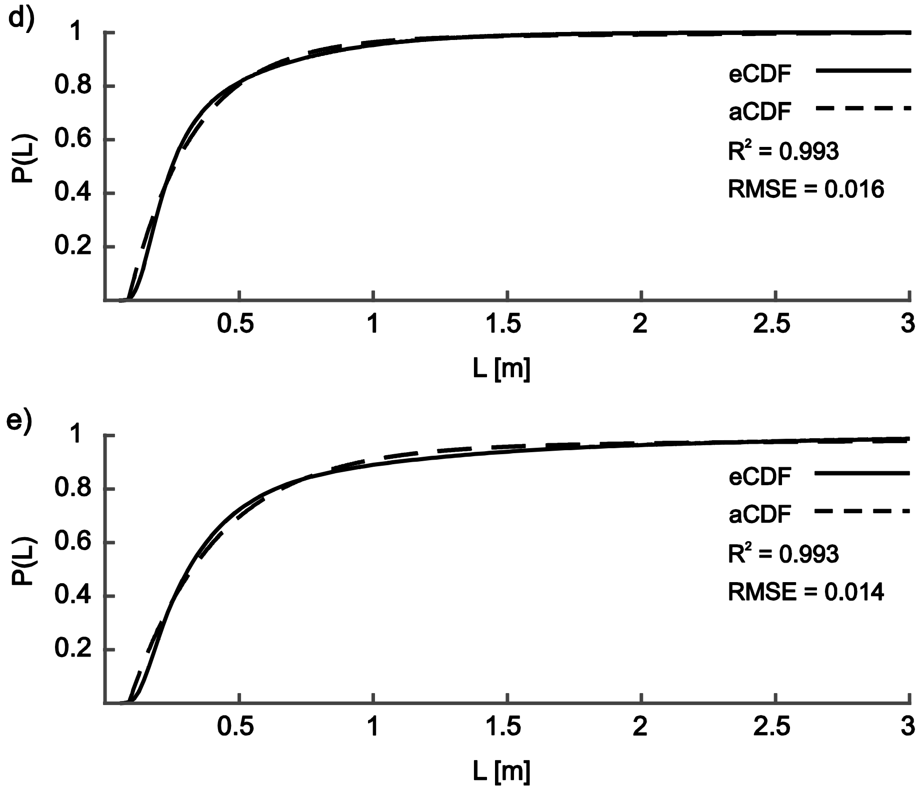

Figure 6.2: Continued – Empirical cumulative probability distributions (eCDF) of the two farthermost points in on structure as a reference for the joint size distribution (solid lines) per joint set (d and e) in Case Study I; the cumulative density distributions are approximated with the double-exponential function (aCDF) according to eq. 2.9 (dashed lines); each subplot includes the coefficient of determination (*R^2*) as well as the root mean squared error (RMSE).

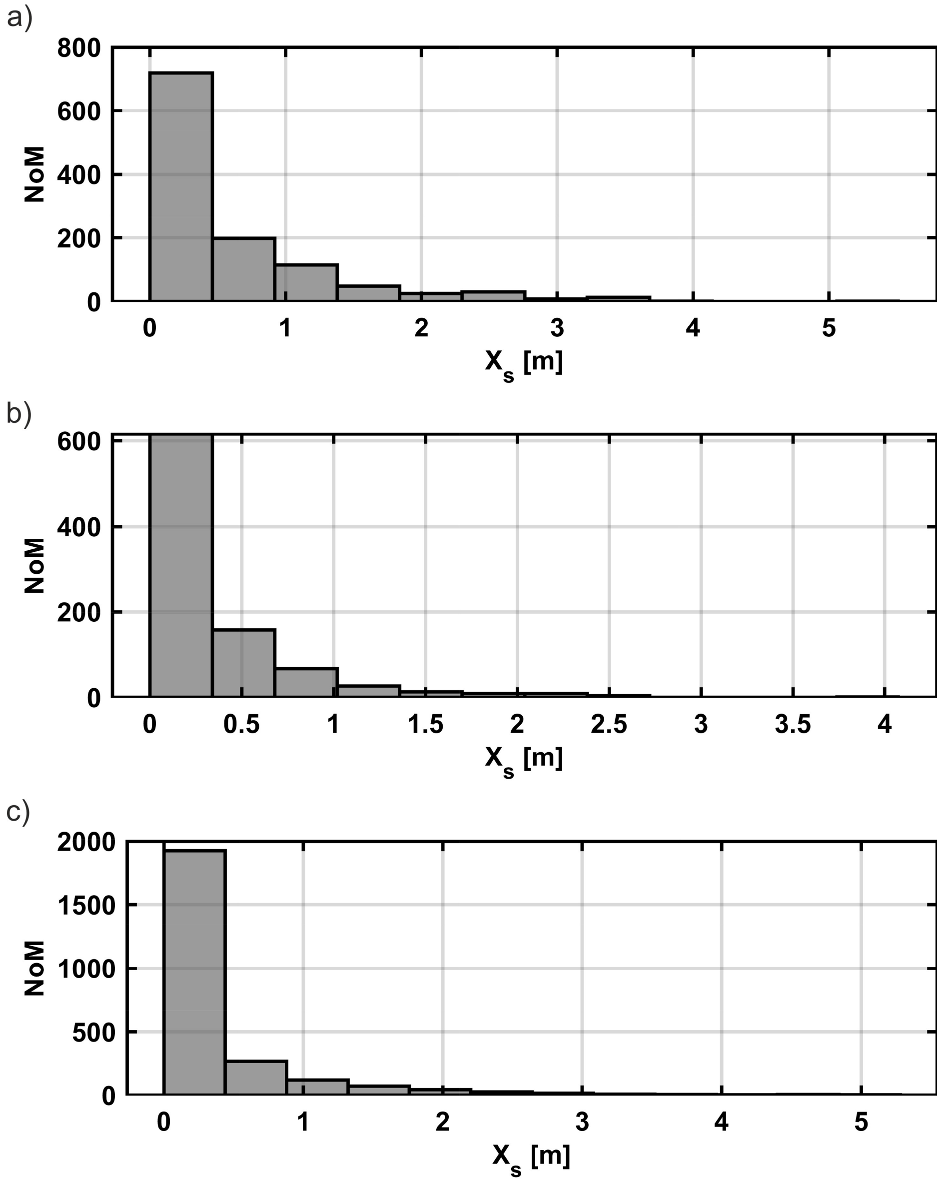

Figure 6.3: Histogram representation of the joint set spacings (X_s) per joint set JS1 to JS3 (a to c) in Case Study I; the measurements are calculated by the Multiple Scanline Tool in SMX Analyst.

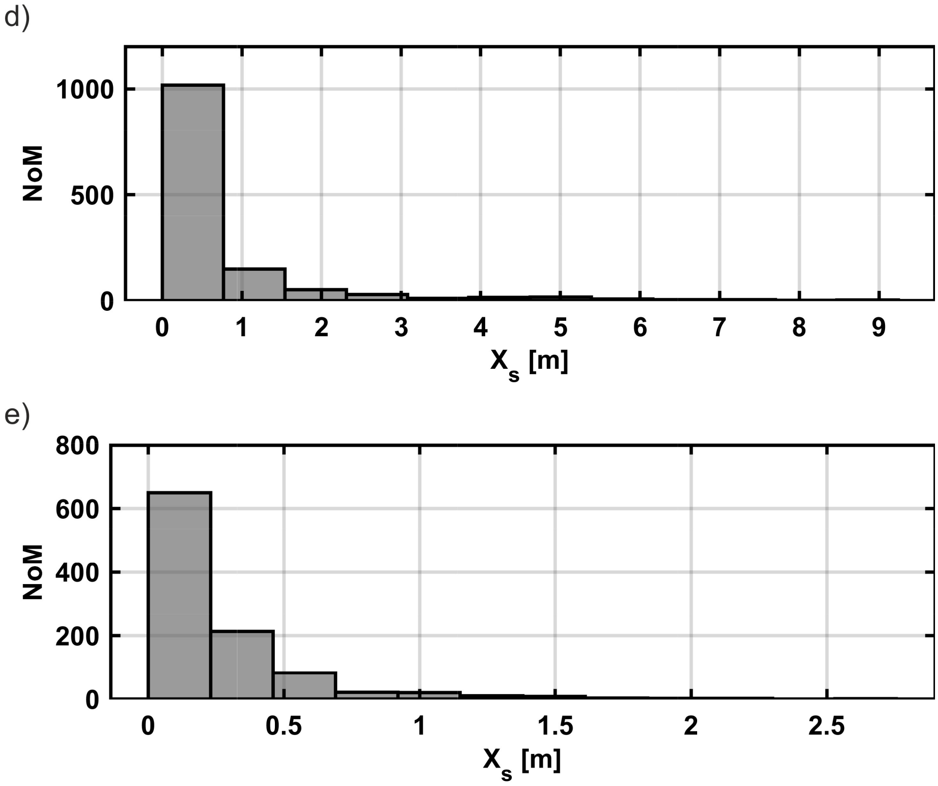

Figure 6.4: Continued – Histogram representation of the joint set spacings (X_s) for joint set JS4 and JS5 (d and e) in Case Study I; the measurements are calculated by the Multiple Scanline Tool in SMX Analyst.

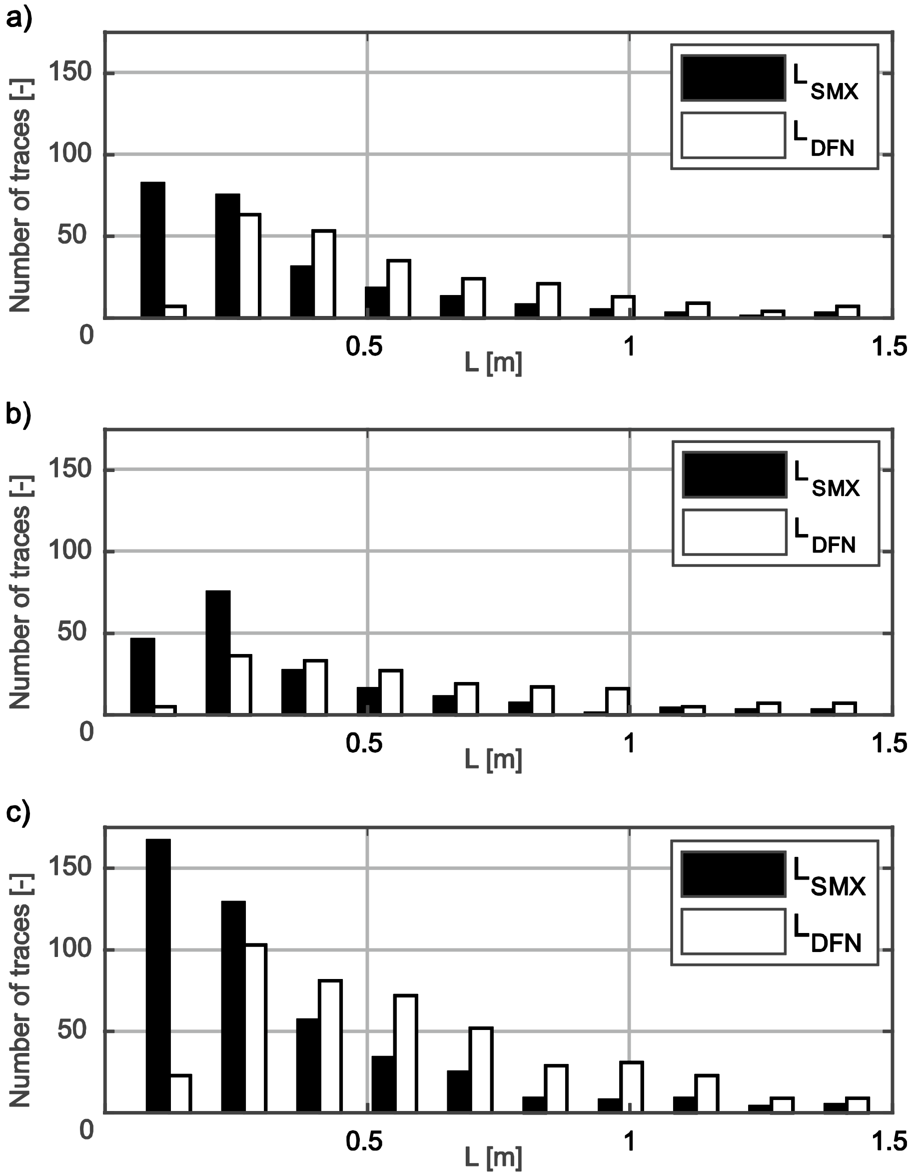

Figure 6.5: Histogram representation of the joint trace lengths (L_{SMX}/L_{DNF}) between 0 and 1.5 m per joint set (a to c) in Case Study I; the bars represent the joint trace lengths obtained from SMX Analyst, the lines represent the results obtained by the statistical recalculation of the joint size distribution for the DFN.

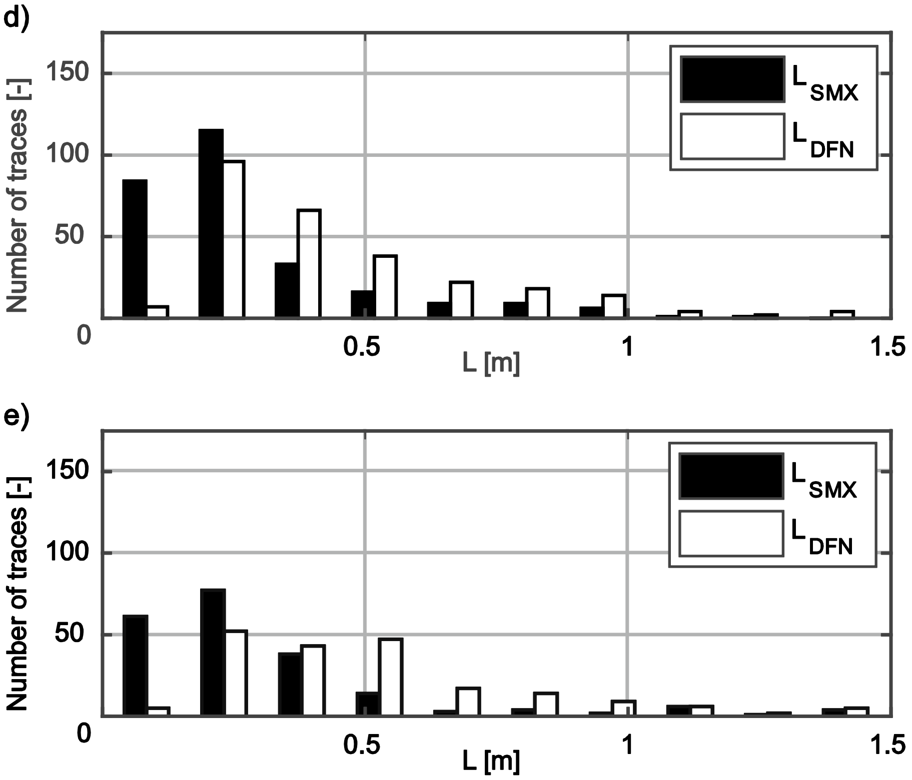

Figure 6.6: Continued – Histogram representation of the joint trace lengths (L_{SMX}/L_{DNF}) between 0 and 1.5 m per joint set (d and e) in Case Study I; the bars represent the joint trace lengths obtained from SMX Analyst, the lines represent the results obtained by the statistical recalculation of the joint size distribution for the DFN.

Appendix B Data Case Study II

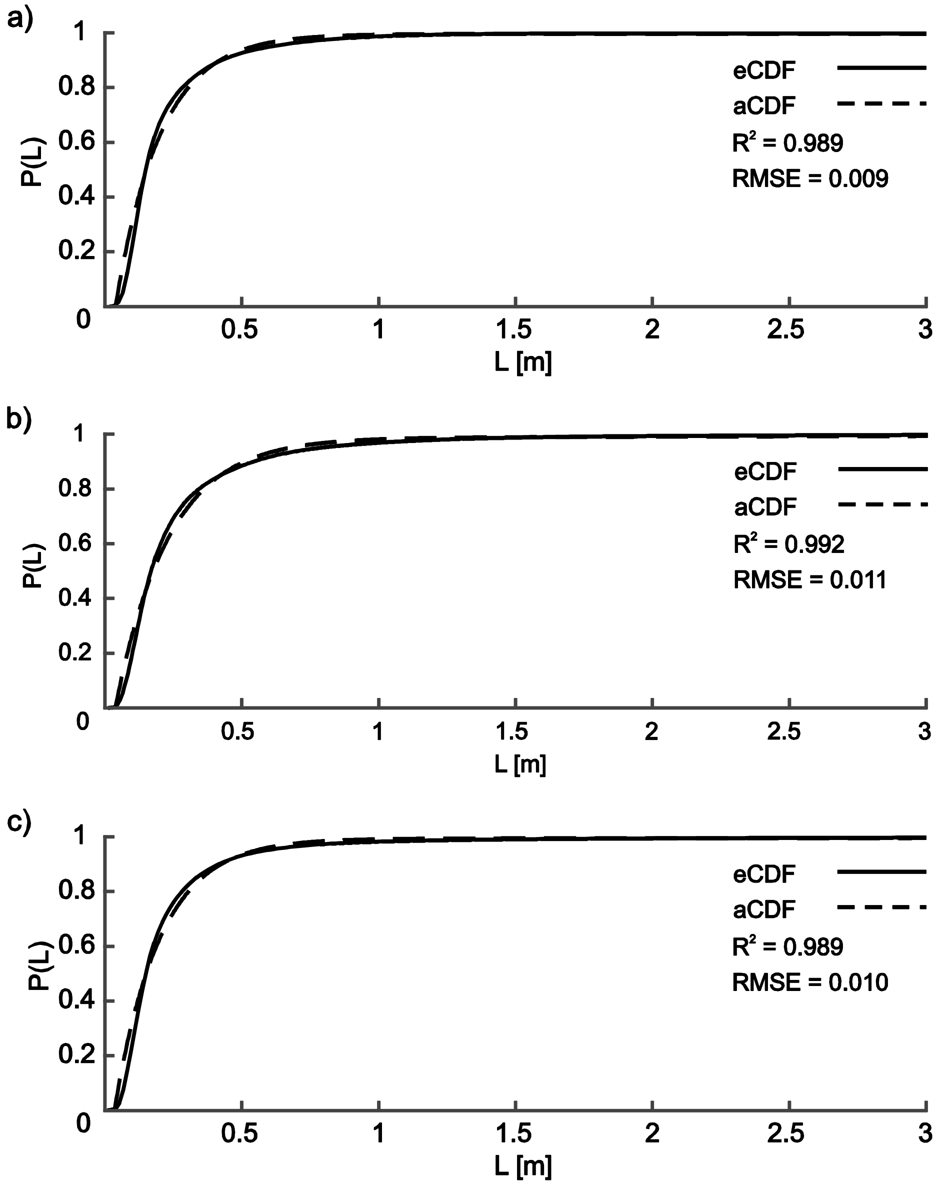

Figure 6.7: Empirical cumulative probability distributions (eCDF) of the two farthermost points in on structure as a reference for the joint size distribution (solid lines) per joint set (a to c) in Case Study II; the cumulative density distributions are approximated with the double-exponential function (aCDF) according to eq. 2.9 (dashed lines); each subplot includes the coefficient of determination (*R^2*) as well as the root mean squared error (RMSE).

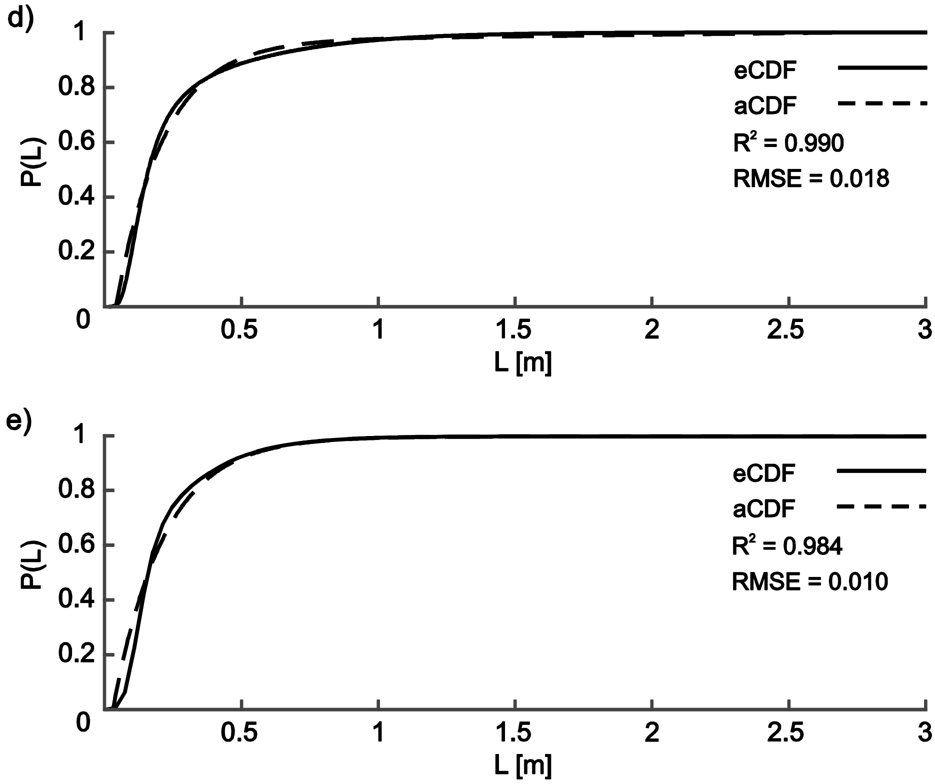

Figure 6.8: Continued – Empirical cumulative probability distributions (eCDF) of the two farthermost points in on structure as a reference for the joint size distribution (solid lines) per joint set (d and e) in Case Study II; the cumulative density distributions are approximated with the double-exponential function (aCDF) according to eq. 2.9 (dashed lines); each subplot includes the coefficient of determination (*R^2*) as well as the root mean squared error (RMSE).

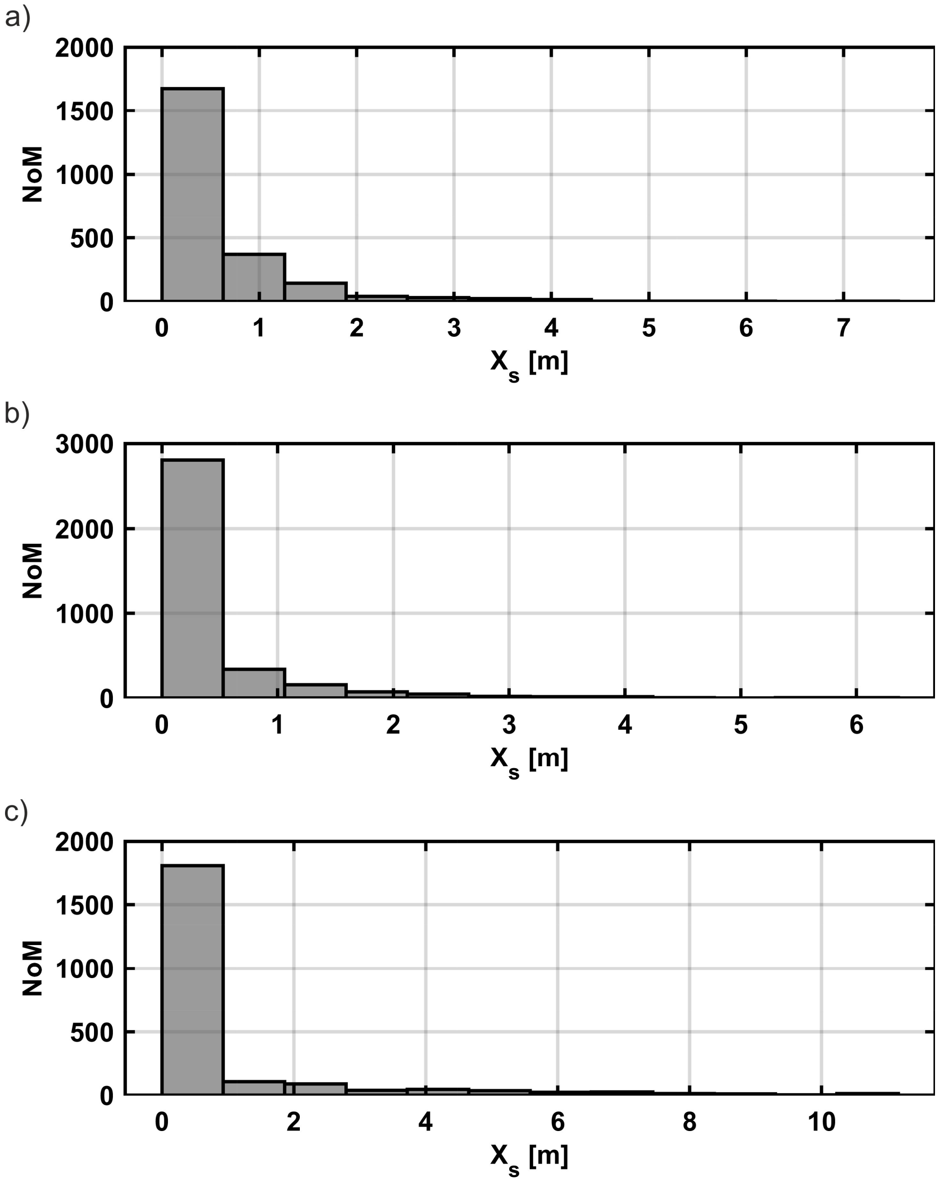

Figure 6.9: Histogram representation of the joint set spacings (X_s) per joint set JS1 to JS3 (a to c) in Case Study II; the measurements are calculated by the Multiple Scanline Tool in SMX Analyst.

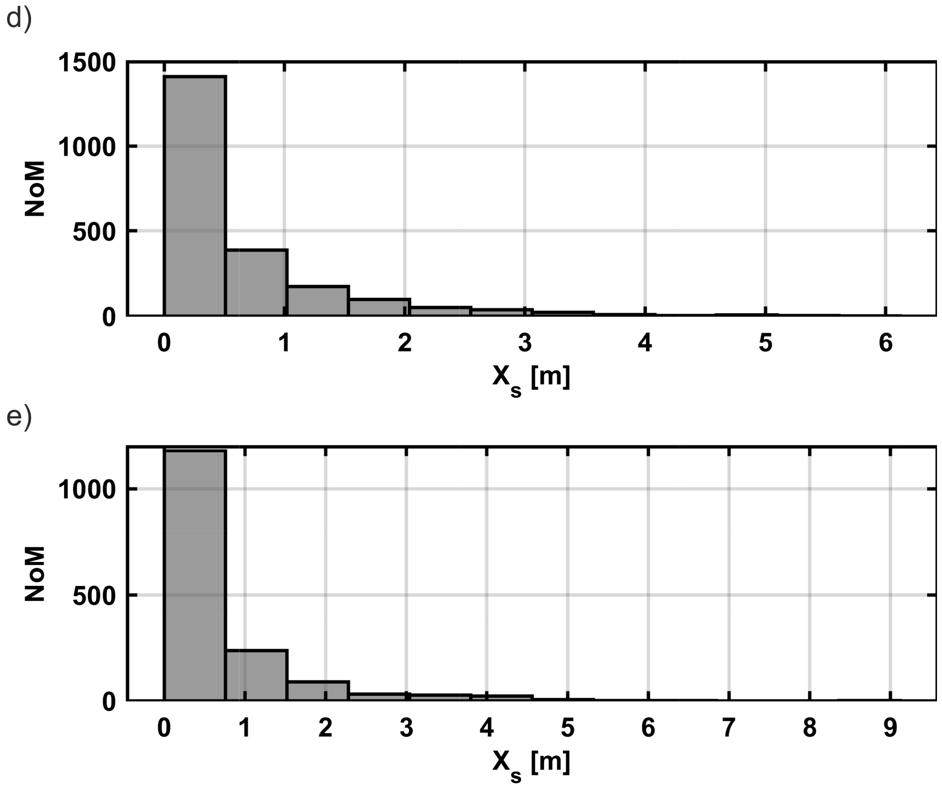

Figure 6.10: Continued – Histogram representation of the joint set spacings (X_s) for joint set JS4 and JS5 (d and e) in Case Study II; the measurements are calculated by the Multiple Scanline Tool in SMX Analyst.

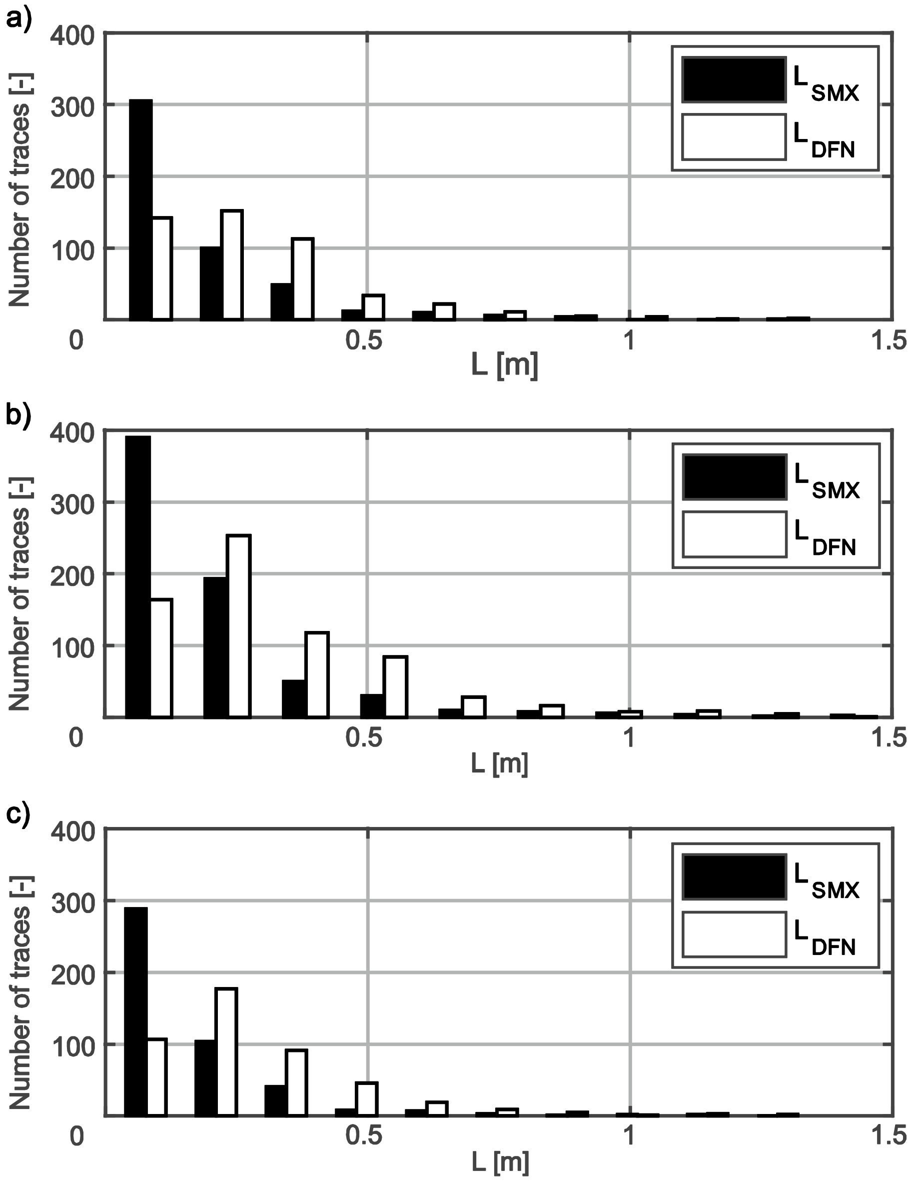

Figure 6.11: Histogram representation of the joint trace lengths (L_{SMX}/L_{DNF}) between 0 and 1.5 m per joint set (a to c) in Case Study II; the bars represent the joint trace lengths obtained from SMX Analyst, the lines represent the results obtained by the statistical recalculation of the joint size distribution for the DFN.

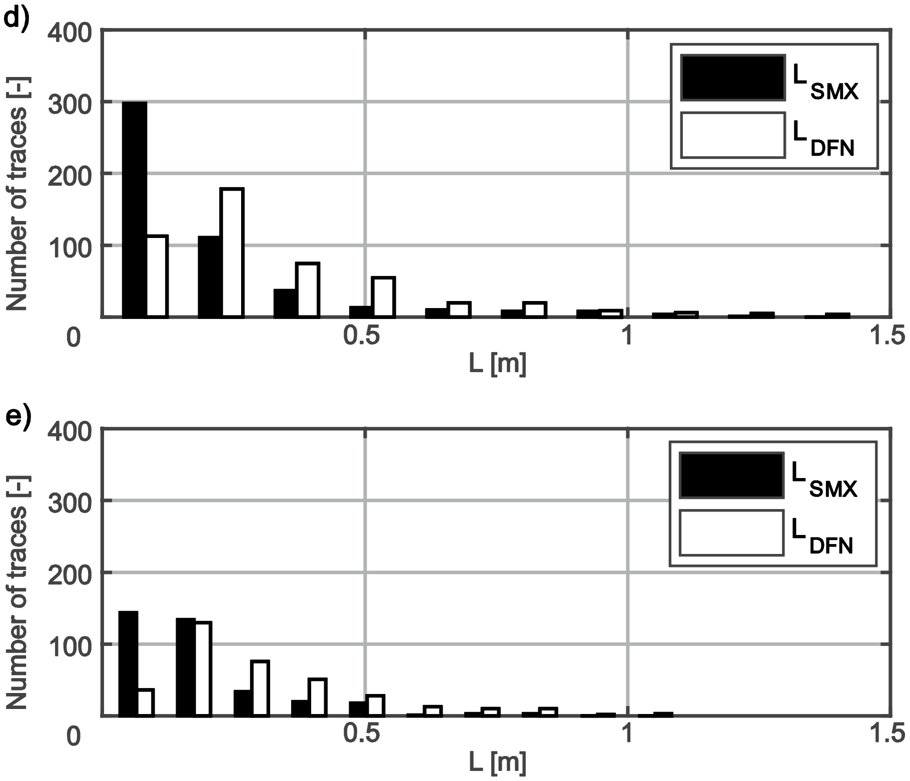

Figure 6.12: Continued – Histogram representation of the joint trace lengths (L_{SMX}/L_{DNF}) between 0 and 1.5 m per joint set (d and e) in Case Study II; the bars represent the joint trace lengths obtained from SMX Analyst, the lines represent the results obtained by the statistical recalculation of the joint size distribution for the DFN.

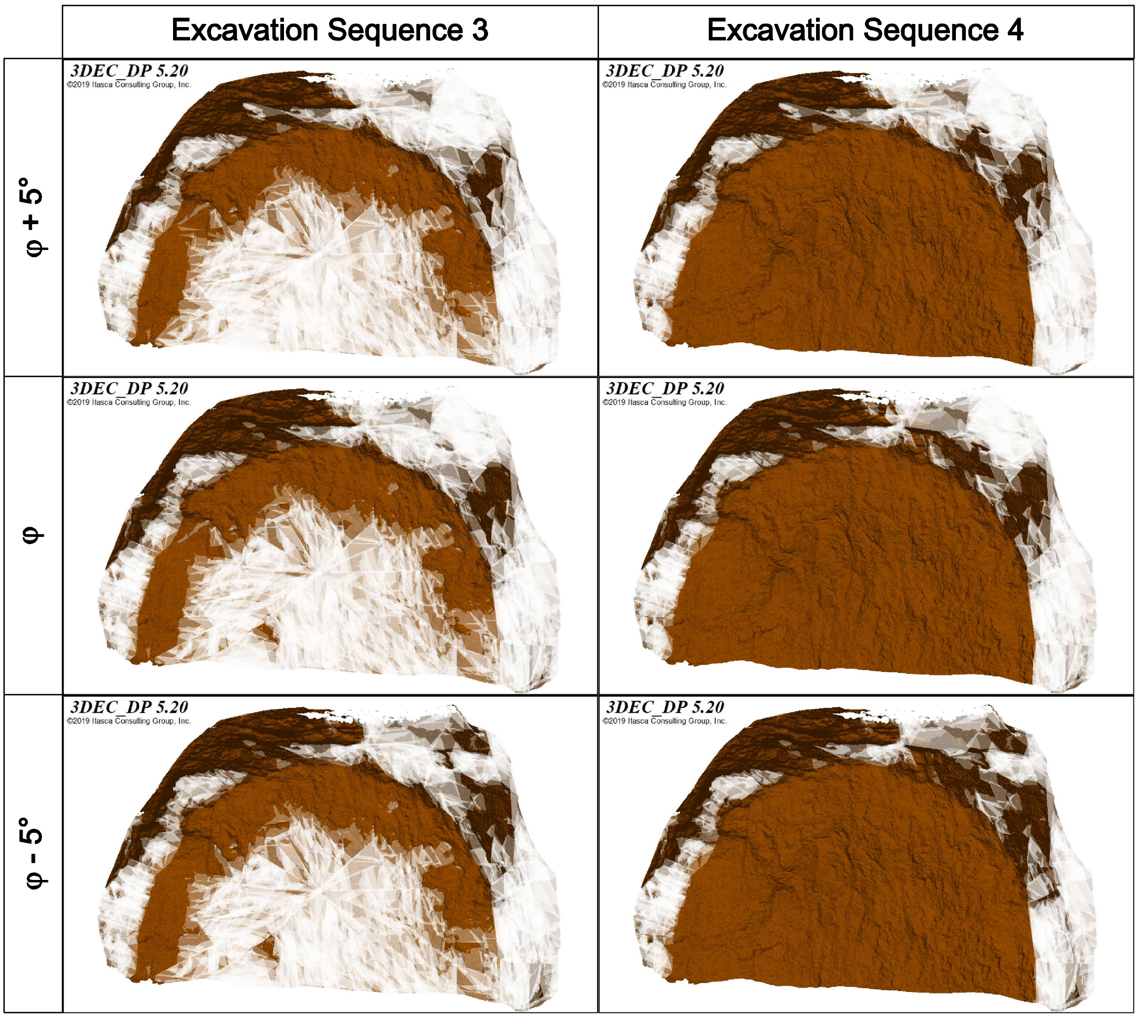

Figure 6.13: Numerical representation of the rock mass in Case Study II after deleting all blocks moving more than 1 cm in SSS-3 and SSS-4 at different friction angles and $K = 0.33$; the DSM is displayed in brown, the remaining blocks are shown in a transparent white colour.